January 2012

Measurement And Analysis Of Turbulence Response Near The Stagnation Region Of Large Diameter Cylindrical Leading Edges With Aftbody

Md. Nafiz H. K. Chowdhury

MEASUREMENT AND ANALYSIS OF TURBULENCE RESPONSE NEAR THE STAGNATION REGION OF LARGE DIAMETER CYLINDRICAL LEADING EDGES WITH AFTBODY

by

Md. Nafiz H. K. Chowdhury

Bachelor of Science, Bangladesh University of Engineering & Technology,

2008

A Thesis

Submitted to the Graduate Faculty

of the

University of North Dakota

In partial fulfillment of the requirements

for the degree of

Master of Science

Grand Forks, North Dakota

December

2012

This Thesis, submitted by Md. Nafiz H. K. Chowdhury in partial fulfillment of the requirements of the Degree of Master of Science from The University of North Dakota, has been read by the faculty advisory Committee under whom the work has been done and is hereby approved

_____

Forrest E. Ames, Ph.D.
Chairperson

_____

Nanak Grewal, Ph.D.

_____

Yeo Howe Lim, Ph.D.

This thesis is being submitted by the appointed advisory committee as having met all of the requirements of the Graduate School at the University of North Dakota and is hereby approved.

_____

Wayne Swisher, Ph. D.
Dean of the Graduate School

_____

Date

PERMISSION

Title Measurement and Analysis of Turbulence Response near the Stagnation Region of Large Diameter Cylindrical Leading Edges with Aftbody

Department Mechanical Engineering

Degree Master of Science

In presenting this thesis in partial fulfillment of the requirements for a graduate degree from the University of North Dakota, I agree that the library of this University shall make it freely available for inspection. I further agree that permission for extensive copying for scholarly purposes may be granted by the professor who supervised my thesis work or, in his absence, by the chairperson of the department or the dean of the Graduate School. It is understood that any copying or publication or other use of this thesis or part thereof for financial gain shall not be allowed without my written permission. It is also understood that due recognition shall be given to me and to the University of North Dakota in any scholarly use which may be made of any material in my thesis.

Md. Nafiz H. K. Chowdhury

October 10, 2012

TABLE OF CONTENTS

LIST OF FIGURES……...vii

LIST OF TABLES……....xix

NOMENCLATURE..……...xx

ACKNOWLEDGEMENT…….……..xxii

ABSTRACT……...xxiv

CHAPTERS

I. INTRODUCTION……..1

II. RELEVENT PAST STUDIES……....6

2.1 Experimental Investigation of the Influence of Turbulence on Stagnation Region Heat Transfer……...7

2.2 Numerical Investigation of Turbulence Effects on Stagnation Region Heat Transfer……...22

2.3 Present Viewpoint……26

III. EXPERIMENTAL SETUP……..27

3.1Wind Tunnel Facility……....27

3.2 Turbulence Generators ……31

*3.2.1*Aero-combustor ……..32

3.2.2. High Turbulence Generator……...32

3.2.3 Grid Generated Turbulence……35

3.3 Traversing Section……...36

3.4 Fabrication of Test Bodies……...38

3.5 Tip design……42

3.6 Data Acquisition System……..43

*3.6.1*Temperature Measurement……..43

3.6.2 Pressure Measurement……44

3.7 Hot Wire Measurements……..44

3.8 Fundamental Data Analysis……45

IV. COMPUTATIONAL PREDICTIONS FOR EXPERIMENTAL SETUP……..48

4.1Gambit Model……..49

4.2 Fluent Setup ……..51

V. EXPERIMENTAL RESULTS……..53

5.1 Test Conditions……...54

5.2 Single Wire Measurements……55

5.3 Description of the Flow Field……56

5.4 Turbulence measurements without the cylinders……...57

5.5 Mean Velocity Distributions……..61

5.6 Turbulence Characteristics……....71

5.6.1 RMS fluctuating velocity……..72

5.6.2 Turbulence Energy Scale (Lu)……..74

5.6.3 Integral Length Scale (L_x)……76

5.6.4 Spectrum Analysis..……..78

5.6.5 Dissipation Rate (ε)……...81

5.6.6 Effective Length (L_e) ……83

VI. CONCLUSIONS…..…….....95

APPENDICES……...99

REFERENCES……126

LIST OF FIGURES

Figure Page

1. Rolls Royce AE 3007 turbofan engine used to power the Global Hawk surveillance aircraft (Courtesy of Rolls Royce). 5
2. GE TM2500 Trailer Mounted Aeroderivative Gas Turbine (Courtesy of GE Energy). 5
3. Flat-plate Free-Streamline Model by Bearman (P.W.Bearman 1972). 9
4. Mean velocity approaching stagnation region. O-smooth flow; Δ-grid; 11
5. Distribution of TI and Length Scale in streamwise direction (y/d = 0 and z/d = 4.57) 16
6. Rig Layout.(Smith, M.C., and Kuethe, A.M. 1966) 18
7. Wind tunnel and turbulence grid used in Nix and Diller's (Nix, A.C., Diller, T.E. 2009) experiment. 20
8. Velocity profile and Turbulence length scale distribution as a function of distance from the cylinder in Nix and Diller's (Nix, A.C., Diller, T.E. 2009) experiment. 20
9. Streamwise rms velocity and turbulence distribution as a function of distance from the cylinder in Nix and Diller's (Nix, A.C., Diller, T.E. 2009) experiment. 21

10. Turbulence intensity along the stagnation streamline (Zhongmin Xiong and Sanjiva K. Lele 2007). The solid line is a power law fit using the same the exponent (-0.83) as in Van Folssen's (Van Fossen, G.J., Simoneau, R.J., and Ching, C.Y. 1995) experiment. 25
11. Turbulence intensity along the stagnation streamline, transformed x axis (Zhongmin Xiong and Sanjiva K. Lele 2007). 25
12. Schematic of Low Speed Wind Tunnel with Cylindrical Test Section. 28
13. Schematic of the heat exchanger cooling water system (Barbot 2003). 29
14. Heat exchanger cooling water pump and tank installation (Barbot 2003)....30
15. Schematic of aeroderivative combustor turbulence generator. 33
16. Front view of Aero Combustor and High Turbulence Generator....34
17. Rear view of Aero Combustor and High Turbulence Generator....34
18. The grid turbulence generator assembly (Indrajit Jaswal 2008). 36
19. Traversing section inside the testing tunnel. 37
20. Geometry profiles of the 0.1016 cm (4″) and 0.4064 (16″) cm diameters. 39
21. Calculated surface velocity distributions over 0.1016 cm (4″) and 0.4064 cm (16″) diameters....39
22. Top view of 4″ diameter leading edge cylinder body. 40
23. Front view of 4″ diameter leading edge cylinder body with tip. 40
24. Front view of 16″ diameter leading edge cylinder body with tip. 41

25. Top view of 16″ diameter leading edge cylinder body. 41
26. Tip for small (4″ diameter) cylinder. 42
27. Tip for big (16″ diameter) cylinder. 43
28. 2D Gambit Model. 49
29. 2D Gambit model with mesh. 50
30. Close view of mesh near the stagnation region. 50
31. Plot of residuals after 10,000 iterations. 52
32. Contour plot for velocity magnitude at inlet velocity of 10 m/s. 52
33. Streamwise local turbulence distributions in the upstream from the stagnation point at 10 m/s. 58
34. Energy scale plot along the stagnation streamline upstream of the stagnation point at 10 m/s. 59
35. Integral length scale plot along the stagnation streamline upstream of the stagnation point at 10 m/s. 60
36. Dissipation rate distribution along the stagnation streamline upstream of the stagnation point at 10 m/s. 61
37. Dimensionless mean velocity distribution along normalized upstream distance from the cylinder stagnation point at four different Reynolds numbers for aero combustor (AC1) for 4″ cylinder. 65

38. Dimensionless mean velocity distribution for 16″ cylinder along normalized upstream distance from the cylinder stagnation point at four different Reynolds numbers for aero combustor (AC1). 65
39. Dimensionless mean velocity distribution for 4″ cylinder along normalized upstream distance from the cylinder stagnation point at four different Reynolds numbers for aero combustor with spool (ACS). 66
40. Dimensionless mean velocity distribution for 16″ cylinder along normalized upstream distance from the cylinder stagnation point at four different Reynolds numbers for aero combustor with spool (ACS). 66
41. Dimensionless mean velocity distribution for 4″ cylinder along normalized upstream distance from the cylinder stagnation point at four different Reynolds numbers with big grid (GR1). 67
42. Dimensionless mean velocity distribution for 16″ cylinder along normalized upstream distance from the cylinder stagnation point at four different Reynolds numbers with big grid (GR1).....67
43. Dimensionless mean velocity distribution for 4″ cylinder along normalized upstream distance from the cylinder stagnation point at four different Reynolds numbers with small grid near (GS1). 68

44. Dimensionless mean velocity distribution for 16″ cylinder along normalized upstream distance from the cylinder stagnation point at four different Reynolds numbers with small grid at near position (GS1). 68
45. Dimensionless mean velocity distribution for 4″ cylinder along normalized upstream distance from the cylinder stagnation point at four different Reynolds numbers with small grid at far position (GS2)..... 69
46. Dimensionless mean velocity distribution for 16″ cylinder along normalized upstream distance from the cylinder stagnation point at four different Reynolds numbers with small grid at far position (GS2). 69
47. Dimensionless mean velocity distribution for 4″ cylinder along normalized upstream distance from the cylinder stagnation point at four different Reynolds numbers with high turbulence generator (HT1)..... 70
48. Dimensionless mean velocity distribution for 16″ cylinder along normalized upstream distance from the cylinder stagnation point at four different Reynolds numbers with high turbulence generator (HT1). 70
49. RMS fluctuating velocity distributions along upstream stagnation line for the small cylinder..... 73
50. RMS fluctuating velocity distributions along upstream stagnation line for the big cylinder. 74

51. Energy scale distributions along the upstream stagnation line for the small cylinder.....75

52. Energy scale distributions along the upstream stagnation line for the big cylinder.....75

53. Integral Length Scale distributions along stagnation streamline for small cylinder.....77

54. Integral Length Scale distributions along stagnation streamline for big cylinder.....77

55. Spectra for aero-combustor with spool for the small cylinder at 10 m/s. 80

56. Spectra for aero-combustor with spool for the big cylinder at 10 m/s. 80

57. Dissipation rate plots in the upstream of the small cylinder. 82

58. Dissipation rate plots in the upstream of the big cylinder.....83

59. Plot of Dissipation rate against Effective length with and without the small cylinder (4") in position for the aero combustor (AC1) at Re_D = 62,500. 84

60. Plot of Dissipation rate against Effective length with and without the small cylinder (4") in position for the aero combustor with spool (ACS) at Re_D = 62,500.....85

61. Plot of Dissipation rate against Effective length with and without the small cylinder (4") in position for the big grid (GR1) at Re_D = 62,500.....86

62. Plot of Dissipation rate against Effective length with and without the small cylinder (4") in position for the small grid at near location (GS1) at Re_D = 62,500.....87

63. Plot of Dissipation rate against Effective length with and without the small cylinder (4") in position for the small grid at far location (GS2) at Re_D = 62,500.....88

64. Plot of Dissipation rate against Effective length with and without the small cylinder (4") in position for the high turbulence generator (HT1) at Re_D = 62,500.....89

65. Plot of Dissipation rate against Effective length with and without the big cylinder (16") in position for the aero combustor (AC1) at Re_D = 250,000. 90

66. Plot of Dissipation rate against Effective length with and without the big cylinder (16") in position for the aero combustor with spool (ACS) at Re_D = 250,000.....91

67. Plot of Dissipation rate against Effective length with and without the big cylinder (16") in position for the big grid (GR1) at Re_D = 250,000. 91

68. Plot of Dissipation rate against Effective length with and without the big cylinder (16") in position for the small grid at near location (GS1) at Re_D = 250,000.....92

69. Plot of Dissipation rate against Effective length with and without the big cylinder (16") in position for the small grid at far location (GS2) at Re_D = 250,000.....93

70. Plot of Dissipation rate against Effective length with and without the big cylinder (16") in position for the high turbulence generator (HT1) at Re_D = 250,000.....94

71. Calibration curve with 4^{th} order polynomial fit.....108

72. Velocity distribution along the stagnation streamline 113

73. Dimensionless fluctuating velocity distribution for 4″ cylinder along normalized upstream distance from the cylinder stagnation point at four different Reynolds numbers with aero-combustor (AC1).....114

74. Dimensionless fluctuating velocity distribution for 4″ cylinder along normalized upstream distance from the cylinder stagnation point at four different Reynolds numbers for aero-combustor with spool (ACS).....114

75. Dimensionless fluctuating velocity distribution for 4″ cylinder along normalized upstream distance from the cylinder stagnation point at four different Reynolds numbers with big grid (GR1).....115

76. Dimensionless fluctuating velocity distribution for 4″ cylinder along normalized upstream distance from the cylinder stagnation point at four different Reynolds numbers with small grid at near location (GS1).....115

77. Dimensionless fluctuating velocity distribution for 4″ cylinder along normalized upstream distance from the cylinder stagnation point at four different Reynolds numbers with small grid at far location (GS2). 116
78. Dimensionless fluctuating velocity distribution for 4″ cylinder along normalized upstream distance from the cylinder stagnation point at four different Reynolds numbers for high turbulence generator (HT1). 116
79. Dimensionless fluctuating velocity distribution for 16″ cylinder along normalized upstream distance from the cylinder stagnation point at four different Reynolds numbers with aero combustor (AC1). 117
80. Dimensionless fluctuating velocity distribution for 16″ cylinder along normalized upstream distance from the cylinder stagnation point at four different Reynolds numbers for aero combustor with spool (ACS). 117
81. Dimensionless fluctuating velocity distribution for 16″ cylinder along normalized upstream distance from the cylinder stagnation point at four different Reynolds numbers for big grid (GR1). 118
82. : Dimensionless fluctuating velocity distribution for 16″ cylinder along normalized upstream distance from the cylinder stagnation point at four different Reynolds numbers for small grid at near location (GS1). 118

83. Dimensionless fluctuating velocity distribution for 16″ cylinder along normalized upstream distance from the cylinder stagnation point at four different Reynolds numbers for small grid at far location (GS2).....119
84. Dimensionless fluctuating velocity distribution for 16″ cylinder along normalized upstream distance from the cylinder stagnation point at four different Reynolds numbers for high turbulence generator (HT1).....119
85. Integral length scale distribution for 4″ cylinder along normalized upstream distance from the cylinder stagnation point at four different velocities for aero combustor (AC1).....120
86. Integral length scale distribution for 4″ cylinder along normalized upstream distance from the cylinder stagnation point at four different velocities for aero combustor with spool (ACS). 120
87. Integral length scale distribution for 4″ cylinder along normalized upstream distance from the cylinder stagnation point at four different Reynolds numbers for big grid (GR1).....121
88. Integral length scale distribution for 4″ cylinder along normalized upstream distance from the cylinder stagnation point at four different Reynolds numbers for small grid near position (GS1).....121

89. Integral length scale distribution for 4″ cylinder along normalized upstream distance from the cylinder stagnation point at four different Reynolds numbers for small grid at far position (GS2). 122
90. Integral length scale distribution for 4″ cylinder along normalized upstream distance from the cylinder stagnation point at four different velocities for high turbulence generator (HT1). 122
91. Integral length scale distribution for 16″ cylinder along normalized upstream distance from the cylinder stagnation point at four different velocities for aero combustor (AC1). 123
92. Integral length scale distribution for 16″ cylinder along normalized upstream distance from the cylinder stagnation point at four different velocities for aero combustor with spool (ACS). 123
93. Integral length scale distribution for 16″ cylinder along normalized upstream distance from the cylinder stagnation point at four different Reynolds numbers for big grid (GR1). 124
94. Integral length scale distribution for 16″ cylinder along normalized upstream distance from the cylinder stagnation point at four different Reynolds numbers for small grid at near position (GS1)..... 124

95. Integral length scale distribution for 16″ cylinder along normalized upstream distance from the cylinder stagnation point at four different Reynolds numbers for small grid at far position (GS2).....125

96. Integral length scale distribution for 16″ cylinder along normalized upstream distance from the cylinder stagnation point at four different Reynolds numbers for high turbulence generator (HT1).....125

LIST OF TABLES

Table Page

1. Table of various grid sizes and locations in Bearman's (P.W.Bearman 1972) investigation. 10

2. Table showing all the turbulence generators used with their corresponding turbulence intensities, length scale, and others at the stagnation point at no cylinder conditions..... 100

3. Table showing all stations that used for capturing data at different turbulence generator conditions 101

NOMENCLATURE

English Letter Symbols

$E_1(f)$ One dimensional energy spectrum of the velocity fluctuation u' as a function of frequency, f

$E_1(k_1)$ One dimensional energy spectrum of u' as a function of wave number

$E_1(k_1) = U\, E_1(f)/2\pi$, m^3/s^2

f Frequency, 1/s

K Turbulent kinetic energy, $(u'^2+v'^2+w'^2)/2$ m^2/s^2

k_1 Wave number, $k_1 = 2\,\pi\, f/U$, m^{-1}

Lu Energy scale, $Lu = 1.5\, |u'|^3/\varepsilon$, m

L_x Longitudinal integral length scale based on u' fluctuation, m

P_{atm} Atmospheric pressure, Pa

P_s Static pressure, Pa

P_T Total pressure, Pa

Re_D Diameter Reynolds number, based on V_{max}

T_∞ Free stream temperature, K

TLR Turbulence parameter, TLR = Tu $(\delta_2/Lu)^{1/3}$ $(Re_{\delta 2}/1000)^{1/4}$ for skin friction,

TLR= Tu $(\Delta_2/Lu)^{1/3}$ $(Re_{\Delta 2}/1000)^{1/4}$ for heat transfer

Tu Turbulence level, Tu = $\frac{\sqrt{u'^2}}{U_\infty}$

TRL Turbulence parameter, TRL = Tu $Re_D^{5/12}$ $(D/Lu)^{1/3}$

U Streamwise velocity, m/s

U_∞ Approach velocity (m/s)

u′ rms streamwise fluctuation velocity, m/s

ε Turbulent dissipation rate, m^2/s^3

A constant relating to the one-dimensional spectrum, 1.62

Notations

AC1 Aero Combustor

ACS Aero Combustor with spool

GR1 Big Grid

GS1 Small Grid at near position

GS2 Small Grid at far position

HT1 High Turbulence Generator

Subscripts

o At stagnation point of leading edge without the presence of cylinder

ACKNOWLEDGEMENT

I would like to thank the University of North Dakota, specifically the Mechanical Engineering department, for providing me the opportunity to receive a quality education. It is also my pleasure to acknowledge the people that have given me support and advice during my stay at the University of North Dakota. First of all, I would like to give thanks to my supervisor, Dr. Forrest E. Ames for all his support, encouragement and critique that he has given me over the last two and half years. Dr. Ames not only taught me a wealth of information but also provided every opportunity to achieve the goals that I had set out for myself. His invaluable guidance and perseverance has encouraged me to learn from my mistakes and move forward in my research.

Second, I would like to thank all of my fellow Graduate students that I have worked with at UND including Matthew Mihelish, Mitch Busche, Leo Moualeu and Jonathan Long. These people were members of Turbulent Transport in Turbines Group (TTTG). Having the privilege to work with such a good group of people made the last two years of my life a truly enjoyable experience. Also I would like to thank Dr. Gautham Krishnamoorthy for his support in understanding and helping me out with his knowledge in CFD and Dr. Nanak Grewal for extending his helpful hand towards me from the beginning of my degree.

I would also like to thank my parents, Firoz Khan and Nazma Firoz, for their never-ending unconditional love and continuous mental support they have given to me over the last two years. Their love has helped me to endure tough times and remain focused on my thesis work. This degree would not be possible without them, and I will never be able to thank them enough. The support and dedication they show to all their children is truly amazing. I would also like to thank the rest of my family including my brothers, Zulkernine and Nadim for their constant support. Thank you for being a wonderful family.

Finally, I would like to thank Gary Dubuque and Jay Evenstad for their help and advice in machining and Teri Berg for her administrative guidance.

ABSTRACT

The stagnation region of a turbine vane is a critical area for assessing heat transfer. The heat loads at that region are influenced by many factors such as the turbulence intensity, length scales, interaction of the turbulent eddies, vortex stretching and rapid straining of the fluid streamlines. In such a situation, it becomes difficult for gas turbine designers to accurately predict the heat transfer rate at leading edge stagnation region.

The purpose of this study is to investigate the response of high intensity free stream turbulence (FST) near the stagnation region of two different diameter leading edge cylinders in order to better understand the physics and to expand the parameter range for vane designers. Since FST has significant impact on the heat transfer augmentation, this study will examine the influence of elevated turbulence in the highly accelerating flow near the stagnation region. In the presence of the stagnation region of a body, turbulence can be intensified due to the straining field that elongates turbulent eddies or be blocked due to the presence of the wall. This amplification of turbulence allows eddies to penetrate closer to stagnation region surfaces and enhance the heat transfer augmentation.

In this research, a comprehensive set of data including velocities, turbulent components, and turbulent spectral information were acquired for two different diameter (0.1016 m and 0.4064 m) cylinders. Data for local heat transfer was previously recorded

by a previous graduate student. Hot wire measurements were acquired at various locations along the upstream stagnation stream line for a range of cylinder diameter Reynolds numbers and turbulence intensities. Turbulence measurements and energy spectra were acquired using hot-wire technique. Mean velocity profiles along the stream line were compared with computational fluid dynamic (CFD).

All these experiments were performed in UND's large scale, low speed cascade wind tunnel facility. Results from the larger cylinder and smaller cylinders of 0.4064 m and 0.1016 m diameters accordingly indicated in the previous studies that increasing turbulence intensity augments heat transfer at the stagnation region and promotes transition to turbulent flow. However, it was also evident from the previous experiments that, on the small cylinder, augmentation levels were closer to the TRL model prediction than that on the larger cylinder. The smaller cylinder with aft body tends to exhibit more rapid straining of the turbulent eddies from the oncoming turbulence, which intensified turbulence near the stagnation region.

CHAPTER I

INTRODUCTION

A gas turbine is a heat engine that utilizes a high-temperature and high pressure gas as the working fluid by transforming the thermal energy into mechanical energy. The required energy is produced from combustion of a fuel with air resulting in the needed temperatures in the turbine. In general, a gas turbine engine consists of a compressor, combustion chamber, and turbine. Then the working fluid, from the combustor, is directed circumferentially by guide vanes at the exit of the combustor nozzle to impinge upon turbine airfoils to utilize the energy. The turbine blades pass the gas stream, through their streamlined shapes after utilizing the tangential momentum of the gas that produces the power. A series of turbine blade rows are attached to a rotor/shaft assembly in multi stages and coupled with a compressor. The shaft rotation drives an electric generator for land based gas turbines to produce power and the compressor to bring air to the gas turbine combustor. But in an aircraft engine the shaft rotates the multi stage compressors and the fan to draw air into the combustion chamber and create thrust. Gas turbines produce a high quality heat that can be used to generate steam for combined-cycle applications to significantly enhance thermal efficiency. For utility applications, the combined cycle is the typical choice because the steam produced by the gas turbine exhaust is used to power a steam turbine for additional electricity generation. The challenge of achieving higher thermal efficiency for improved performance and less NO_x

emissions is reflected in the fact that they are conflicting goals, which magnifies the complexity. The higher temperatures typically produce higher NO_x emissions. Moreover, limiting oxygen in order to lower NO_x emissions can lead to unacceptably high levels of CO and unburned carbon emissions. In addition, increasing temperatures above the 1600^{o} C used in today's systems becomes a significant challenge to materials science and cooling designers.

Gas turbine engines operate on a thermodynamic cycle called the Brayton cycle. In this cycle there are two fundamental ways to increase the efficiency of the engine: increasing the compression ratio and increasing combustion temperature. Modern combined cycles use gas turbines with pressure ratios designed to maximize the overall cycle efficiency rather than just the efficiency of the gas turbine, effectively setting the pressure ratio for a given setup. This constraint on pressure ratio leaves engine designers one option to increase efficiency: increase the combustion temperature. Over the past 70 years, the gas turbine engine has gone through many modifications and improvements to attain the higher output and efficiency of the cycles. As a consequence, today's gas turbine engines are widely used in the areas of power generation and aircraft propulsion.

Today, the gas turbine industry is a very highly competitive field which is being driven by consumer demands for increased aero engines, higher thermal efficiency, reliability, and emissions. But the power output and efficiency of a gas turbine are directly a function of the turbine inlet temperature. In this regard, the gas turbine industry is continuously trying to increase the turbine inlet temperature. But this increase in the temperature causes both positive and negative consequences. Firstly, it increases the

efficiency of the cycle and secondly, it increases the erosion and deposition of particulates on the leading edge and upstream facing portions of the turbine vanes, creating a roughened surface. The presence of surface roughness on gas turbine vanes is known to decrease the efficiency of the engine by increasing the aerodynamic losses and increasing the heat transfer to the surface of the vane.

The increase in heat transfer to the surface of the vane is a particularly critical variable in the reliability of an engine. Gas turbines that are designed to attain maximum efficiency may be operating at inlet gas temperatures that are significantly higher than the maximum operating temperature of the vane material. Some modern high efficiency plants operate at firing temperatures in excess of 1600º C. The reason the vanes are able to withstand the extreme temperatures is due to the presence of intricate internal cooling schemes, thermal barrier coatings, and film cooling, and predicted heat loads from the hot gasses to the vane surface. If the surface of the vane is slowly changed due to the accumulation of surface roughness, the heat transfer characteristics are then changed which may result in component failure due to overheating of the material.

The stagnation region of a turbine vane is usually the area of high heat transfer and the level of heat load prediction can be complicated when hot gases combine with high intensity turbulence generated by the combustion system. Practically, turbulence intensities of up to 20 percent or more can be generated from the combustor. The interaction of turbulent eddies near the stagnation region is a complex phenomenon. The strain field can cause an intensification of relatively small eddies in the flow while the large eddies are blocked by the stagnation region surface. A combination of these various

factors such as high intensity freestream turbulence, very high Reynolds numbers, turbulent intensification due to rapid straining of the turbulent eddies contribute to the high levels of heat transfer augmentation generated at the leading edge stagnation region.

Now it is becoming progressively more important to predict the heat load distribution in the components downstream of the combustor. Inaccurate predictions can result in poor reliability, reduced life cycle and extra cost for redesign or maintenance. With the use of advanced component cooling schemes, it is possible to attain gas temperatures significantly above the maximum temperature of the alloy.

The intensification of turbulence in the vicinity of a stagnation region has previously been documented. However, turbulence seems to be unaffected along the pressure surface of a vane where the strain rate is smaller. Recent heat transfer measurements have suggested that turbulence may not be significantly intensified in the presence of large stagnation regions, which are becoming a more popular design for first vanes. Current work is focused on investigation of the turbulence decay and documenting the response of turbulence to large leading edge regions. These data should allow designers to improve predictive models and design more efficiently and reliable gas turbine components.

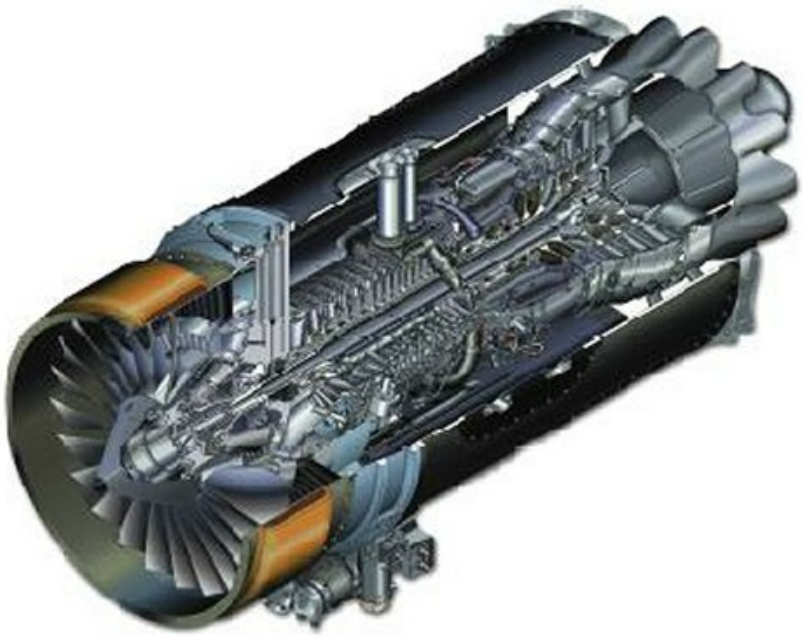

Figure 1: Rolls Royce AE 3007 turbofan engine used to power the Global Hawk surveillance aircraft (Courtesy of Rolls Royce).

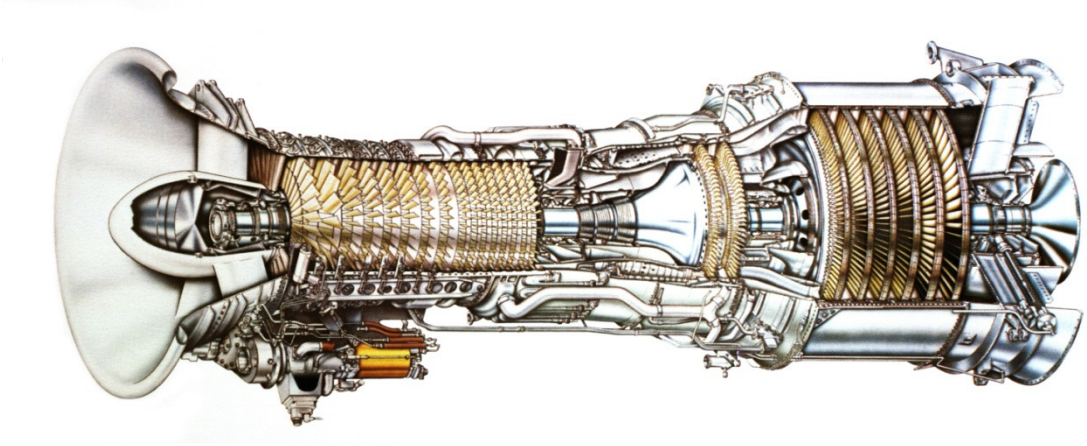

Figure 2: GE TM2500 Trailer Mounted Aeroderivative Gas Turbine (Courtesy of GE Energy).

CHAPTER II

RELEVENT PAST STUDIES

The purpose of the research is to investigate the response of high intensity free stream turbulence characteristics in the presence of the stagnation region of two different diameter leading edge cylinders while expanding the parameter range of turbulence effects on heat transfer for the designers. Since FST has a significant impact on the heat transfer augmentation; this study will examine the influence of elevated turbulence in the highly accelerating flow near the stagnation region. In the presence of the stagnation region of a body, turbulence can be intensified due to the strain field that elongates turbulent eddies. This amplification of turbulence allows eddies to penetrate closer to the stagnation region surfaces and enhance the heat transfer augmentation. Since the gas turbines have been in operation for decades, numerous studies similar to this have been conducted in the past. These studies focused on turbulence characteristics with the elevated turbulence intensity and Reynolds numbers. The history of turbulent spectra in the upstream of a body will aid in the enhancement of turbulence modeling. A literature review of the major findings was conducted to assess the state of knowledge in the field and to add confidence to the experimental techniques. The review will look at the turbulence measurements, and computational predictions.

A significant number of studies have documented average heat transfer at the stagnation region, but few studies have investigated heat transfer phenomena with details of the upstream turbulence history. These investigations examined a wide variation of relevant leading edge diameter aft body geometries but did not develop a quantitative link between the fluid flow field and its impact on the heat transfer. This research experimentally investigated the fluid dynamics and its characteristics near the stagnation region to enhance our understanding of the physics in this region.

This study is intended to provide a database of local fluid dynamics including velocity, turbulent components, and turbulent spectra in the presence of leading edge cylinders with aft body to support the development of more physically based turbulence models for use in predictive modeling of external flows.

2.1 Experimental Investigation of Turbulence Influence on Stagnation Region Heat Transfer

Zapp (Zapp 1950) was an early investigator who studied the influence of turbulence on cylindrical stagnation region heat transfer. He produced turbulence levels of 3.0% and 11.5% using grids and found heat transfer increases up to 68%. The influence of turbulence intensity on heat transfer has previously been considered as an important parameter in any stagnation region heat transfer. Kestin (Kestin 1966) suggested that an implicit assumption that considered into many early heat transfer

studies was that the turbulent scale was sufficiently small in comparison with the dimensions of the body.

Smith and Kuethe (Smith, M.C., and Kuethe, A.M. 1966) studied laminar heat transfer on a flat plate and a circular cylinder subjected to round rod square mesh grid generated turbulence up to 6 %. They found heat transfer increased about 30% in the laminar region of the flat plate and almost 70% increase on a circular cylinder. They suggested that the eddy diffusivity across the laminar boundary layer near stagnation region was proportional to the free stream turbulence times the wall normal distance ($\varepsilon_M \propto$ Tu y). They also came up with an approximately linear relationship between $Nu_D/Re_D^{1/2}$ and a parameter $TuRe_D^{1/2}$ they developed to correlate their findings. Smith and Kuethe's correlating parameter, $TuRe_D^{1/2}$, has previously been used widely as the basis to fit data from a range of investigations.

Later Kestin and Wood (Kestin, J., and Wood, R.T. 1971) investigated the effect of Reynolds number (75, 100 and 125×10^3) on the cylinders placed in cross flow at three at varying levels of turbulence intensity. In the range where the boundary layer is laminar, the effect of turbulence intensity is always to increase the heat transfer rate, approximately by a constant factor Φ which is a function of the turbulence intensity as well as the Reynolds number. Across the turbulent boundary layer and wake the influence is not systematic, as both increases and decreases are observed. The data for the stagnation line are compared with other measurements. They also used $TuRe_D^{1/2}$ to develop correlations as suggested by a semi empirical theory due to Smith and Kuethe (Smith, M.C., and Kuethe, A.M. 1966). However, the global correlation equation (a

second-degree polynomial) differs from the originally proposed linear relationship, and the uncertainty was quoted on the order of ±8 percent.

The nature of the freestream turbulence in the proximity of a stagnation point has been experimentally studied by P. W. Bearman (P.W.Bearman 1972). He measured all three components of the velocity as the flow approached a 2-D bluff body. The most remarkable increase in unsteadiness was measured for the w′ component in the direction transverse to the flow. His results also showed the distortion of grid generated turbulence as it approaches the stagnation region and explained by vortex stretching of the turbulence.

The bluff body he had used was a flat plate which was designed according to Roshko's notched hodograph method, as shown in figure below. Turbulence measurements were made using constant temperature anemometer (CTA) system. A traverse gear was embedded in the model to move the probe holder along the stagnation streamline. The values of the turbulence scale were estimated from power spectral density measurement based on Tylor's hypothesis.

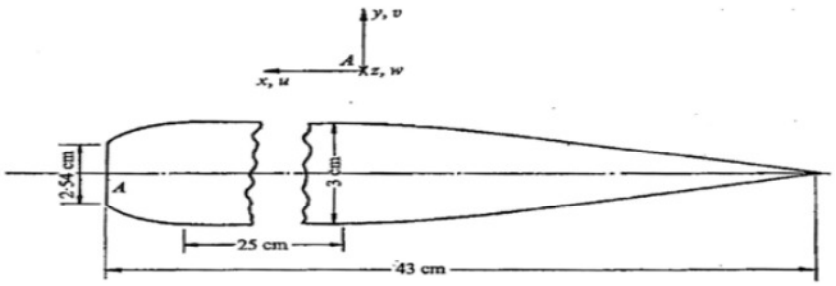

Figure 3: Flat-plate Free-Streamline Model by Bearman (P.W.Bearman 1972).

His primary interest was to study the distortion of grid-generated turbulence as it approaches near the bluff body. He used four different grids for his experiment shown in Table 1 and investigated the turbulence structure behind the grids. He performed these measurements in the absence of the model, at a distance from the grid, corresponding to the stagnation point.

Table 1: Table of various grid sizes and locations in Bearman's (P.W.Bearman 1972) investigation.

Grid	Mesh size M (cm)	Bar size b (cm)	Distance to stagnation point, x/M
A	3·81	0·98	70·4
B	7·62	1·28	35·1
C	15·22	3·11	17·6
D	22·83	3·77	11·7

He also made some hot-wire measurements for mean velocity distribution upstream of the bluff body and compared the data with Roshko's hodograph method and there was a good agreement between the experimental data and the predicted curve except near the stagnation region.

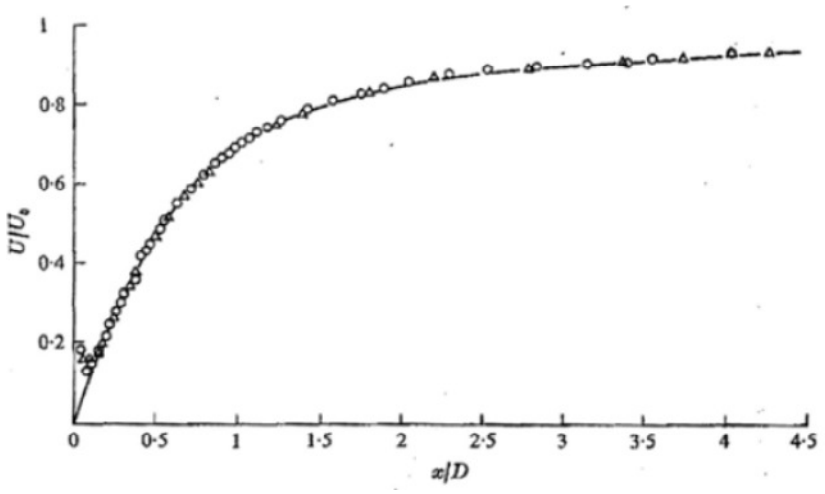

Figure 4: Mean velocity approaching stagnation region. O-smooth flow; Δ-grid; −−−hodograph solution (P.W.Bearman 1972).

According to Bearman, when $L_x/D >> 1$, a quasi-steady type of approach may be used, and along the stagnation streamline, $(\overline{u^2})^{1/2}$ attenuates similar to the mean flow pattern. However, when $L_x/D << 1$, turbulence is distorted by the mean flow field and ($\overline{u^2})^{1/2}$ amplifies due to vortex stretching. He also found the combination of these effects with attenuation of energy at low wave numbers and amplification at high wave numbers for L_x/D= O (1).

Britter, Hunt, and Mumford (R. E. Britter, J. C. R. Hunt AND J. C. Mumford 1979) experimentally studied the response of grid-generated turbulence past a circular cylinder using hot-wire anemometry over a Reynolds number range from 4.25×10^3 to 2.74×10^4 and a range of intensities from 0.025 to 0.062. Measurements of the mean velocity distribution, and rms intensities and spectral energy densities of the turbulent velocity fluctuations are presented for various radial and circumferential positions relative to the cylinder, and for ratios of the cylinder radius *a* to the scale of the incident

turbulence L_x, ranging from 0.05 to 1.42**.** The influence of upstream conditions on the flow in the cylinder wake and its associated induced velocity fluctuations is discussed. Their results usually supported Hunt's predictions. They determined the response of spectra approaching a cylinder and found the amplification of relatively high wave number spectra by the cylindrical strain field and the blocking of relatively low wavenumber spectra by the cylinder's surface.

VanFossen and Simoneau (VanFossen, G. J.& Simoneau, R. J. 1987) studied the relationship between FST and stagnation region heat transfer. They generated Reynolds number ranging from 13,000 to 177, 000 and measured spanwise averaged heat transfer rate for high and low turbulence cases. They also made some hot-wire measurements near the stagnation region and found that the mean velocity dropped monotonically as the flow approached to the stagnation region. They also suggested that the vorticity could be amplified due to the mean velocity gradients as flow moves closer to the stagnation region.

Ames and Moffat (Ames, F.E., and Moffat, R.J. 1990) investigated the influence of high intensity large scale turbulence on cylindrical stagnation region heat transfer. They compared their results with Kestin and Wood's (Kestin, J., and Wood, R.T. 1971) correlation based on cylinder diameter for a given turbulence generator and the data fell well below. They developed a simple spectral model based on the previous work from Hunt (Hunt 1973) and Britter, Hunt, and Mumford (R. E. Britter, J. C. R. Hunt AND J. C. Mumford 1979) which considered the intensification of high wavenumber spectra due to the straining and the blocking of low wavenumber spectra due to the proximity to the surface. They developed a simple eddy diffusivity model using the spectral model of

turbulence. They also developed the parameter TRL parameter [Tu $Re_D^{5/12}(Lu/D)^{1/3}$] for stagnation region heat transfer based on the eddy diffusivity model using scaling derived from the turbulent heat flux equation. Later, Ames et al. [(Ames, F.E., and Moffat, R.J. 1990), (Ames 1997), (Ames, F.E., Wang, C., and Barbot, P.A. 2003), (F. E. Ames, L. A. Dvorak, and M. J. Morrow 2005)] have correlated a range of stagnation region heat transfer data with that and suggested a good engineering estimation for the stagnation region heat transfer is $Nu/Nu_0 = 1 + 0.04*TRL$.

Mehendale et al. (Mehendale, A.B., Han, J.C., and Ou, S. 1991) studied grid generated mainstream turbulence effect on leading edge heat transfer. They generated turbulence by using a bar grid (Tu = 3.3–5.1%), passive grid (Tu = 7.6–9.7 %), and an innovative jet grid (Tu = 12.9–15.2 %). They considered leading edge diameter Reynolds numbers of 25,000, 40,000, and 100,000. They measured spanwise and streamwise distributions of local heat transfer coefficients on the leading edge and flat sidewall. They found that the leading edge heat transfer increases appreciably with increasing mainstream turbulence intensity, but the effect weakens at the end of the flat sidewall due to turbulence decay. Stagnation point heat transfer results for high turbulence intensity flows are in good agreement with the Lowery and Vachon's correlation (Lowery, G.W., Vachon, R.I. 1975), but the overall heat transfer results for the leading edge quarter-cylinder region are over estimated for their overall correlation for the entire circular cylinder region.

Van Fossen, G.J., Simoneau, R.J., and Ching, C.Y (Van Fossen, G.J., Simoneau, R.J., and Ching, C.Y. 1995) investigated the influence of free-stream turbulence intensity, length scale, Reynolds number, and leading-edge velocity gradient on stagnation-region

heat transfer in their experiment. Heat transfer was measured in the stagnation region for four models with elliptical leading edges downstream of five turbulence-generating grids. They concluded that stagnation-region heat transfer augmentation increased with decreasing length scale but they failed to define an optimum scale for the turbulence generating grid used in their study. An empirical correlation was developed that fit heat transfer data for isotropic turbulence to within ±4 percent but did not predict data for anisotropic turbulence. Stagnation heat transfer augmentation caused by turbulence was unaffected by the velocity gradient. The data of other researchers compared well with the correlation. A method of predicting heat transfer downstream of the stagnation point was also developed.

Ames (Ames 1997) and Ames et al. (Ames, F.E., Wang, C., and Barbot, P.A. 2003, Ames, F.E., Argenziano, M., Wang 2004) investigated heat transfer augmentation on the stagnation regions and laminar pressure sides of turbine vanes. Their results showed that while heat transfer augmentation in the stagnation region correlates the TRL parameter [$TuRe_D^{5/12}$ $(Lu/D)^{1/3}$], augmentation on the pressure side correlated more closely to [$TuRe_C^{1/3}$ $(Lu/C)^{1/3}$], where C is the cord length. They suggested that turbulence in the stagnation region was intensified due to the strain field. However, even though the relative level of heat transfer augmentation was high, the straining of turbulence along the pressure side had no noticeable effect on heat transfer augmentation.

Van Fossen and Chan Y. Ching (G. James Van Fossen and Chan Y. Ching 1997) also studied the influence of integral length scales on stagnation region heat transfer of a circular leading edge along with wide range of different grid generated turbulence. Their

objective was to determine a length scale that could be responsible for the greatest augmentation in stagnation region heat transfer for a given turbulence intensity. They also aimed to develop a prediction tool for stagnation heat transfer in the presence of FST. Five turbulence generating grids were used producing turbulence intensities in the range of 1.1 to 15.9 % while the ratio of integral length scale to cylinder diameter (L_x/D) ranged from 0.05 to 0.30. They estimated turbulence intensity and integral length as a function of distance from the grids. Data were captured at cylinder Reynolds numbers ranging from 42,000 to 193,000. Results showed that stagnation region heat transfer rate increases by turbulent augmentation as length scale decreases. Though an optimum scale was not found, but they developed a correlation that fit heat transfer data for the square bar grids to within +4%. They also suggested that the degree of isotropy in the turbulent flow field has a large impact on stagnation heat transfer.

The effect of free stream turbulence on local mass transfer from a circular cylinder is experimentally investigated by S. Sanitjai, and R.J. Goldstein (S. Sanitjai 2001) at different Reynolds number ranging from 3.0×10^4 to 8.3×10^4, turbulence intensity from 0.2% to 23.7% and integral length scale from 0.8 to 6.3 cm using four turbulence generators. Three of them are grid and other one is a combustor-like turbulence generator. They found that the pattern of mass transfer distribution changes considerably with free stream turbulence. They also studied the effect of a splitter plate on local mass transfer and visualized the flow field near the surface using an oil/lampblack mixture. They also documented the streamwise turbulence intensity and longitudinal length scale variation without the cylinder in position in Figure 5.

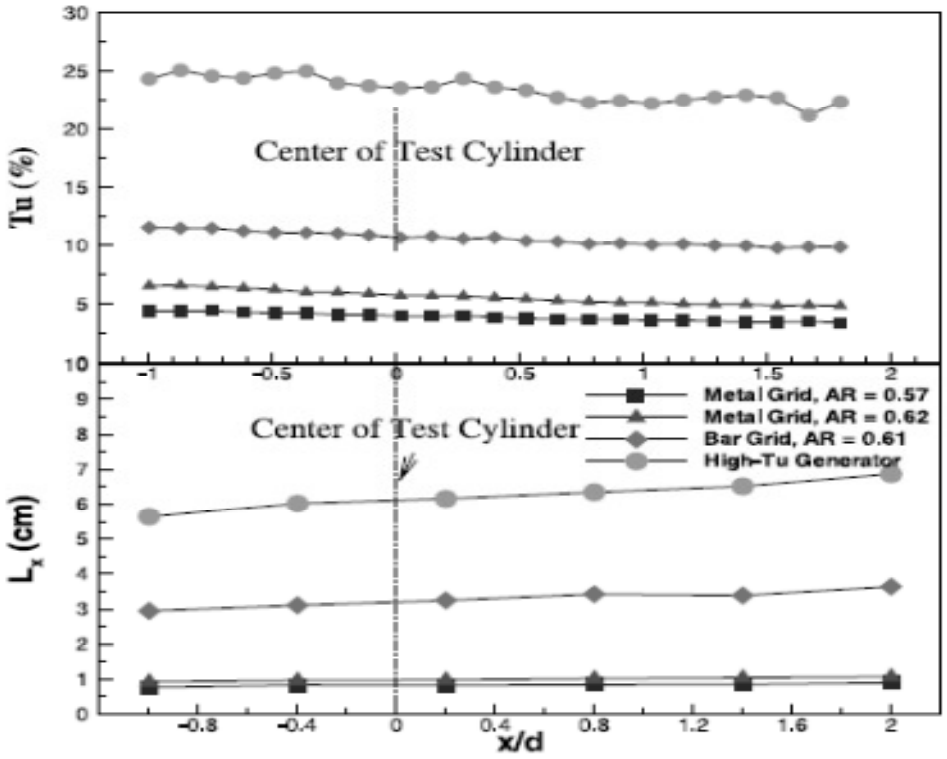

Figure 5: Distribution of TI and Length Scale in streamwise direction (y/d = 0 and z/d = 4.57)

They concluded that the front stagnation line mass transfer changes significantly with the FST and it increases up to 60% as the turbulence intensity goes from 0.2% to 23% at highest Reynolds number. They also described that FST has strong effects on the flow around a cylinder which is why high levels of FST are needed to alter flow characteristics at low Reynolds number. At the end of the paper, they suggested the following correlation included the Reynolds number, Turbulence Intensity and the length scale effects

$$\frac{Sh_{\theta=0}}{Re^{1/2}} = 0.000067 * \left[Tu\, Re \left(\frac{Lx}{d} \right)^{-0.5} \right] + 1.526$$

Van Fossen and Bunker (Van Fossen, G. James and Bunker, Ronald S 2001) measured the stagnation region heat transfer due to turbulence from a Dry Low NO_x (DLN) can combustor, and found that stagnation point heat transfer increased in the presence of turbulence by 77% compared to the laminar case. Their DLN combustor was a can type with 6 fuel-air swirlers, each swirler having 12 large air swirl vanes on the outer side and a 16-vane diffusion tip on the inside. The mock combustor had no dilution holes and no fuel in it, but generated a swirl and high turbulence intensity comparable to a land-based power turbine. The DLN data was significantly underpredicted by Van Fossen's parameter and moderately over predicted by the TRL parameter. Their heat transfer model had a cylindrical leading edge which transitioned to a flat plate surface downstream with 19 heated aluminum strips on the rear of the model. They also included the hot-wire measurements and showed that very high levels of free-stream turbulence were generated, estimated to be spanwise-averaged turbulence intensity of 28.5%.

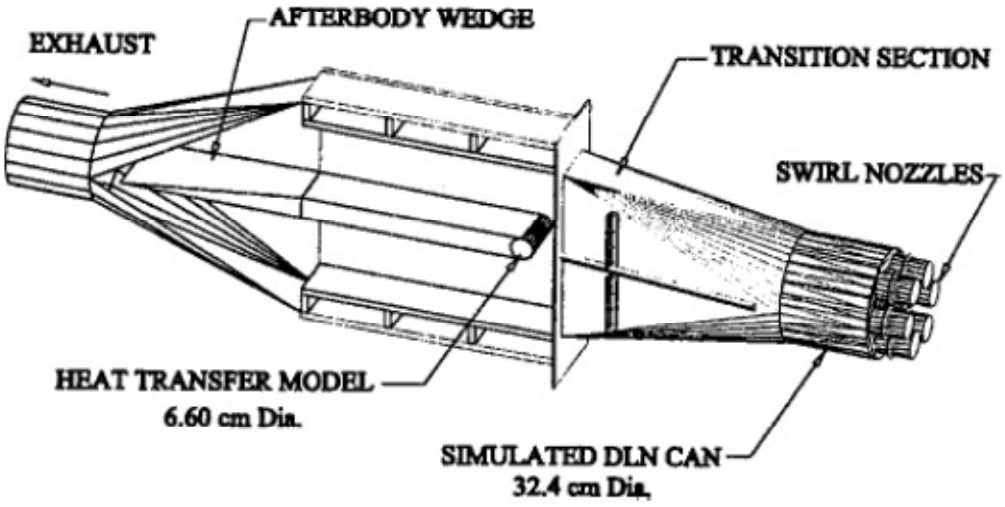

Figure 6: Rig Layout.(Smith, M.C., and Kuethe, A.M. 1966)

Oo and Ching (Oo, A.N., and Ching, C.Y. 2002) investigated the influence of vortical structures in the flow by generating turbulence with uni-planar round rod grids perpendicular and parallel to the stagnation line. Oo and Ching's data did not correlate well with Van Fossen's correlation and improved significantly when a dimensionless vortex parameter was included.

K.A. Thole et al. (K.A. Thole, R.W. Radomsky, M.B. Kang, A. Kohli 2002) also investigated the elevated free stream turbulence effect on the heat transfer for a turbine vane. They have generated an approach turbulence level of 19.5% and compared it with 0.6% turbulence level as a baseline. At the same time, they also made BL measurements for better understanding the effect of high free stream turbulence. They found that the velocity fluctuations were mostly anisotropic and increased in magnitude when approaching the vane. They also found heat transfer augmentation increases 80% along

the pressure side and 25% at endwall compared to the low free stream turbulence (0.6%) case. They compared data based on a range of correlations that were available from the other previous researchers. However, those correlations showed heat transfer augmentation at elevated turbulence levels but still they underpredicted the augmentation level.

Nix and Diller (Nix, A.C., Diller, T.E. 2009) studied the physical mechanism of the augmentation of stagnation point heat transfer from a cylinder by FST. They used five different grids for the purpose of generating a wide range of turbulent intensities, containing different turbulent length scales. They used hot wire to measure the crossflow velocity at different upstream positions of the stagnation point which produced the information regarding the average velocity and fluctuating component including the turbulence intensity and integral length scale. Their fundamental model concept was that, eddies penetrate from freestream through the boundary layer into the surface. The resulting predictions of the analytical model matched well with the measured heat transfer augmentation. And they used the following equation that was previously suggested by Nix et al.(Nix, A.C., Diller, T.E., and Ng, W. F.) to calculate the turbulent heat transfer based on the idea that the increase in stagnation region heat transfer could be correlated based on integral length scale

$$\Delta h_t = \frac{k}{\left[\pi\alpha \frac{\Lambda_x}{u'_{rms}}\right]^{1/2}} \tag{2.1}$$

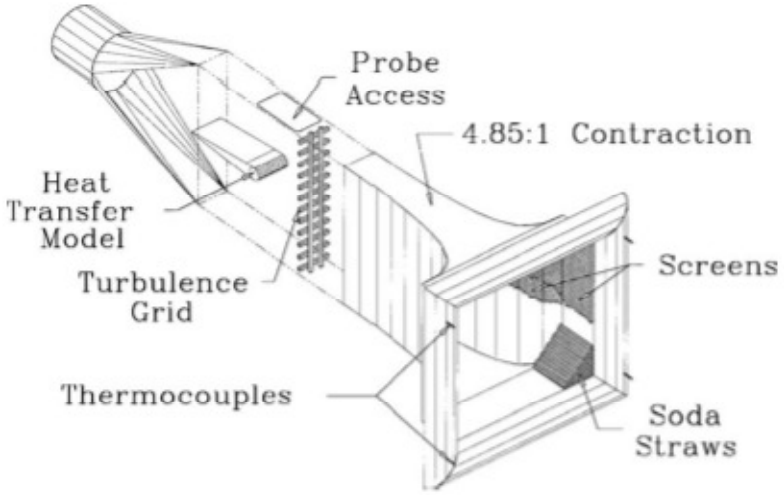

Figure 7: Wind tunnel and turbulence grid used in Nix and Diller's (Nix, A.C., Diller, T.E. 2009) experiment.

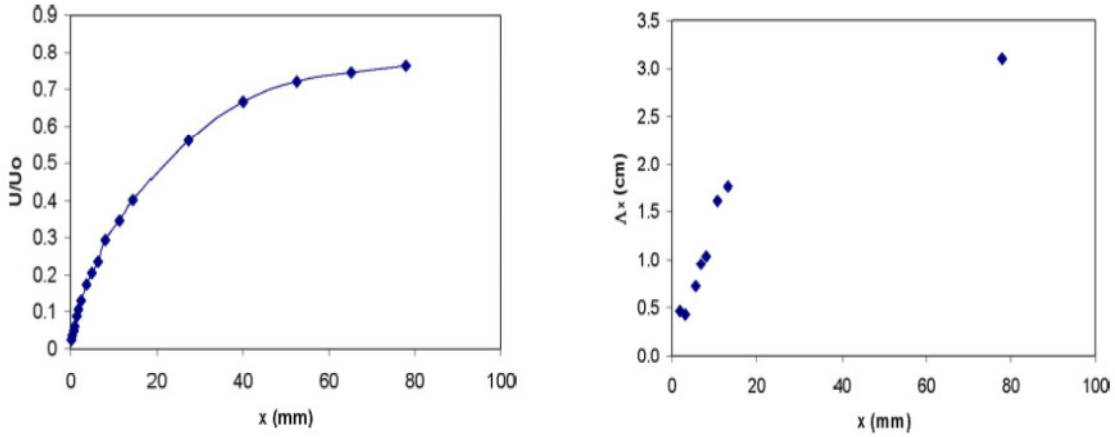

(a) (b)

Figure 8: Velocity profile and Turbulence length scale distribution as a function of distance from the cylinder in Nix and Diller's (Nix, A.C., Diller, T.E. 2009) experiment.

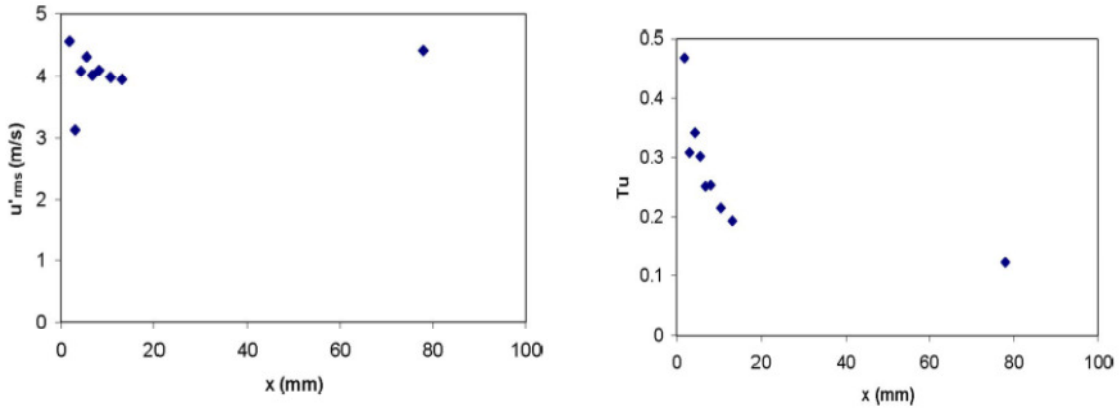

(c) (d)

Figure 9: Streamwise rms velocity and turbulence distribution as a function of distance from the cylinder in Nix and Diller's (Nix, A.C., Diller, T.E. 2009) experiment.

The mean velocity profile as a function of distance (x) from the cylinder showed good agreement with the potential flow solution for the no grid condition. Also the local turbulent intensity increases sharply as mean velocity decreases and so does the length scale, as the cylinder stagnation region is approached. They did not find any noticeable change in the rms velocity fluctuation, u′. The results also indicated a small band of frequencies for that rms velocity fluctuation affect the surface heat transfer. They suggested that the large scale eddies penetrates the boundary layer and gives rise of turbulent heat transfer augmentation reported to be 45-65% higher in their experiment.

Gifford et al. (Gifford, A.R., Diller, T.E., and Vlachos, P.P. 2011) also investigated the heat transfer in the stagnation region subjected to FST. They suggested that the coherent structure of eddies that enters the stagnation region is subjected to amplification and stretching of vorticity. This effect allows eddies to penetrate the momentum and thermal boundary layers with sufficient energy that give rise to the local heat transfer.

2.2 Numerical Investigation of Turbulence Effects Stagnation Region Heat Transfer

S. P. Sutera (Sutera S.P 1965) investigated vorticity amplification in the presence of a stagnation region and its effect on the heat transfer numerically. In his study he extended the work that suggested by Sutera et al. (Sutera S.P., Maeder P.F. and Kestin J. 1963) previously and dealt with more general case. He considered a stagnation point flow containing unidirectional and distributed vorticity of a scale which is 1.5 times the neutral. He found that a vorticity input which increases the wall shear rate by less than 3% can increase the wall heat transfer rate by approximately 40 %. He also suggested that for that given orientation, vorticity is amplified as it approaches the boundary layer and induces significant three dimensional effects within the boundary layer and resulting heat transfer augmentation.

Hunt (Hunt 1973) analytically investigated the response of turbulence in the presence of a circular cylinder body in turbulent cross flow using rapid distortion of turbulence theory (RDT). He performed computations and found velocity spectra for the limiting cases where the turbulence scale is very much larger or smaller than the size of the body. His results suggest that relatively small scales are intensified in the stagnation region strain field and that relatively large scales are attenuated in a manner similar to the mean flow as the flow approaches neat the stagnation region.

Rigby and Van Fossen (Rigby, D.L., and Van Fossen, G.J. 1991) numerically investigated the influence of spanwise variations of freestream velocity on cylindrical stagnation region heat transfer. They found the vorticity introduced by the spanwise

variations amplified near the stagnation region due to vortex stretching. This mechanism can cause periodic arrays of structures similar to horseshoe vortices, which give a considerable rise in the spanwise averaged heat transfer coefficients.

Bae, Lele, and Sung (S. Bae, S.K.Lele and H.J.Sung 2000) performed a series of numerical simulations and found that the amplification of streamwise vorticity enhances stagnation region heat transfer. They imposed sinusoidal disturbances of wavelength, λ, and relative amplitude, *A*, on the free stream analogous to Rigby and Van Fossen (Rigby, D.L., and Van Fossen, G.J. 1991) to examine the effect on stagnation region heat transfer. Their results suggested three regimes which they called (a) the damping regime where $\lambda/\delta < 2.7$, (b) the attached amplifying regime where $2.7 < \lambda/\delta < 5.3$ and (c) the detached amplifying regime where $\lambda/\delta > 5.3$. They defined δ, as the boundary layer thickness for the undisturbed flow. They concluded that in the damping regime, disturbances were damped and heat transfer augmentation was lower. The streamwise vorticity attached to the wall in the attached amplifying regime, and heat transfer, for a given Reynolds number and amplitude, was maximized. In the detached amplifying regime, the streamwise vorticity was remained separate from the wall and the heat transfer augmentation decreased with increasing wavelength. They also compared the results from the attached and detached amplifying regimes with the TRL parameter by Ames et al. (Ames, F.E., and Moffat, R.J. 1990). The data fit the correlation quite well.

The effect of incoming organized disturbances and free-stream turbulence on leading-edge heat transfer was investigated by Z. Xiong and S. K. Lele (Zhongmin Xiong and Sanjiva K. Lele 2007) numerically. They found an optimum length scale to give the maximum heat transfer enhancement for the organized disturbance situation but other

than this optimum value, the enhancement decreases with the increase of length scale. They performed large eddy simulation (LES) with dynamic SGS model at Reynolds number $Re_D = 10^4$ based on upstream approach velocity and the leading edge diameter. They considered homogeneous, isotropic turbulence with intensity $u'_{rms}/u_\infty = 0.08$ and integral length scale of $L/D = 0.1$. They characterized three different regions where the interaction of turbulence impinged on the leading edge. The simulation gave a turbulent heat transfer enhancement of 11%, which they claimed is in fair agreement with the experimental data. Their outcomes also motivated a hybrid simulation strategy where the turbulence outside and away from a blade surface was captured using LES techniques while a finer DNS-like grid was embedded within the near-wall region to resolve the smaller eddies responsible for near-wall effects. Fig. 10 shows the turbulence intensity along the stagnation stream line that they represented from their simulation. The root-mean-square values are obtained by averaging u', v', and w' in time and in the spanwise direction. The turbulence is largely decaying until it reaches a distance of about D from the leading edge where the behavior of u', v' and w' changes. And It is noticeable that close to the body u' and w' are amplified while v' continues to decay. In Van Fossen's (Van Fossen, G.J., Simoneau, R.J., and Ching, C.Y. 1995) experiment, a power law curve of the form $Tu \sim x^m$ was used to fit the decay of free-stream turbulence in the absence of the model versus the distance downstream of the turbulence-generating grid. The power-law fitted curve is also plotted in Fig. 15 with the same exponent m = - 0.83 as used in the experiments. The fairly good agreement indicates that the initial decay rate of the free-stream turbulence has been captured correctly by their simulation.

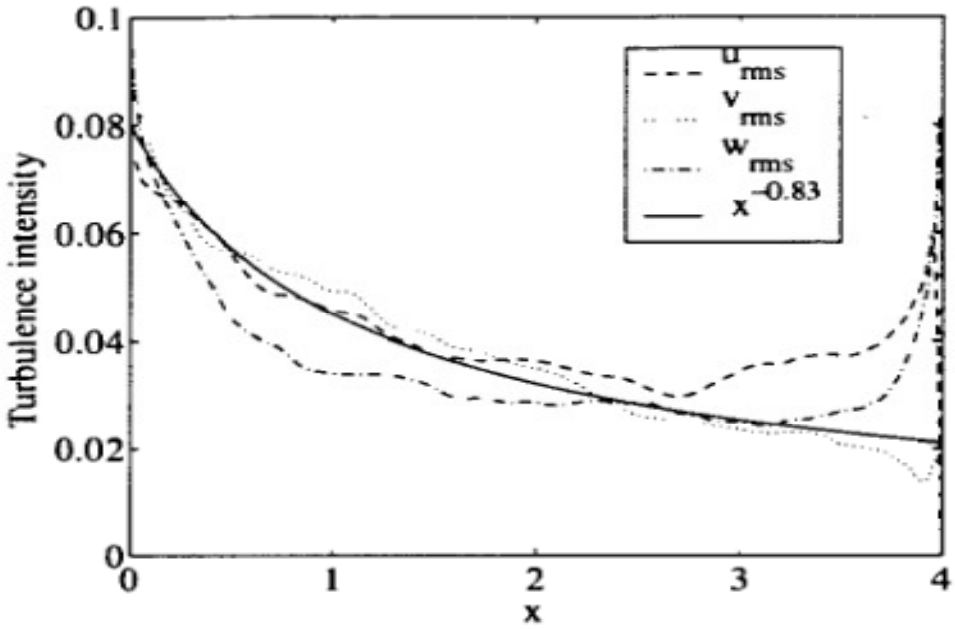

Figure 10: Turbulence intensity along the stagnation streamline (Zhongmin Xiong and Sanjiva K. Lele 2007). The solid line is a power law fit using the same the exponent (-0.83) as in Van Folssen's (Van Fossen, G.J., Simoneau, R.J., and Ching, C.Y. 1995) experiment.

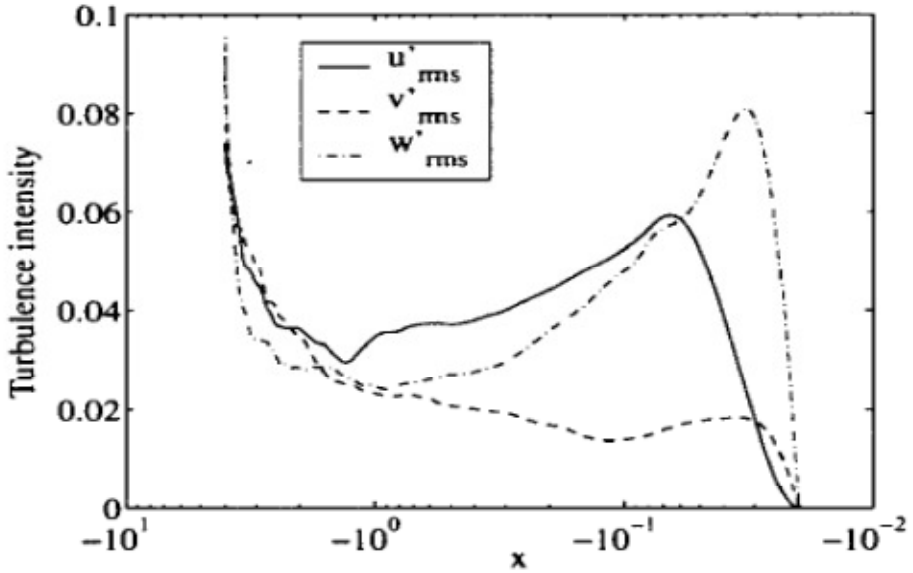

Figure 11: Turbulence intensity along the stagnation streamline, transformed x axis (Zhongmin Xiong and Sanjiva K. Lele 2007).

2.3 Present Viewpoint

The augmentation of stagnation region heat transfer due to flow field turbulence is a scientifically interesting problem with high relevance to gas turbine design. Different investigators have studied this problem and have attempted to rationalize results from a range of different perspectives including empirical, turbulent spectrum based, coherent structure, and numerical. The main focus of this present research is to systematically expand the parameter range into higher Reynolds numbers by using larger diameter cylinders. Stagnation region heat transfer has been studied using these large cylinders with high turbulence levels over a range of turbulent scales. The present study is intended to favor the perspective of references in analyzing and reporting these results. However, the objective is to make this comprehensive data set available to other investigators in this area.

CHAPTER III

EXPERIMENTAL SETUP

This chapter provides a comprehensive description of the experimental set up and the test facility used for acquiring streamwise turbulence data in the presence of the stagnation region. The experimental measurements were captured in a relatively large scale, low speed wind tunnel facility. Two large cylindrical leading edge test bodies were used when turbulence measurements were acquired in the flow field upstream to the stagnation region. Two grids and two mock aero-combustor turbulence generators were used to generate 6 different inlet turbulence conditions for this study. The test bodies allowed Reynolds numbers based on the leading edge diameter and the approach velocity to reach from a minimum of 15,625 to a maximum of 500,000.

3.1Wind Tunnel Facility

The University of North Dakota's low speed, large scale wind tunnel with a Plexiglas test section has been used for the experiments shown in Figure 12. The test bodies were placed inside the rectangular test section made of Plexiglas.

The wind tunnel is an assembly of several pieces of equipment: an inlet filter plenum, a large centrifugal blower, a two stage diffuser, a finned air-water heat exchanger, a screen box, a conventional nozzle with or without a spool which can be

replaced with one of the mock combustors based on the inlet condition developed. Finally, the test section is attached which holds the test body with a traversing system.

Air is brought up inside the wind tunnel through eight filters with a 90 ~ 95% filtering efficiency, mounted in a wooden plenum that is attached to the inlet of the blower. The filters are used to protect delicate downstream instrumentation such as hotwires that can be easily damaged by the presence of dirt particles in the air. A large centrifugal blower from New York Blower (model AF-Forty size 274) with a rated capacity of 6.6 m^3/s airflow at a static pressure rise of 5000 Pa was used to draw the air inside the system. The blower is driven by a 45 kW induction motor using V belts and pulleys. A variable frequency drive is used to adjust motor speed according to the desired Reynolds number at the inlet of the test section.

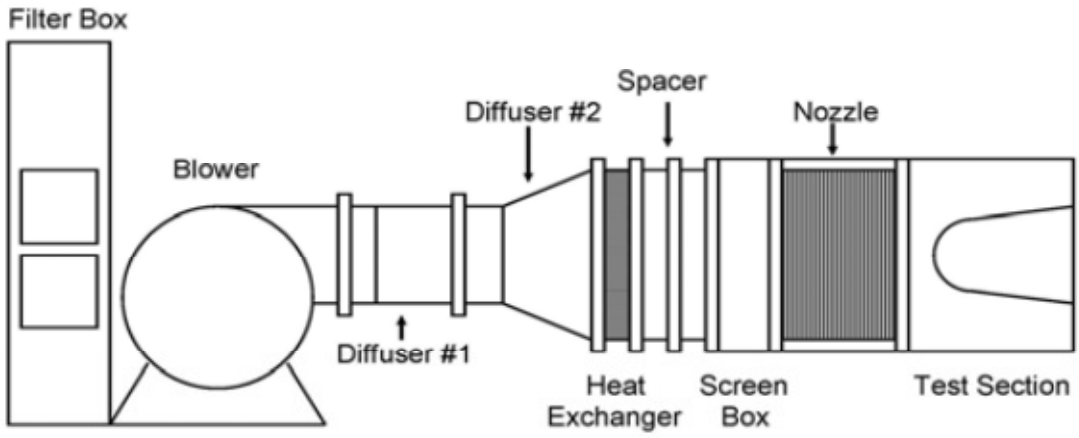

Figure 12: Schematic of Low Speed Wind Tunnel with Cylindrical Test Section.

Air, from the exit of the blower, moves through a two stage multi-vane diffusers. They diffusers are used to recover static pressure by decreasing the velocity of the air.

The diffusers increase the flow area from 16.5″ x 24.25″ (400.125 in^2) to 36″ x 50″ (1800 in^2) in two stages. The dimensions of the diffusers along with design details are reported along with schematic diagrams by (Preethi Gandavarapu 2011).

Air, exiting from the diffusers, flow into an air to water finned tube heat exchanger. The heat exchanger is maintained at constant temperature by supplying a steady stream of re-circulated cooling water. Water was circulated using a 0.5 HP Jacuzzi centrifugal pump that connected to tank with a capacity of 100 gallons as seen in

Figure 13 and Figure 14. Heat is gained by the water which is removed from the system by discharging a small amount from the tank. Cold makeup water is added to the tank continuously to keep a constant water temperature. The makeup water flowing into the tank is regulated by a ball valve to maintain a constant air temperature in the test section for long surveys requiring steady state conditions which can last up to 8 to 10 hours.

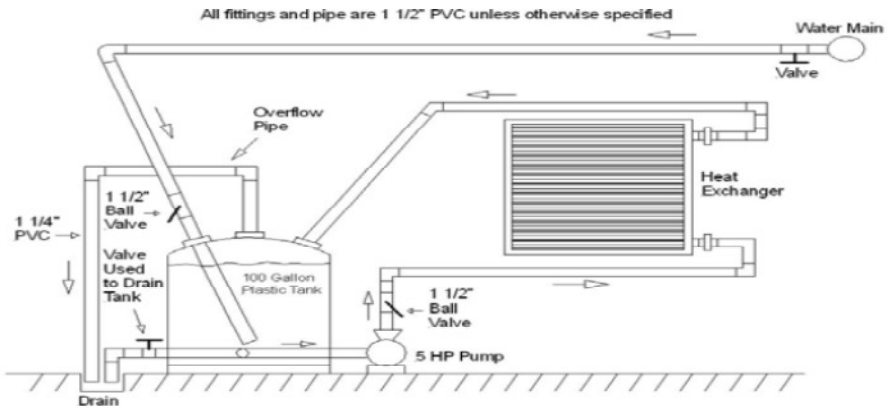

.

Figure 13: Schematic of the heat exchanger cooling water system (Barbot 2003).

Figure 14: Heat exchanger cooling water pump and tank installation (Barbot 2003).

After passing the heat exchanger, air flows into a flow conditioning unit consisting of 4 fine mesh nylon screens spaced at 2″ (5 cm). The screens are used to minimize the velocity variations across the duct. The conditioned air then enters into a 3.6:1 area ratio nozzle or an aero-derivative combustor turbulence generator depending on the turbulence condition required in the test section. Area contraction in the smooth nozzle generates the uniform flow entering the test section by accelerating the air. A rectangular spool made of Plexiglas which contains one of the two grids at different locations is attached after the nozzle to produce grid generated turbulence.

Air flows into the test section after exiting from the nozzle or a turbulence generator. The test section simulates the leading edge of a turbine vane with larger

diameter. The test section is instrumented with an upstream total pressure, downstream static pressure, and total temperature measurement probes. Tunnel approach velocity is calculated using upstream total and downstream static pressure based on a ratio estimated from CFD predictions.

3.2 Turbulence Generators

Gas turbine combustors are expected to generate high turbulence intensities to enhance mixing of fuel-air mixture with hot products to sustain combustion. This elevated turbulence tends to augment heat transfer rates near the stagnation region of the first stage vanes. The relative length scale of turbulence helps researchers and designers understand the influence of turbulence on heat transfer in the stagnation region. To simulate the exit condition from a combustor, investigators have most often used grids to generate turbulence. However, it is also essential to study the turbulence characteristics of combustor exit flows to predict the heat transfer inside the turbine. This experiment has been designed to investigate the evolution of turbulence characteristics in the presence of a cylindrical leading edge of a vane. Various flow fields were generated using turbulence generators and grid turbulence sections with characteristics similar to a realistic combustor. The schematic of the aero-combustor turbulence generator is shown in Figure 17.

The mock combustors have been developed to produce large scale high intensity turbulence that mimics many current gas turbine engine combustors (Forrest E. Ames 1990). Our mock combustor has an inner liner fitted with a slotted back panel to create

wall jets, and it has two rows of tubes that create holes on the side panels to simulate primary and dilution jets. The mock-combustors direct flow through either 2:1or 1:1 area ratio nozzles inlet which increases average flow velocity. Two types of turbulence generators were chosen to investigate the distortion of turbulence in the presence of the cylinders.

3.2.1 *Aero-combustor*

The aero-combustor presented in Figure 15 is designed with two side panels containing holes and a slotted back panel. The side panels have two rows of ten holes with 6.35 cm ID and mounted inside the combustor box using an angle iron bracket. The panels are shown in Figure 15 flashed with the 2:1 inlet contraction nozzle wall. Each hole is lined with a 0.55 cm thick wall tube which protrudes 6.35 cm into the generator box in order to better direct the air flow. The first row serves the purpose of primary holes and is centered 25.4 cm from the inside wall of the back panel. The second row, serves as dilution holes and is spaced 25.4 cm from the first row of holes. The back panel is comprised of two rows of five slots. Each slot is 20.32 cm by 3.175 cm rectangle in size. The slots centerlines are placed 3.81 cm from the outer edges of the panel.

3.2.2. High Turbulence Generator

The high turbulence generator uses the same orientation of side and back panels as the aero-combustor but it is re-scaled by a factor of 2. The holes diameter and the slot

sizes are scaled down by a factor of two and the number of holes and slots are doubled on the panels. Figure 17 shows front and back of the turbulence generators.

The holes are fabricated using 0.38 cm wall plastic tubes which are glued in the holes of the side panel. The hole centers are spaced 12.7 cm and 25.4 cm from the inside surface of the back panel. The slots in the back panel consist of 20 11.3 cm by 1.58 cm rectangular holes in two rows. Similar to the aero-combustor, the holed panels are located on the sides and the slotted back panel is mounted perpendicular to the side panels. The high turbulence generator directs air into the test section without any contraction.

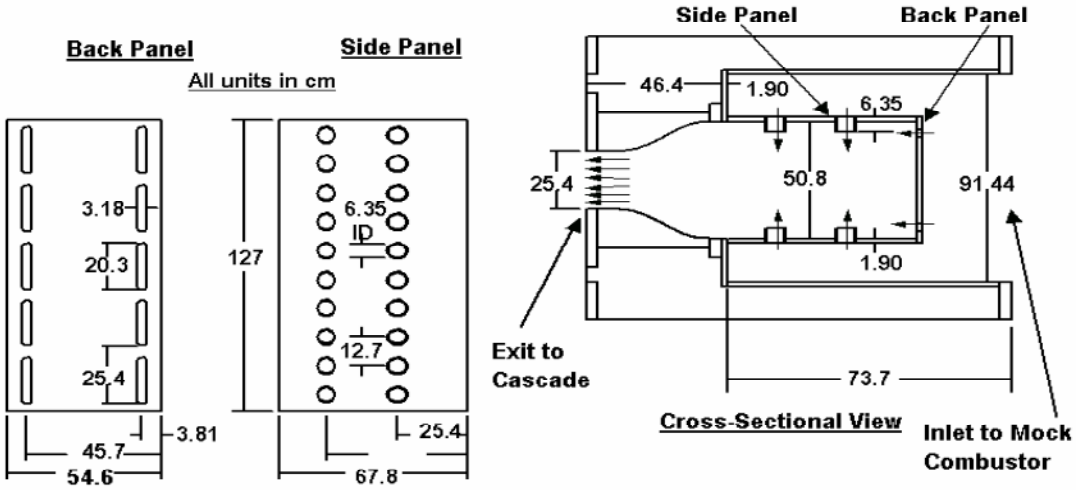

Figure 15: Schematic of aeroderivative combustor turbulence generator.

Figure 16: Front view of Aero Combustor and High Turbulence Generator.

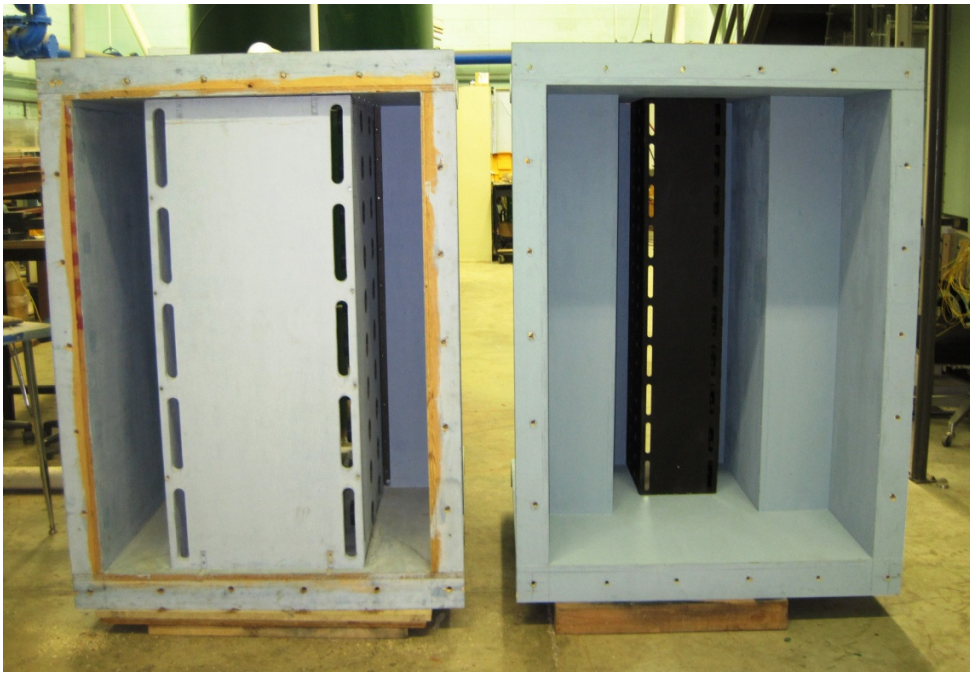

Figure 17: Rear view of Aero Combustor and High Turbulence Generator.

3.2.3 Grid Generated Turbulence

The grid turbulence section uses the 3.6 to 1 area ratio nozzle as well as an additional section in which the actual grid is mounted. Grid turbulence was generated, using two bi-planar, square bar, square mesh grids with a 2:1 variation in size and mesh spacing installed upstream the test section. It is held in a 91.5 cm long x 25.4 cm wide rectangular section joining the nozzle to the test section, with a cross sectional area equal to the test section inlet.

The smaller grid is an assembly of a 0.635 cm square aluminum bar, with a regular mesh spacing of 3.175 cm. This smaller grid was placed at two different locations in a rectangular spool upstream of the test surface- one at 10 mesh lengths and the other at 32 mesh lengths producing turbulence intensities of about 9.2% and 3.1% respectively at the measurement plane 7 cm upstream of the leading edge plane with no cylinder in place. The second grid is larger and fabricated from 1.27 cm square aluminum bars having a spanwise and pitchwise spacing of 6.35 cm producing a 64% open area. The grid was placed at a location of about 10 mesh lengths upstream from the leading edge plane of the cylinder.

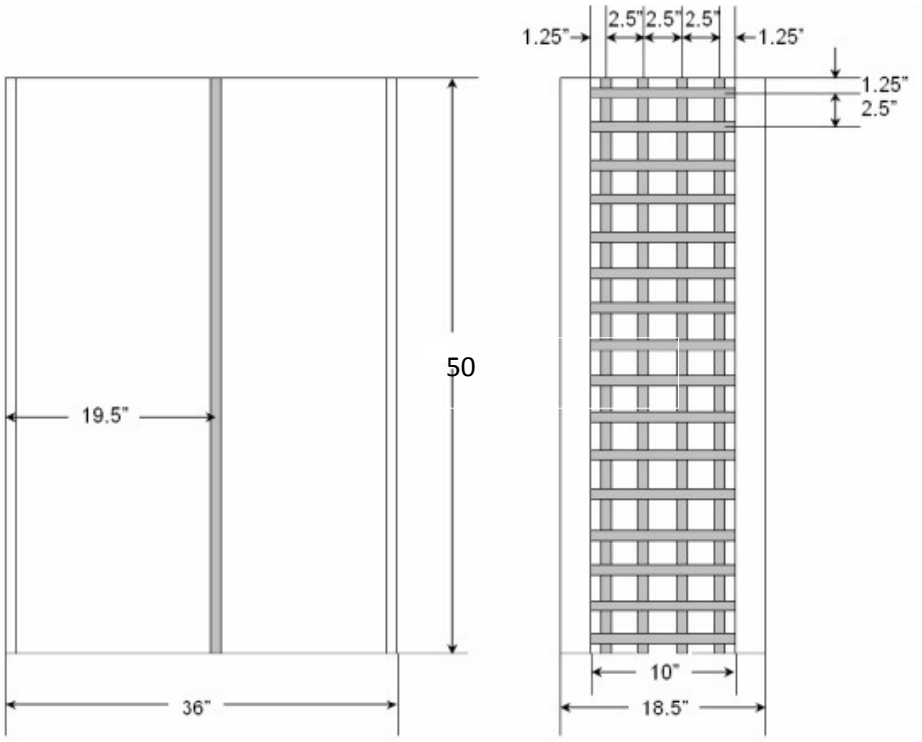

Figure 18: The grid turbulence generator assembly (Indrajit Jaswal 2008).

Both the aero-combustor and large grid turbulence generation sections have been documented previously by Ames et al. (Ames, F.E., Barbot, P.A., Wang, C 2003), (Ames, F.E., Wang, C., and Barbot, P.A. 2003), and (Ames, F.E., Argenziano, M., Wang 2004). Inlet turbulence intensities, turbulent scales, and dissipation rates at different Reynolds numbers for the low turbulence, aero-combustor turbulence, and grid turbulence conditions are summarized in Table 1, Appendix A.

3.3 Traversing Section

A stepper motor driven traversing system from Velmex, Inc. was used to move the hot wire probe holder to different streamwise locations from the stagnation region.

The traversing mechanism was designed and fabricated using a steel tube of 3/8″ diameter that can hold the custom made probe. The center axis of traversing section was aligned with the centerline of the cylinder body. To ensure fewer disturbances in the oncoming flow the probe holder nose was designed based on the potential flow theory. The probe could reach up to 24 inches using the traversing section.

Figure 19 shows a single axis unislide system that can travel 60.96 cm (24 in) in the x - direction. This stepper motors have 400 steps/revolution and lead screws with a pitch of 0.0635 cm/revolution. The unislide was attached with a 63.5 cm x 25.4 cm flat plate which was centered inside the Plexiglas test section. Three windows made of 1.27 cm thick acrylic sheet were placed on one side of the test section to provide access in aligning the components inside the cylinder.

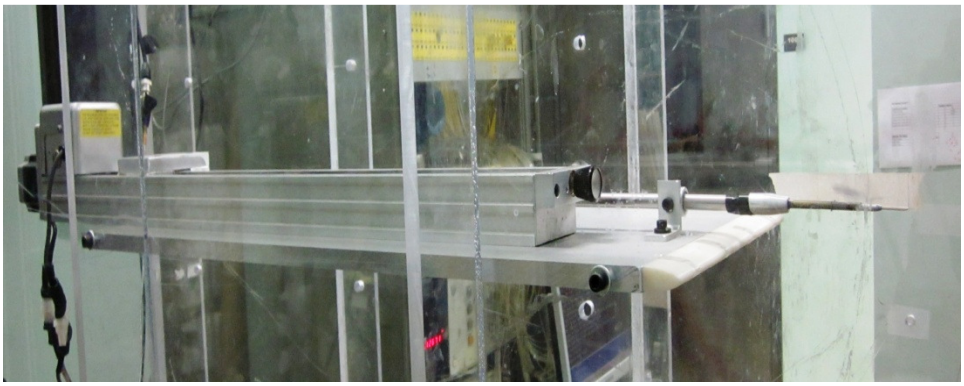

Figure 19: Traversing section inside the testing tunnel.

3.4 Fabrication of Test Bodies

The test surfaces were designed with 0.1016 m and 0.4064 m diameter leading edge surfaces. The cylinders were fabricated out of 1″ polyisocynaurate foam boards, and 0.5″plywood which were covered with 0.38 mm G10 fiberglass epoxy board. In the first step, the foam boards and plywood were cut by using a machined fixture and a router. The foam and plywood were piled up using foam glue up to 10″. After gluing, the cylinder tip was cut by 4″ to set up the modified tip. The tip was assembled with the test surface by securing the tip using screws driven into the plywood. The remainder of the surface was designed to accelerate the flow smoothly along the surface. The half profiles of the geometry for the leading edge surfaces are presented in Figure 20. The predicted surface velocity distributions in Figure 21 initially show a strong region of constant acceleration over the first 30 degrees of the leading edge cylindrical surface where the radius is constant and after that the rate of growth of velocity decreases substantially.

The cylindrical leading edge surfaces were placed inside a 25.4 cm wide by 127 cm high test section. The leading edges of the test surfaces were placed 12.7 cm downstream from the inlet of the 114.3 cm long test section. Figure 23 to Figure 25 are showing the two cylinders after the fabrication.

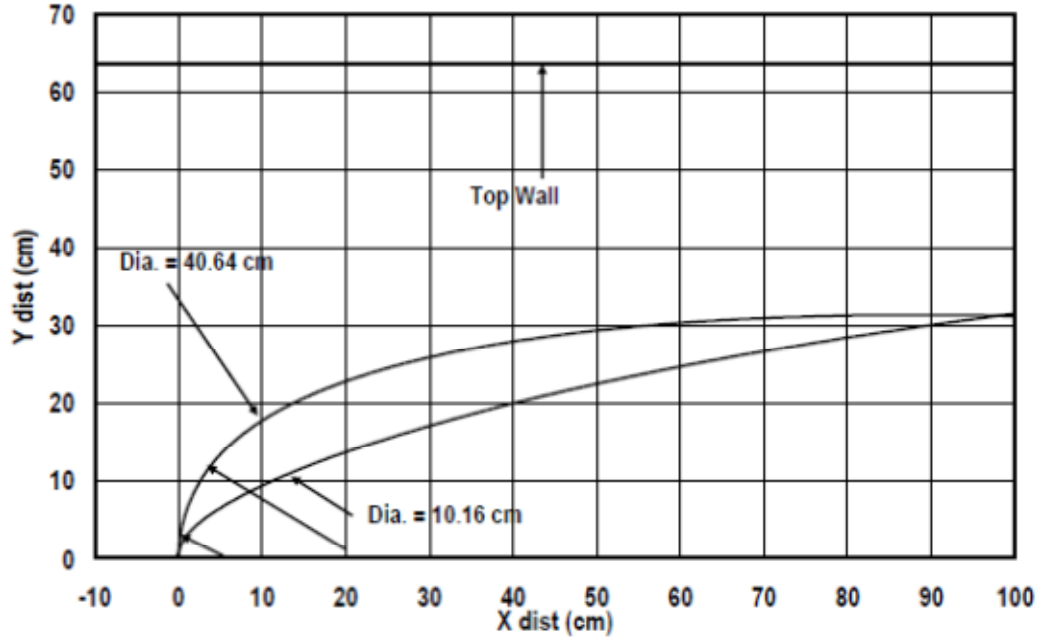

Figure 20: Geometry profiles of the 0.1016 cm (4″) and 0.4064 (16″) cm diameters.

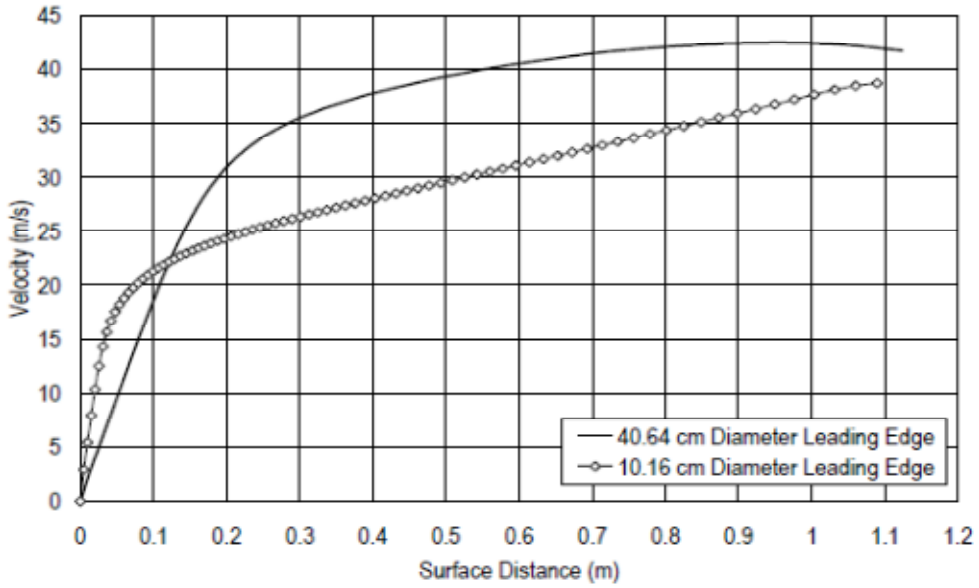

Figure 21: Calculated surface velocity distributions over 0.1016 cm (4″) and 0.4064 cm (16″) diameters.

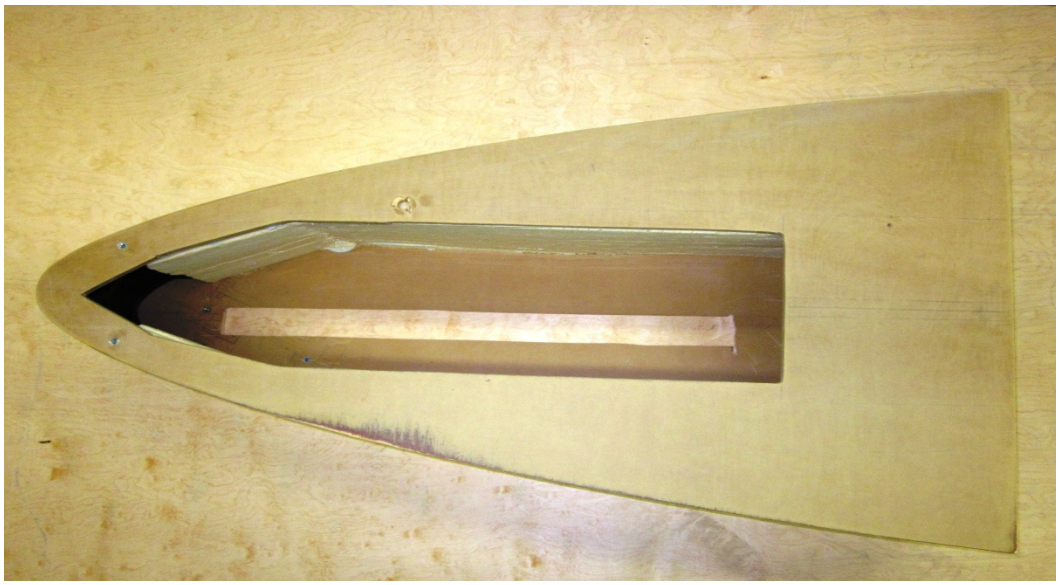

Figure 22: Top view of 4″ diameter leading edge cylinder body.

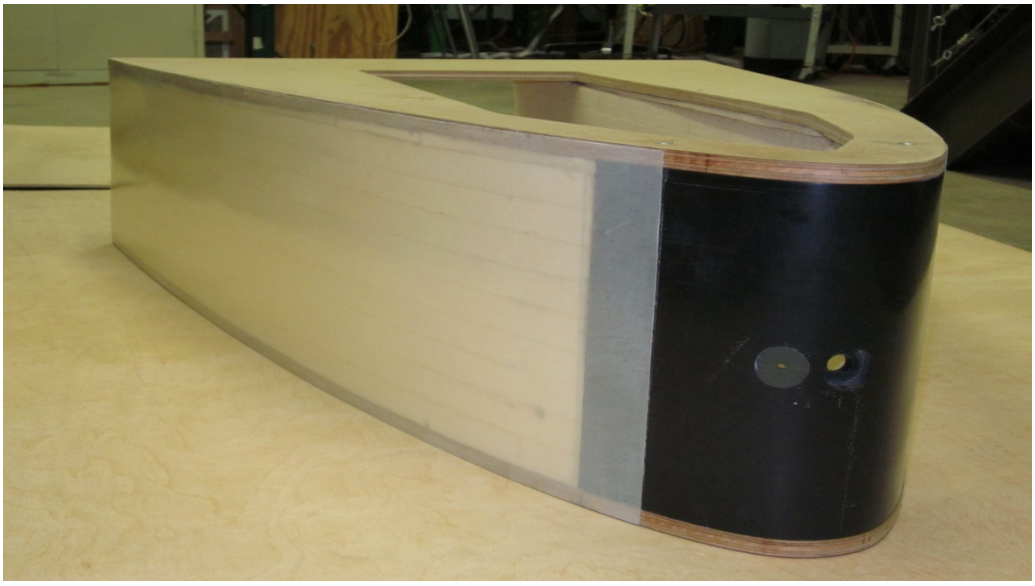

Figure 23: Front view of 4″ diameter leading edge cylinder body with tip.

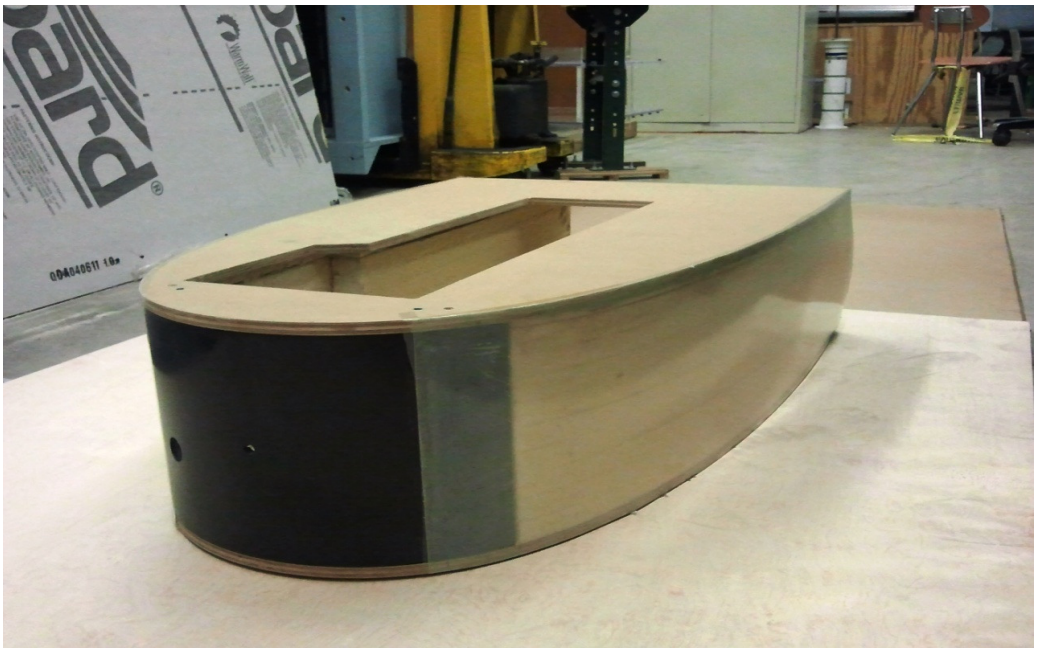

Figure 24: Front view of 16″ diameter leading edge cylinder body with tip.

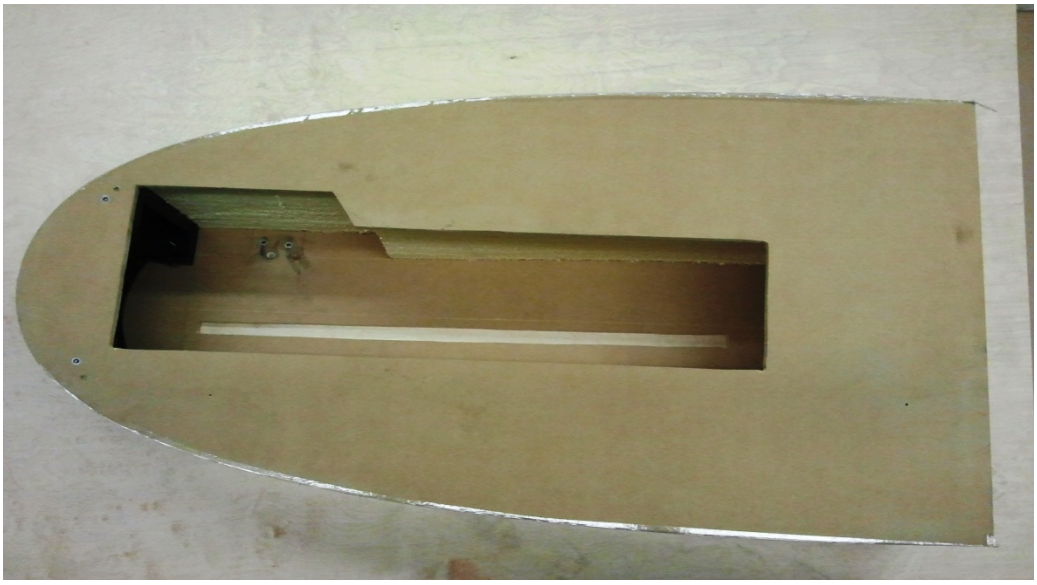

Figure 25: Top view of 16″ diameter leading edge cylinder body.

3.5 Tip design

Cylinder tips were designed separately and manufactured by using a rapid prototype 3D printer facility at UND. For this purpose, we produced highly dense points using several regressions to get a very smooth and nicely fit curve. In both cases, the points are smoothed up to 30^{o}. There were two holes on the tip sections with the purpose of streamwise flow field measurements from the stagnation region and boundary layer measurement for another experiment. Tips were installed in between plywood with the help of drywall screws which are easy to remove and install in the test body. The tips are shown in the Figure 26 and Figure 27.

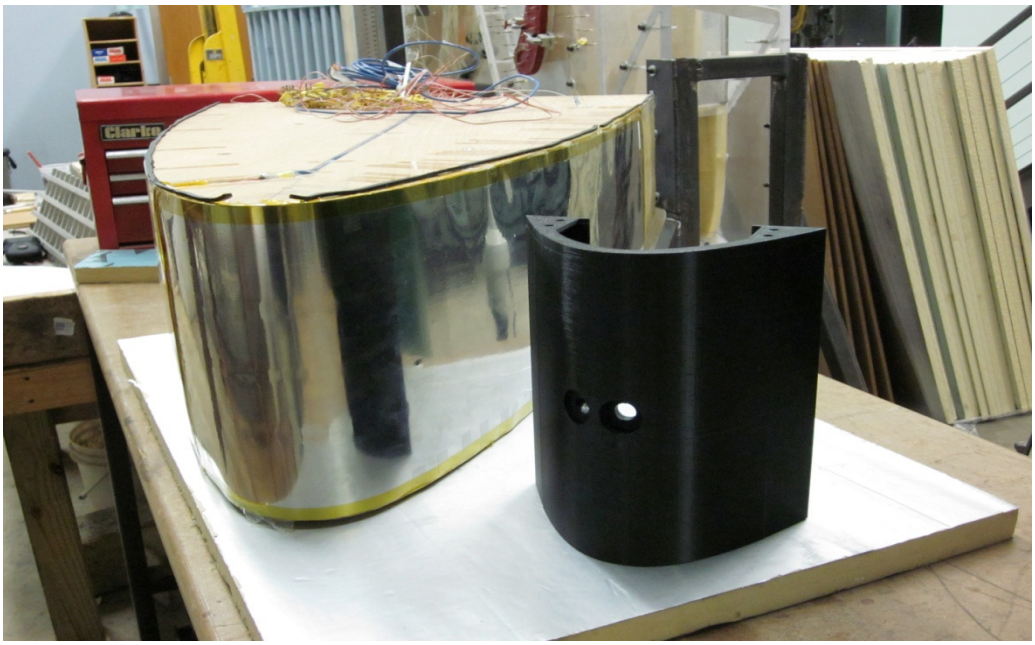

Figure 26: Tip for small (4″ diameter) cylinder.

Figure 27: Tip for big (16″ diameter) cylinder.

3.6 Data Acquisition System

A Dell OptiPlex model GMT-590 computer and a HP 3497A data acquisition unit with an integral voltmeter having 1μV sensitivity were used throughout the experiment to record the temperature and pressure data.

3.6.1Temperature Measurement

Three K type (cromel-alumel) thermocouples were connected to the HP 3497A through a constant temperature reference junction to measure the inlet total temperatures of the tunnel and the ice bath. Thermocouple voltages were acquired using the data acquisition unit. The passive reference junction temperature was measured by a thermocouple immersed in an ice bath.

3.6.2 Pressure Measurement

Two Rosemount pressure transducers with ± 0.1 percent quoted accuracy, and ranges of 250 Pa and 5000 Pa were used to measure the total pressure and the static pressure in the tunnel. They were connected to data acquisition unit through a 48 ports pressure scanner where 44 ports were used on the low side and 4 on the high side. The voltages generated by the pressure transducer were recorded using the HP 3497A unit.

3.7 Hot Wire Measurements

Hot wire measurements were taken using a single wire upstream of the stagnation region at different locations to record the mean and fluctuating velocities. Small steps were taken near the stagnation region. The locations are mapped in Table-3, Appendix B. The x-direction is in the opposite direction of the flow from the stagnation point.

Miniature 55P11 single wire manufactured by Dantec Dynamics was used to obtain hot wire data. According to the Dantec Dynamics catalog (Finn E. Jørgensen 2002), the probe has a platinum-plated tungsten wire that is 5 μm in diameter and 1 mm in length. The prongs of the probe are 5 mm in length. Hotwires must be calibrated before using for the test. The calibration technique is documented in Appendix C explained by Lindsey Dvorak in her master's thesis (Lindsay A. Dvorak 2004).

Traverses in the x-direction were conducted at the exact center location at the stagnation region between adjacent sides. The data was acquired at possible 14 different stations. Initially, it was started from 0.25″ ahead from stagnation region and traversed

incrementally based on the upstream conditions to obtain a complete picture of the flow field.

An IFA 300 constant temperature anemometry (CTA) unit from TSI Inc. was used to operate the hot wire. A 12-bit ADC card named CIO-DAS 16/330 from Measurement Computing Corporation was used to capture the CTA bridge circuit output voltages. Mean velocities and turbulence intensities were acquired using a program written in QuickBasic programming language. Velocity-time data were recorded in 40 sets for each location whereas each set contained 8192 samples. Later, a fast fourier transformation (FFT) was applied to map the time domain information to the frequency domain for spectral analysis.

3.8 Fundamental Data Analysis

A hot wire can respond at very high frequencies which allow it to measure the turbulent fluctuations in the flow. In general, other velocity measuring instruments are less accurate in determining turbulent spectral information in air. The velocity in turbulent flow field varies as a function of both time and space. Therefore, the use of statistics is needed to define any single point values of velocity.

The mean level of a signal, which may represent the average free stream velocity, is denoted by, $\bar{u}$. Mathematically, it can produce an average by summing a series of values

$$\overline{u} = \sum_{i=1}^{n} \frac{u_i}{n} = \lim_{T\to\infty} \frac{1}{T} \int_0^T u(t)dt \tag{4.1}$$

$$\overline{u^2} = \sum_{i=1}^{n} \frac{{u_i}^2}{n} = \lim_{T\to\infty} \frac{1}{T} \int_0^T u^2(t)dt = Mean\ Square \tag{4.2}$$

To get the time average of the square of the fluctuation of the velocity about the mean yields the variance of the velocity, such as

$$\sigma^2 = \frac{\overline{(u - \overline{u})^2}}{n-1} = variance \tag{4.3}$$

$$\sqrt{\overline{u'^2}} = \left[\sum_{i=1}^{n} \frac{(\overline{u} - u_i)^2}{n-1}\right]^{1/2} \tag{4.4}$$

Statistical methods require the independence of u_i. From that view point, it is recommended to wait two or three integral time scales in between two samples to establish independence.

Autocorrelation

The autocorrelation in time is a measure of how well turbulence data is correlated from point to point. There is a high possibility of getting similar value at two points if they are recorded very close in time. But if there any long interval then the probability that the two will have similar values is low. Autocorrelation coefficient is defined as

$$R_E\ (t) = \frac{\overline{u_1(t') * u_1(t'-t)}}{{u'_1}^2} \tag{4.5}$$

Equation 4.5 evaluated at every time interval (t) to generate an autocorrelation curve. The area under the curve given by equation 4.6 is the integral time scale of turbulence and defined as,

$$\tau_E = \int_0^\infty R_E\ (t)dt \tag{4.6}$$

Since the sample size is finite, equation 4.6 is evaluated only at first zero crossing of the autocorrelation curve. The integral length scale can be calculated in two different ways. In this specific experiment, this scale is estimated based on Tylor's hypothesis, given in equation 4.7 which is valid for a range up to u′/U << 1

$$\Lambda_x = U_{mean}.\tau_E \tag{4.7}$$

CHAPTER IV

COMPUTATIONAL PREDICTIONS FOR EXPERIMENTAL SETUP

Heat transfer and aerodynamic loss predictions can be improved if the turbulence characteristics and its response in the presence of a body, such as a cylinder, are accounted for. Detailed upstream turbulence history and flow measurements in the vicinity of a stagnation region are required to investigate the failure of the existing turbulence models in these flow situations. This research will acquire and document a comprehensive set of data including streamwise velocity distribution, turbulent spectral information, and turbulent components.

Computational predictions of flow approaching and over the cylindrical leading edge test surfaces were made in order to properly set up the experiment. Potential flow theory for cylinders in crossflow predicts flow along a stagnation streamline of a cylinder begins to slow well upstream from the stagnation line. This use of cylindrical leading edge regions with after bodies requires CFD prediction for a good estimate of the stagnation streamline velocity. Consequently, CFD predictions were made for each of the cylindrical leading edge test surfaces in order to relate velocity near the exit to the ideal approach velocity.

4.1 Gambit Model

A 2D steady state model shown in Figure 28 was created in Gambit by importing the cylinder vertex data points. The stagnation region of the cylinder was modeled first and then the symmetry condition was applied. A boundary layer mesh was created on the cylinder surface after estimating the boundary layer height for turbulent flow as shown in Figure 30 with a growth factor of 1.34 for 11 rows. Then the edges were meshed. After that, the face was meshed using quad - pave meshing scheme as shown in Figure 29. The inlet was set to the velocity inlet condition and the exit was set as an outflow. The bottom part was considered as symmetry plane to reduce the iteration time. After setting the boundary conditions, the model was saved as 2D and exported as mesh file to use it with Fluent.

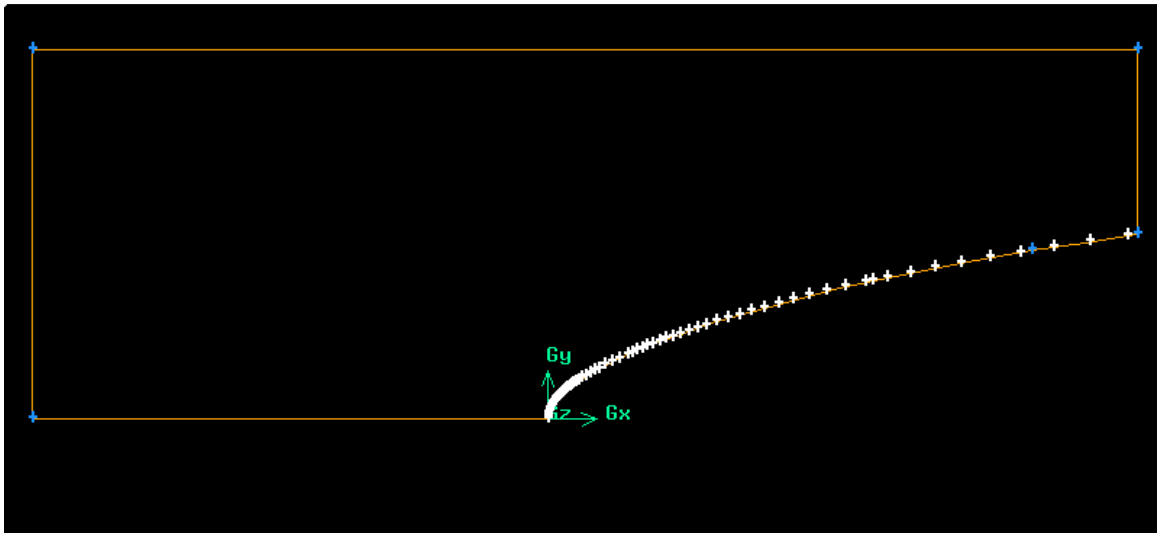

Figure 28: 2D Gambit Model.

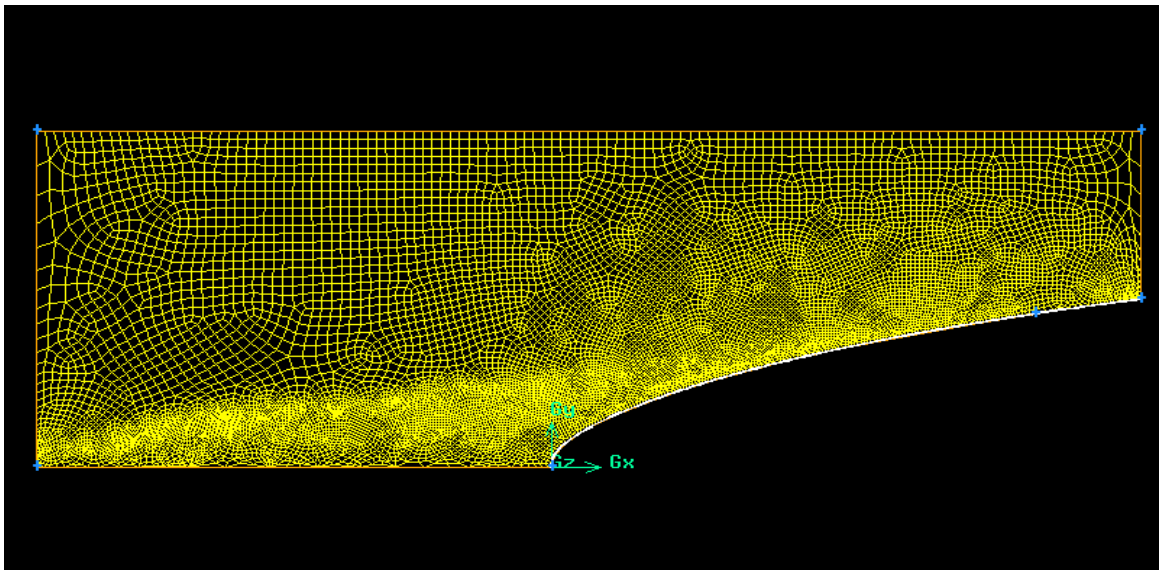

Figure 29: 2D Gambit model with mesh.

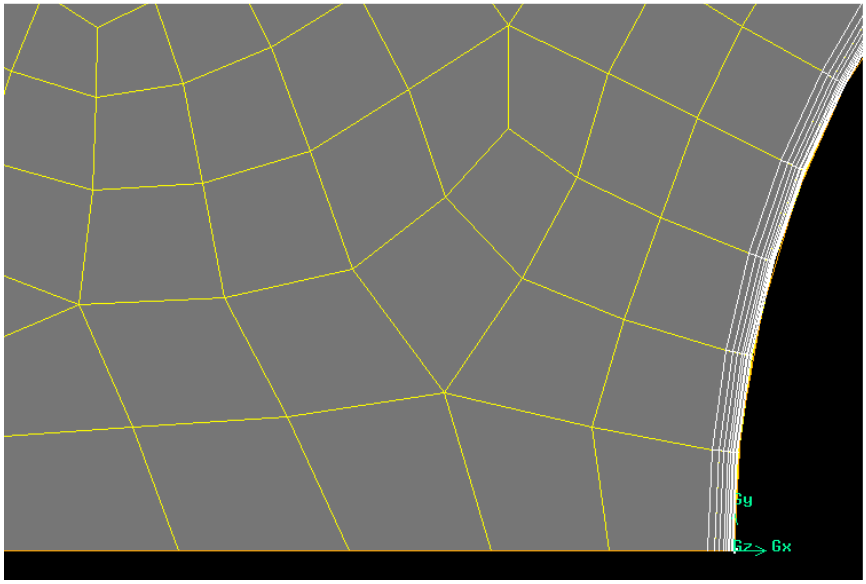

Figure 30: Close view of mesh near the stagnation region**.**

4.2 Fluent Setup

The mesh file was read into Fluent 6.3.26 as a case file. In this regard, Fluent 5/6 solver was used to solve the flow analysis over the cylinder model. Initially, processes such as a grid check and mesh check were performed. Since the geometry is 2-D and quite straight forward, the Spalart –Almaras one equation turbulence closure model was used. The material was set as air with ideal gas condition since it is an incompressible flow for density and Sutherland's law of three coefficient method was defined. At the same time, the energy equation was enabled. An operating pressure of 101, 325 Pa was chosen for the simulation.

Later, boundary conditions were set such as velocity inlet, and outflow keeping all other boundary conditions at default settings. Discretization settings were all changed to second order upwind option and residual monitors were set at 1e-06 to get a better solution.

The solution was then initialized and 10,000 iterations were performed. Shown below are the resulting residual and velocity contours. The solution was converged well in terms of continuity, energy and x-velocity.

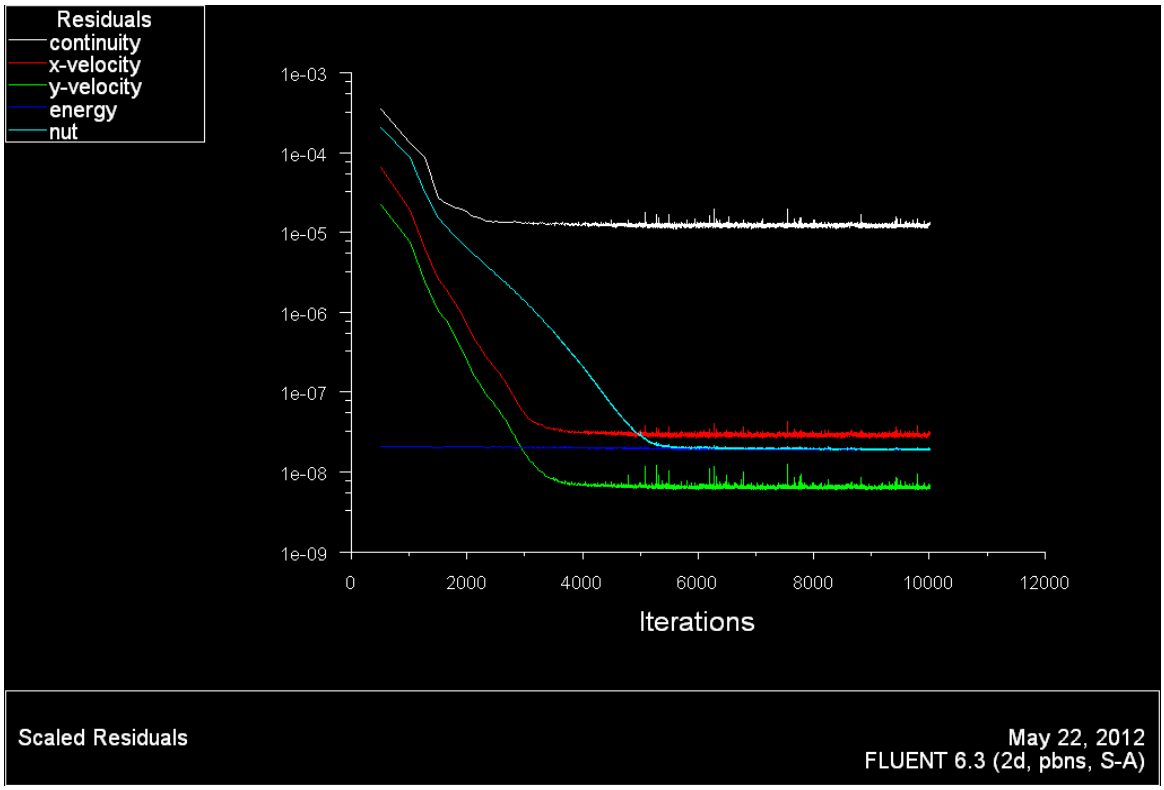

Figure 31: Plot of residuals after 10,000 iterations.

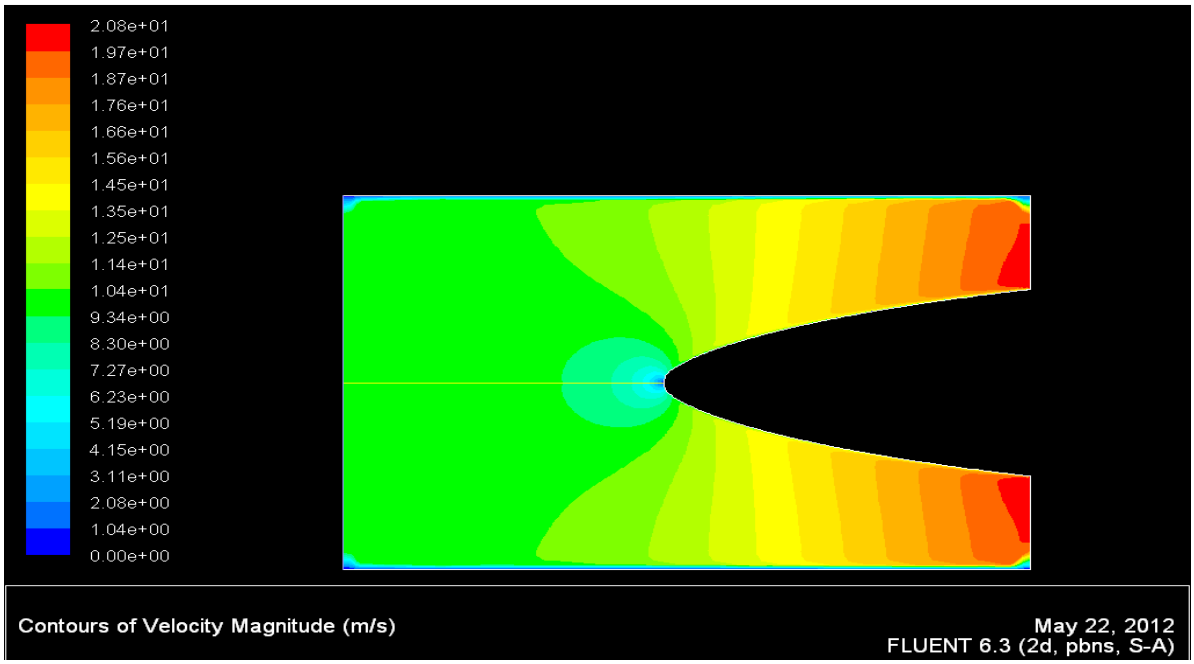

Figure 32: Contour plot for velocity magnitude at inlet velocity of 10 m/s.

CHAPTER V

EXPERIMENTAL RESULTS

This chapter documents the experimental hotwire measurements taken with and without the presence of the large and smaller cylinders. The turbulence generators used and the experimental methodology used for the measurements taken are described in Chapter III. Initially, the turbulence measurements without the cylinders present are described. These measurements include the mean velocity (U), rms fluctuating velocity (u'), the energy length scale (Lu), the integral scale (L_x), the dissipation rate (ε), and where appropriate the one dimensional turbulent spectrum is plotted. Next, turbulence measurements with the cylinders in place are presented. Initially, velocity distributions, acquired using the hotwire are presented as a function of distance from the cylinder and plotted with the velocity distribution predicted with CFD. These provide an indication of the consistency and the difficulty of the near cylinder turbulence measurements. Next, u'/u'_∞ distributions are compared as a function of position comparing the different turbulence conditions. Length scale distributions are also presented to provide information on the evolution of scale as well as influence of the cylinder surface on streamwise energy scale. Comparisons of turbulent spectra are also presented showing some evidence of both wall blocking of large eddies and small scale intensification of the

turbulence. Finally, distributions of normalized dissipation are presented showing both streamwise decay and in some cases significant intensification. These results are discussed as experimental data is presented and summarized at the end of this chapter.

5.1 Test Conditions

Before acquiring the turbulence data, a consistent velocity was maintained to obtain a targeted Reynolds number throughout the experiment by using a tunnel monitoring program at each condition. The tunnel condition was monitored using two downstream static pressures referenced to an upstream Kiel probe. An ice bath reference temperature was developed using a thermos flask filled with ice and water. A thermocouple in an oil filled glass tube was placed in the middle of the flask to sustain constant ice bath reference temperature. The atmospheric pressure was recorded carefully each time, prior to initiating the test.

Experiments were run using the six different turbulence conditions with turbulence intensities ranging from 3% to 16% on the 4 inch small cylinder at four nominal Reynolds numbers (15,625, 31,250, 62,500 and 125,000). For the aero-combustor turbulence condition which generated 13% turbulence condition, the rectangular Plexiglas test section containing the cylindrical leading edge test body was placed just downstream of the exit of its nozzle.

After reaching a specific Reynolds number, the condition was monitored for a while to maintain a steady value till the end of each set of data capture. A similar procedure was repeated for other Reynolds numbers. The next setup of turbulence generating condition was the aero-combustor with a decay spool. This setup generated a

high turbulence intensity of about 9%. A similar procedure was followed for this case as well, keeping all the other remaining conditions constant and hot wire data sets were acquired. The grid generated turbulence condition was generated by first using the conventional nozzle in the place of the aero combustor nozzle. A rectangular spool was placed between the nozzle and test section. The grids were positioned in the spool at different locations upstream of the leading edge of cylinder and generated turbulence of intensities about 3% and 9%. Hot wire data sets were taken following a similar procedure as described above, at this condition. The data sets for the 16 inch diameter cylinder were also captured on the basis of Reynolds numbers at the six turbulence inlet conditions and were used to develop their corresponding individual analysis.

5.2 Single Wire Measurements

Hot wire measurements were taken using a miniature single wire probe. The axis of the wire was positioned perpendicular to the flow direction and parallel to the cylinder axis. The data were captured using a constant temperature anemometry unit. The stations for the traverse were located upstream of the stagnation region. Upstream velocity and turbulence profiles along the stagnation streamline allowed for the determination of the flow characteristics with the presence of different diameter cylinders in cross flow. Turbulent spectra measurements provided energy length scale (Lu), integral scale (L_x), and dissipation levels (ε). The purpose of this study is highly deliberate to offer a database of local fluid dynamics including velocity distributions, turbulent components, and turbulent spectra for leading edge diameter cylinders to support the development of

more accurate turbulence models. In the past, many researchers have investigated length scale effect on the heat transfer but have not reported the upstream turbulence history along with the integral length scale, energy scale and dissipation rate.

The energy scale is defined as $1.5\frac{u'^3}{\varepsilon}$ and is related to the size of eddies that contain the maximum energy in a turbulent flow.

The integral length scale is important in characterizing the structure of turbulence. It is value that quantifies the integral distance of instantaneous flow velocities that are correlated between two points in the flow field.

5.3 Description of the Flow Field

The hot wire traversing system was started as near as possible (0.25″) to the stagnation surface. It was then traversed with an increment of 0.25″ at the first increment then 0.50″ increments up to 2″ to provide a clear view closer to the wall. After that it was traversed with an increment of 1″ up to a certain range based on the inlet conditions which are outlined in the Table-2. Smaller steps in the near wall region were made to get a better view of the velocity profile. The velocity-time data were taken using a miniature single wire 55P11 aligned parallel to the flow and were recorded for each station 40 times (8192 points on each file). The data were analyzed using a Fast Fourier Transformation (FFT) algorithm and averaged to obtain the one dimensional power spectrum of u′ in the flow.

5.4 Turbulence measurements without the cylinders

The local turbulences were measured from the location without the cylinders at place. They are plotted in the

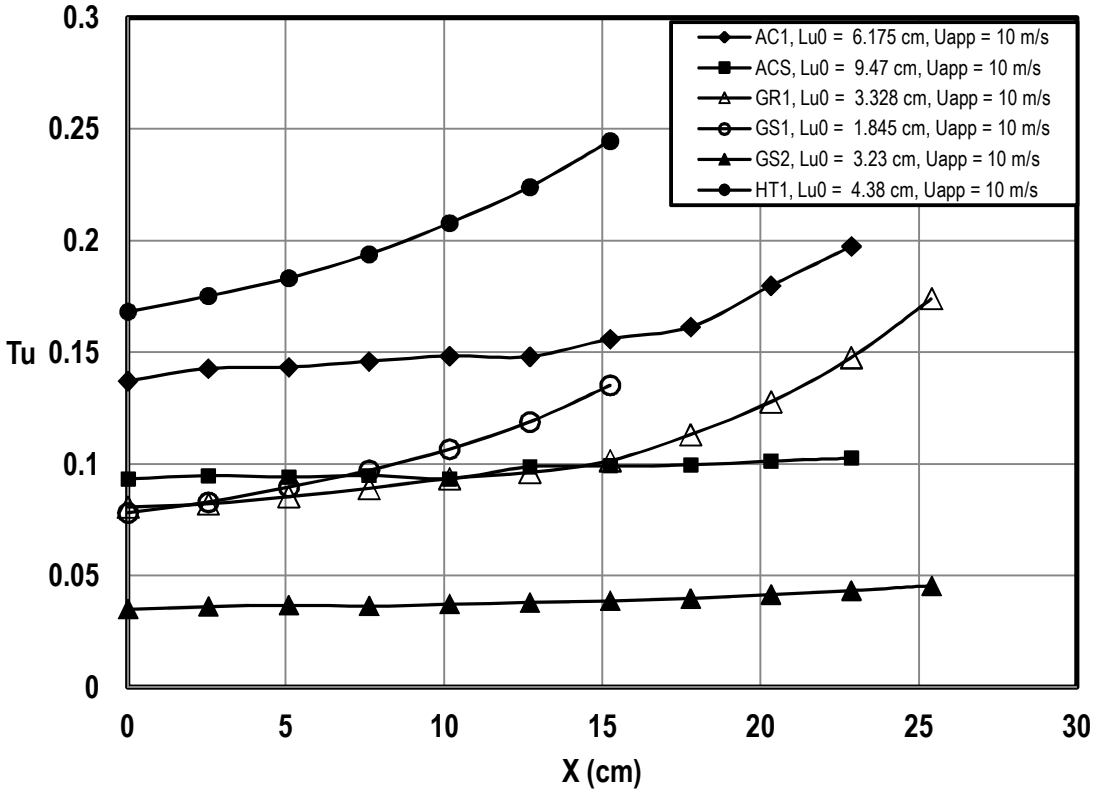

Figure 33 as a function of distance from the stagnation point for 10 m/s. The figure shows the decay of turbulence as the flow approaches the stagnation point. Since without the cylinder there is no reasonable mean velocity gradient, the rms value of fluctuating component represents the local turbulence distribution trend as well. The high turbulence generator, the small grid at near location, and the big grid showed higher decay rates compared to other conditions. The decay rate is higher due to a relatively small turbulent scale combined with a relatively high level of turbulence. Turbulence decay can be

calculated from the simplified form of the turbulence kinetic energy transport equation where turbulence is considered as isotropic and neglecting other terms

$$\frac{1}{Tu} = \frac{1}{Tu_{\infty}} + \frac{x_2 - x_1}{2LuU_{\infty}}$$

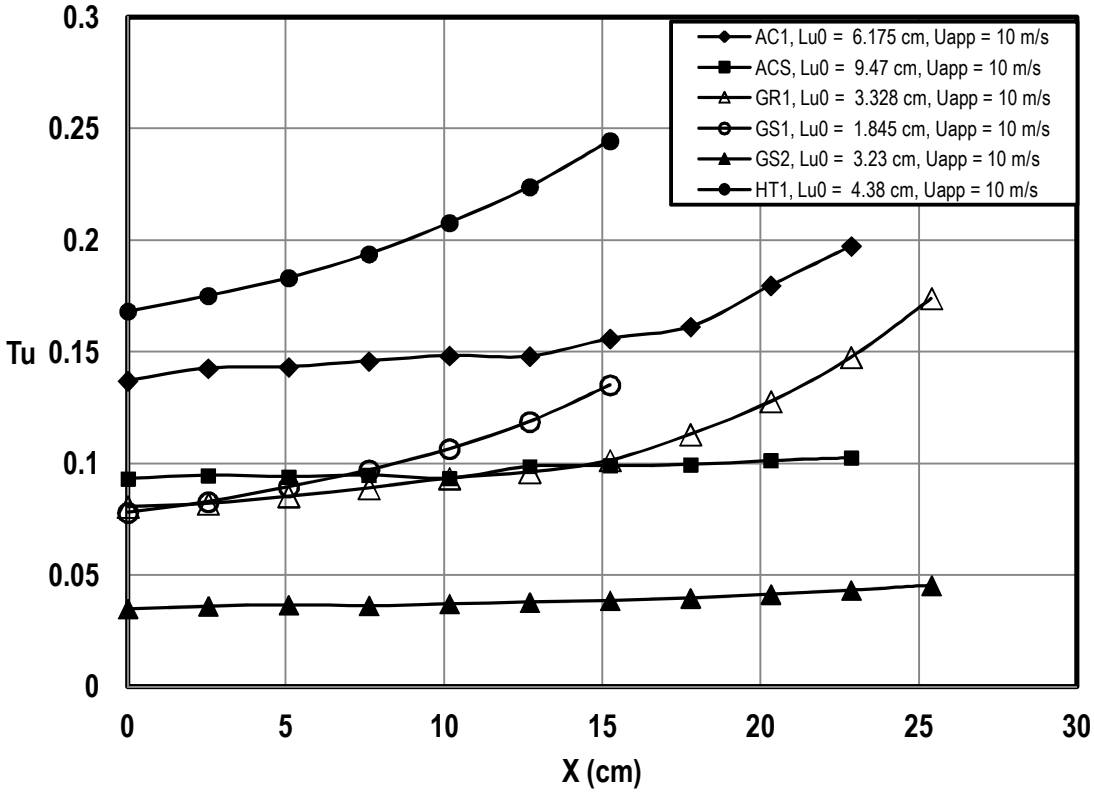

Figure 33: Streamwise local turbulence distributions in the upstream from the stagnation point at 10 m/s.

Energy scales and integral length scales streamwise distributions are plotted in Figure 34 and Figure 35 respectively. They suggested slight increasing trend as the flow moves toward the stagnation point from the inlet plane. This means that the average size of the energy containing eddies is growing bigger with the distance from the turbulence generating plane.

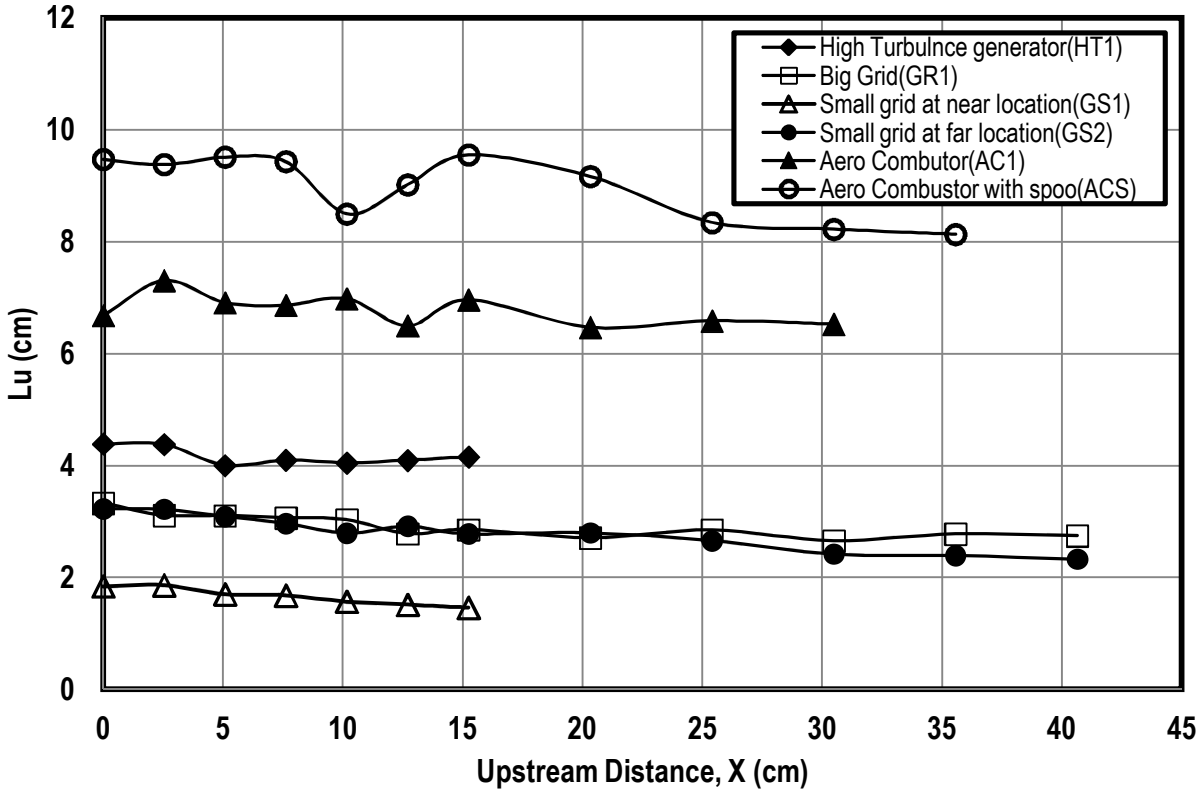

Figure 34: Energy scale plot along the stagnation streamline upstream of the stagnation point at 10 m/s.

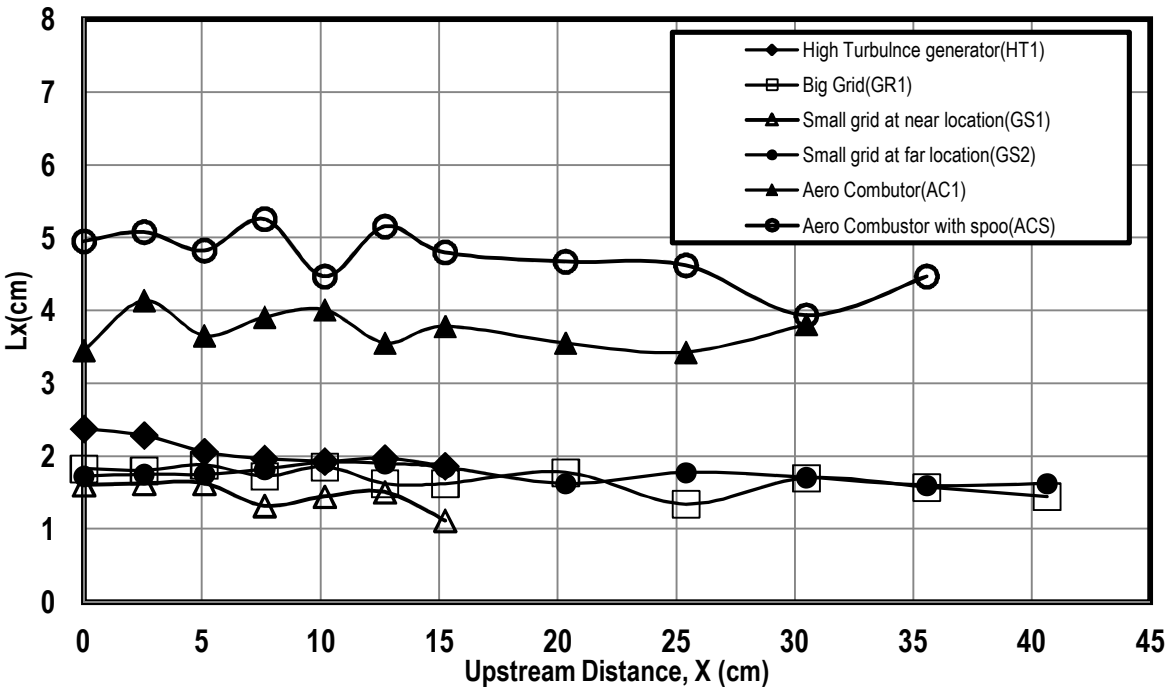

Figure 35: Integral length scale plot along the stagnation streamline upstream of the stagnation point at 10 m/s.

Dissipation rate is also plotted as the function of distance in the Figure 36. The dissipation of turbulent kinetic energy decreases systematically as the flow approaches near the stagnation point. As expected, the kinetic energy decays far from the turbulence generating plane and that can be measured by estimating the dissipation rate from the spectral plot using the -5/3 slope matching in the inertial subrange.

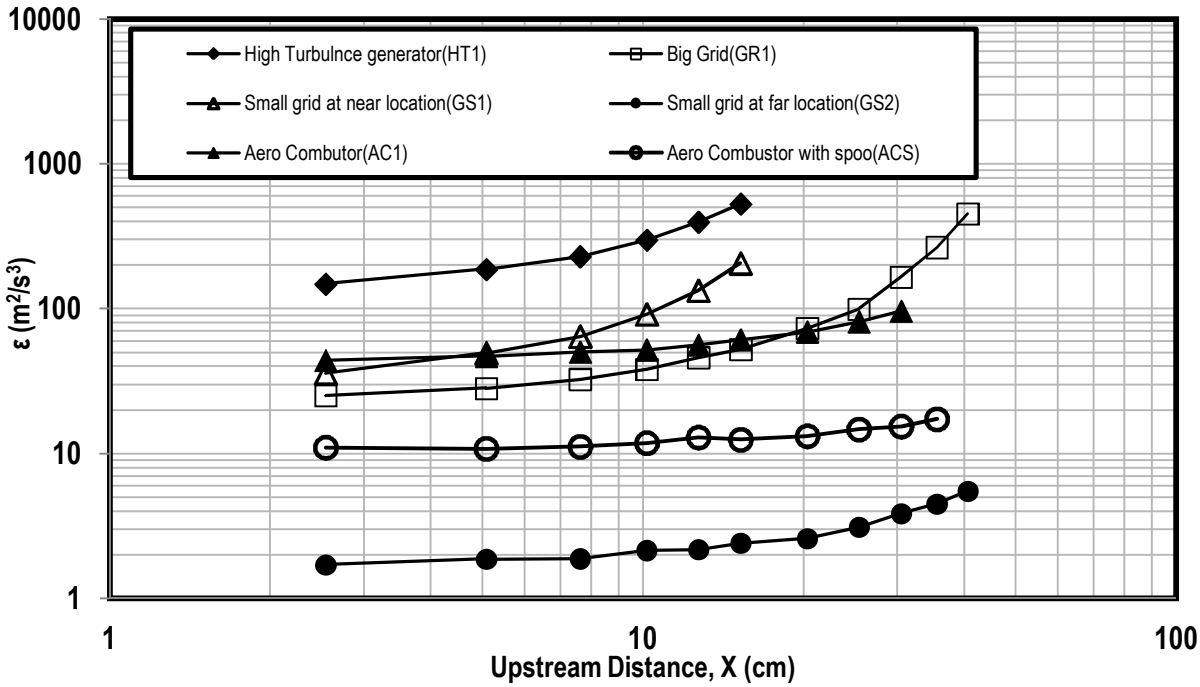

Figure 36: Dissipation rate distribution along the stagnation streamline upstream of the stagnation point at 10 m/s.

5.5 Mean Velocity Distributions

Streamwise mean velocity profiles at different turbulence conditions for four different Reynolds numbers have been taken in consideration with the presence of the cylinder bodies in position. In Figure 37 through Figure 48, the dimensionless mean velocity distributions are plotted as a function of upstream distance from the stagnation point. They are also compared with the data obtained from the CFD calculation using the Spalart - Alamaras one equation model to see how the measurements vary due to turbulence. As expected, the approaching flow velocity decreases as the probe moves closer to the leading edge. But in the experiment, the hot wire results deviated from this trend due to hot wire errors caused by unsteadiness or the presence of high straining field.

The dimensionless velocity distributions for every case are very much similar at different Reynolds numbers and they collect together with minimum uncertainty except for a few cases.

Figure 37 and Figure 38 show the approaching flow profiles for the small and big cylinders. In both cases, the experimental data deviated from the predictions by the CFD code due to errors caused by high levels of turbulence for the aero-combustor case. Initially, they indicated a good agreement but the hot wire measurements showed increasing unsteadiness error as soon as they approached the stagnation region. The unsteadiness encountered due to transverse fluctuating component normal to wire. As the flow approached near the stagnation region, the mean velocity goes down which gives rise in local turbulence intensity. As a consequence, the transverse fluctuating component starts contributing to the streamwise velocity measurements which impacts the single wire performance by introducing errors.

For the case of aero combustor with decaying spool, the mean velocity distributions in Figure 39 and Figure 40 for both cylinders showed good agreement with the CFD predictions. But closer to the wall about 0.5″ far from the stagnation region experimental values showed deviation from the prediction due to high relative unsteadiness resulting from reduced mean velocity and possibly from the rapid straining and vortex stretching. The similar profiles are also observed in Bearman (P.W.Bearman 1972) and Van Fossen's (Van Fossen, G. J.& Simoneau, R. J. 1987) experiments as flow approaches near the stagnation region. The big grid generated turbulence condition also showed the same trend as the aero-combustor with decaying spool as well. They agreed

well with the prediction for the most part except in the near wall region as shown in Figure 41 and Figure 42.

Again, small grid turbulence at two different locations produced two different turbulent scales. The grid at the near location showed good agreement with the CFD analysis for the both cylinders in Figure 43 and Figure 44. The grid at far position condition is slightly overpredicted by the CFD code for the both cylinders in Figure 45and Figure 46. The error in the effective mean velocity was caused by unsteadiness as the flow approached the proximity of the stagnation region resulting from the high FST.

In all cases, the mean velocity is most likely correctly predicted but the hotwire data has encountered some errors that discussed earlier. Additional sources of error can be the vibration as the hot wire probe moved closer to the stagnation region. The probe support was designed with differential diameters due to the smaller diameter of hot wire probe. Moreover, the ID of hole on the stagnation region was 3/8″. In this condition, there was no contact in between probe support and the hole on the stagnation region. That looseness might be a reason for the probe to vibrate in the presence of FST which allowed hot wire to sense some false velocity magnitude vectors responsible for adding uncertainty in the data set.

At the high turbulence generator condition, the small cylinder data fit the predicted mean velocity distribution quite well in Figure 47 whereas, big cylinder showed remarkable deviations from the predicted line in Figure 48. There was a high unsteadiness encountered due to blockage effect due to the presence of the large stagnation region.

Unsteadiness, spanwise variation in local velocity and the vibration in the probe due to high FST contributed a significant amount of variation in the measured and predicted values near the stagnation region. Due to these errors, some points are not documented closer to the stagnation region to avoid complexities in understanding. A rough estimation of those errors is described in appendix C.

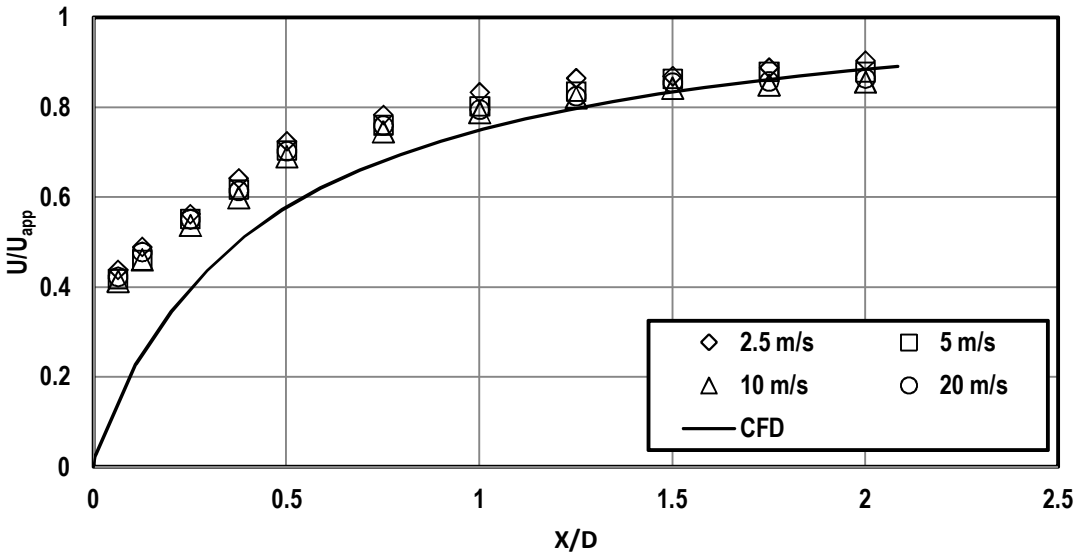

Figure 37: Dimensionless mean velocity distribution along normalized upstream distance from the cylinder stagnation point at four different Reynolds numbers for aero combustor (AC1) for 4″ cylinder.

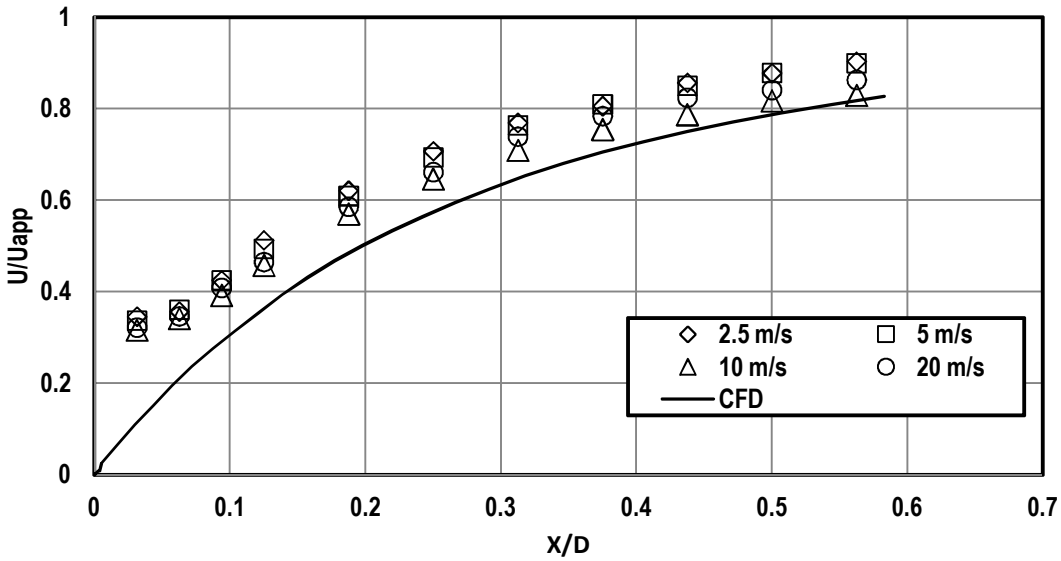

Figure 38: Dimensionless mean velocity distribution for 16″ cylinder along normalized upstream distance from the cylinder stagnation point at four different Reynolds numbers for aero combustor (AC1).

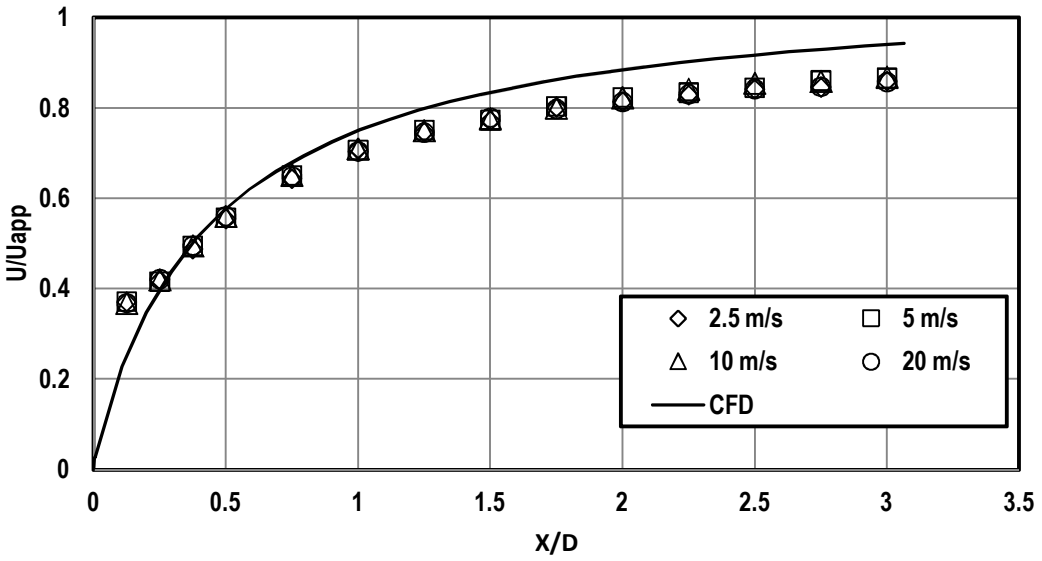

Figure 39: Dimensionless mean velocity distribution for 4″ cylinder along normalized upstream distance from the cylinder stagnation point at four different Reynolds numbers for aero combustor with spool (ACS).

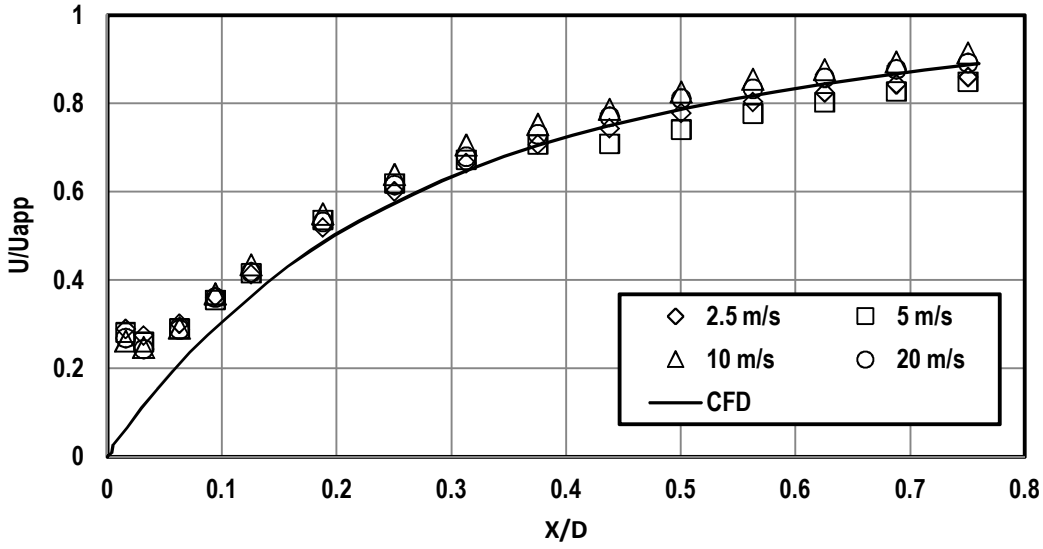

Figure 40: Dimensionless mean velocity distribution for 16″ cylinder along normalized upstream distance from the cylinder stagnation point at four different Reynolds numbers for aero combustor with spool (ACS).

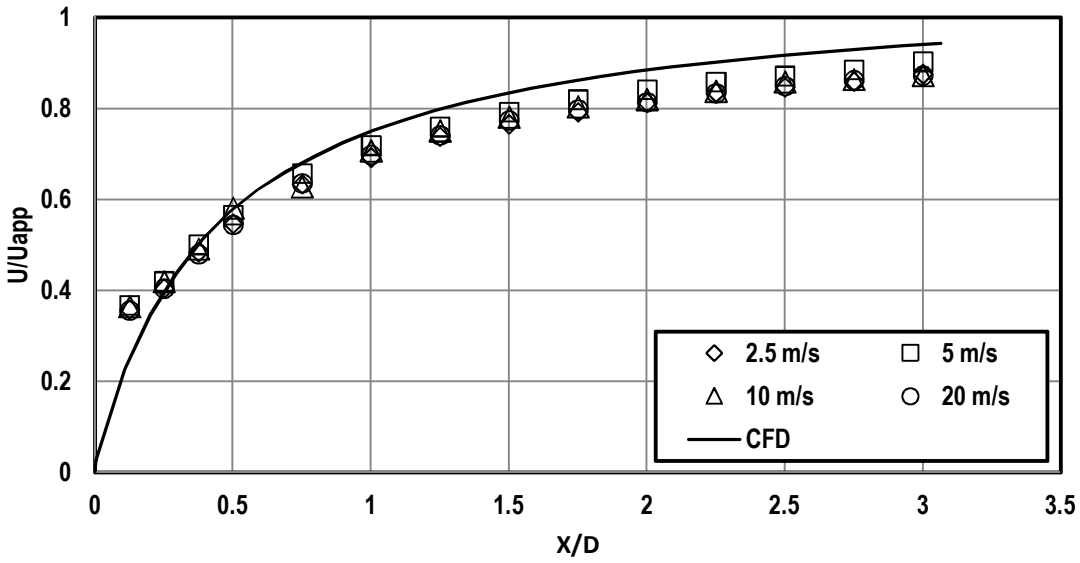

Figure 41: Dimensionless mean velocity distribution for 4″ cylinder along normalized upstream distance from the cylinder stagnation point at four different Reynolds numbers with big grid (GR1).

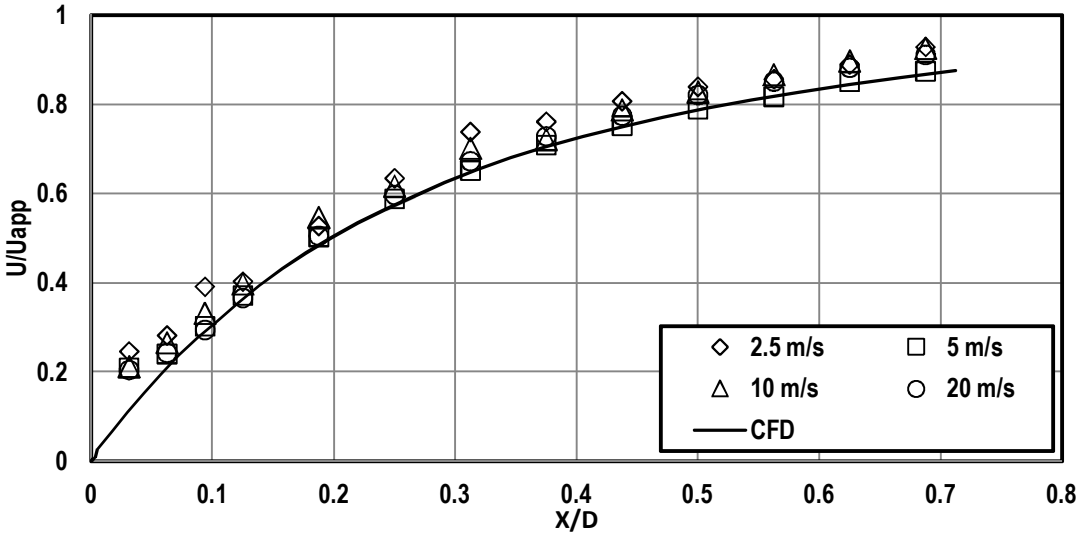

Figure 42: Dimensionless mean velocity distribution for 16″ cylinder along normalized upstream distance from the cylinder stagnation point at four different Reynolds numbers with big grid (GR1).

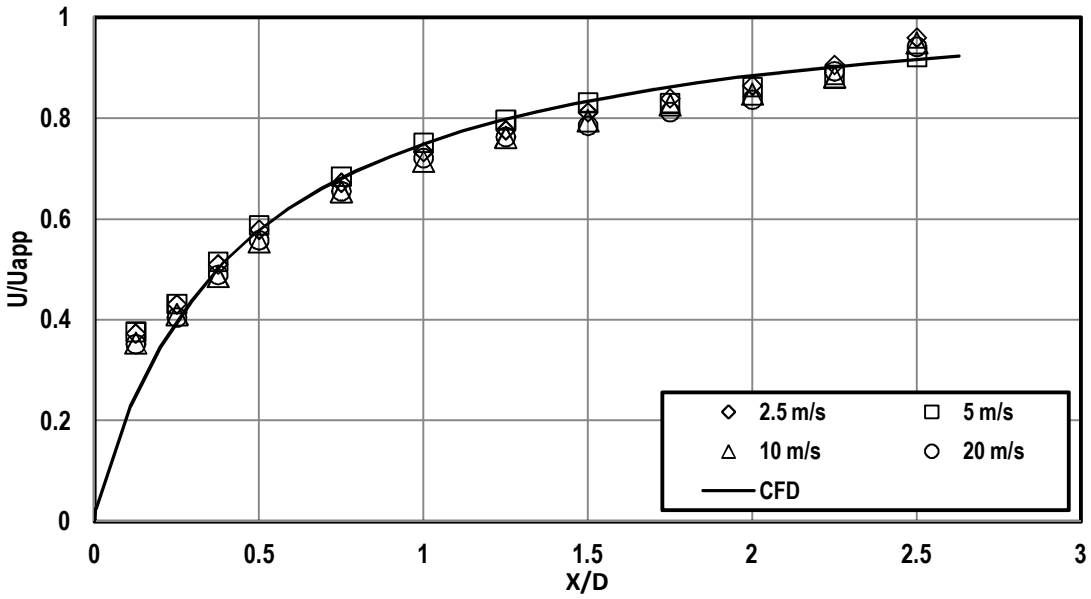

Figure 43: Dimensionless mean velocity distribution for 4″ cylinder along normalized upstream distance from the cylinder stagnation point at four different Reynolds numbers with small grid near (GS1).

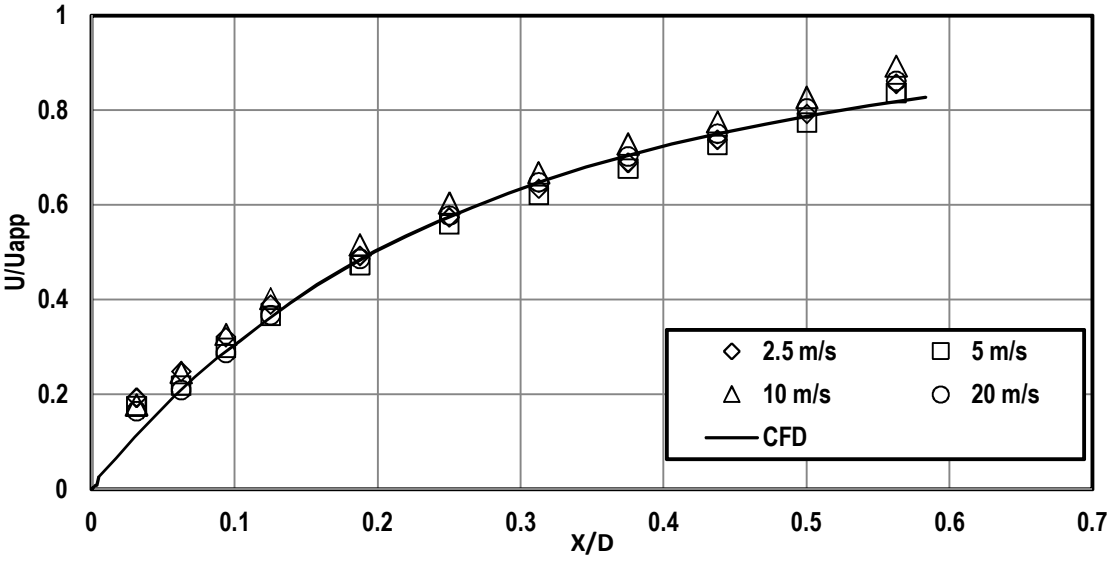

Figure 44: Dimensionless mean velocity distribution for 16″ cylinder along normalized upstream distance from the cylinder stagnation point at four different Reynolds numbers with small grid at near position (GS1).

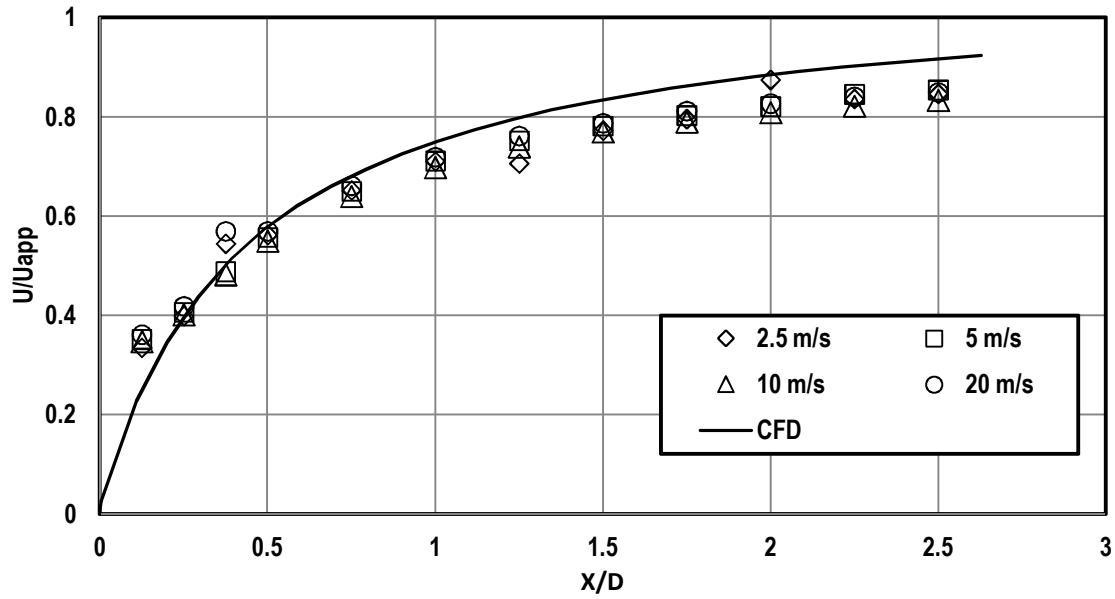

Figure 45: Dimensionless mean velocity distribution for 4″ cylinder along normalized upstream distance from the cylinder stagnation point at four different Reynolds numbers with small grid at far position (GS2).

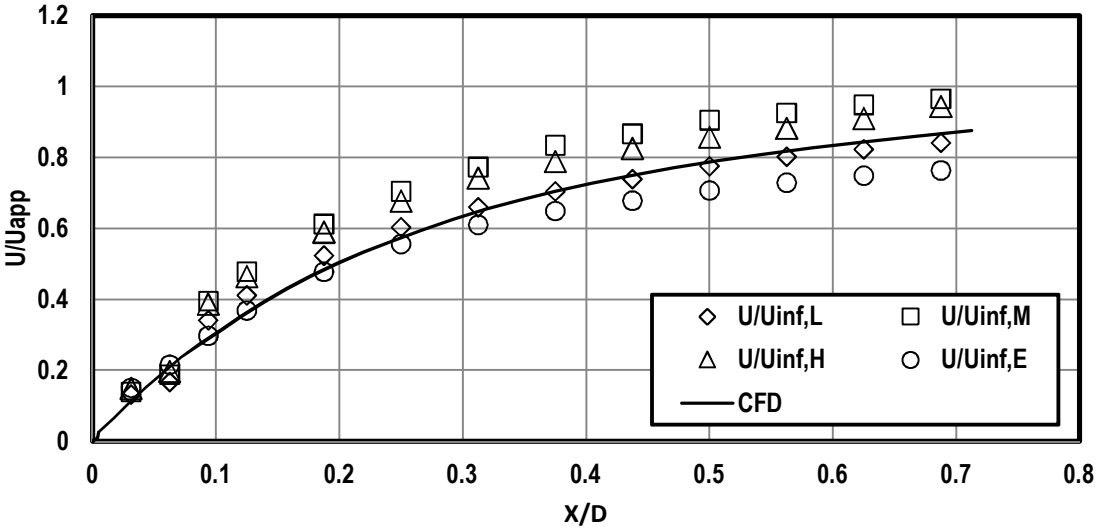

Figure 46: Dimensionless mean velocity distribution for 16″ cylinder along normalized upstream distance from the cylinder stagnation point at four different Reynolds numbers with small grid at far position (GS2).

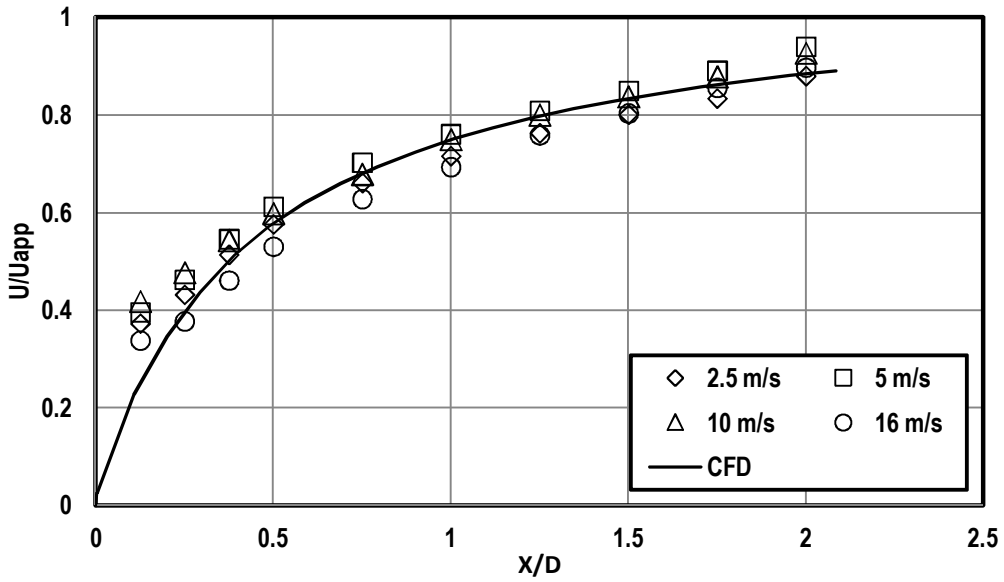

Figure 47: Dimensionless mean velocity distribution for 4″ cylinder along normalized upstream distance from the cylinder stagnation point at four different Reynolds numbers with high turbulence generator (HT1).

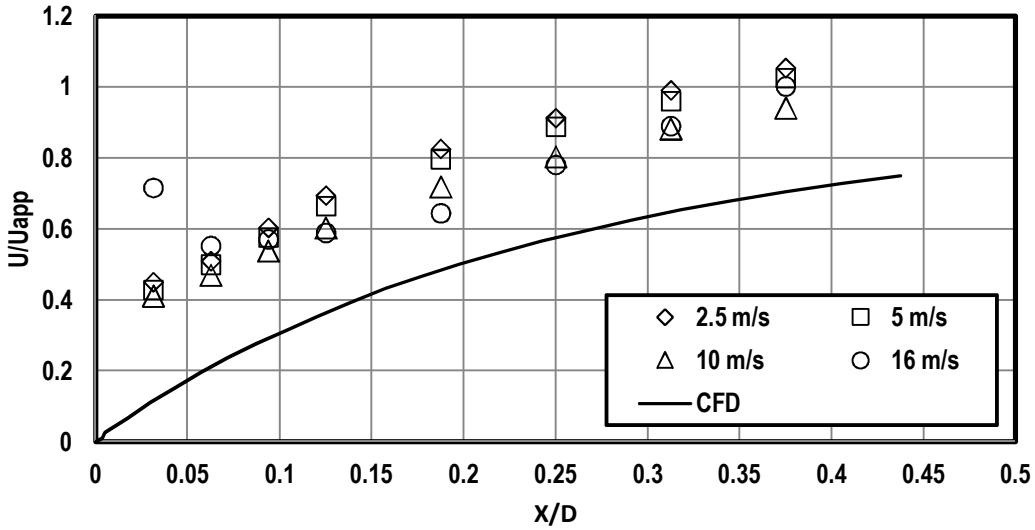

Figure 48: Dimensionless mean velocity distribution for 16″ cylinder along normalized upstream distance from the cylinder stagnation point at four different Reynolds numbers with high turbulence generator (HT1).

5.6 Turbulence Characteristics

The characteristics of turbulence parameters in the approaching flow were also determined from single wire measurements. Previously, it is evident from the experiments that FST increases the heat transfer augmentation near the stagnation region by enhancing the turbulent mixing. Turbulence intensity (Tu%) can be calculated based on the ratio of streamwise one dimensional velocity fluctuation to the mean velocity at any point using the following equation:

$$Tu = \frac{\sqrt{\overline{u'^2}}}{U}$$

The energy length scale represents the average size of the energy containing eddies in the flow suggested by Ames et al.(Ames, F.E., and Moffat, R.J. 1990).

$$Lu = 1.5\ \frac{u'^3}{\varepsilon}$$

To estimate the integral scale, Taylor's hypothesis is used, which is well described by Hinze (J. Hinze 1959). The averaged spectrum is used to calculate the autocorrelation in time using an inverse FFT. Then the autocorrelation in time is integrated to the first zero crossing to estimate the autocorrelation time scale. The autocorrelation time scale is then multiplied by the local convective velocity to develop an estimate for the integral scale (L_x).

5.6.1 RMS fluctuating velocity

The root-mean-square values of the streamwise component of turbulence were measured ahead of the body along the stagnation streamline. Most often it is difficult to interpret their meaning if they are plotted in terms of local turbulence intensity since the change in turbulence intensity is influenced by the changes in the mean velocity.

The streamwise fluctuating component is normalize by its upstream rms value (u'_∞) and plotted as the function upstream normalized distance (X/D). Figure 49 and Figure 50 show the variation of u'/u'_∞ ahead of the stagnation region of both cylinders with six different turbulence conditions. The value of u'/u'_∞ is expected to drop to zero at the surface. Decay of turbulence is expected as the flow moves downstream from the grids or aero-combustor. The amount of decay can be estimated without the presence of the cylinder body.

The small cylinder data show decay in the kinetic energy as the flow approached the stagnation region in most cases while showing some amplification for grid turbulence at far location and the aero-combustor with spool.

Figure 49 shows the decay of the rms fluctuation approximately 55% for the high turbulence generator and small grid at the near location. The small grid turbulence at the far location showed slight amplification of about 3% at X/D = 0.25. In other cases the decay of rms fluctuation velocity is slow and decreases slightly.

The big cylinder (16″) data also show similar trends for those six turbulent length scales but at a different level. Figure 50 shows that the 16″ cylinder attenuates the energy

by approximately 20% and 10% for aero-combustor and aero-combustor with decay spool respectively at X/D = 0.0625. The result also shows amplification for the grid at the far location (GS2).

High turbulence generator case also shows decay to 60% except for the case at higher Reynolds number. It is also similar to the small grid at near location of stagnation region and starts falling off right after crossing the point at X/D = 0.1. Plots for each case for the four Reynolds number are documented in the Appendix D.

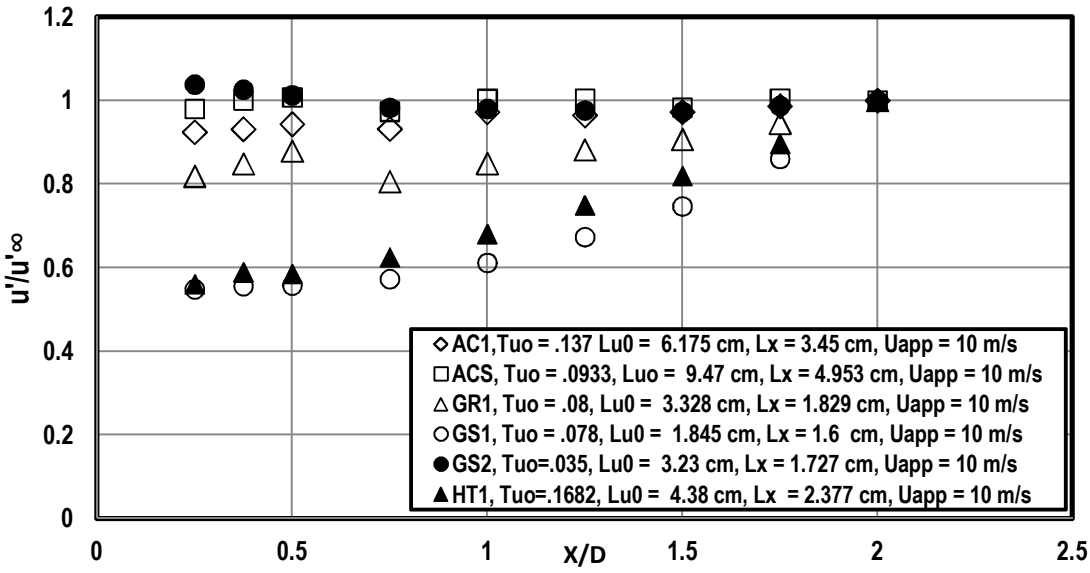

Figure 49: RMS fluctuating velocity distributions along upstream stagnation line for the small cylinder.

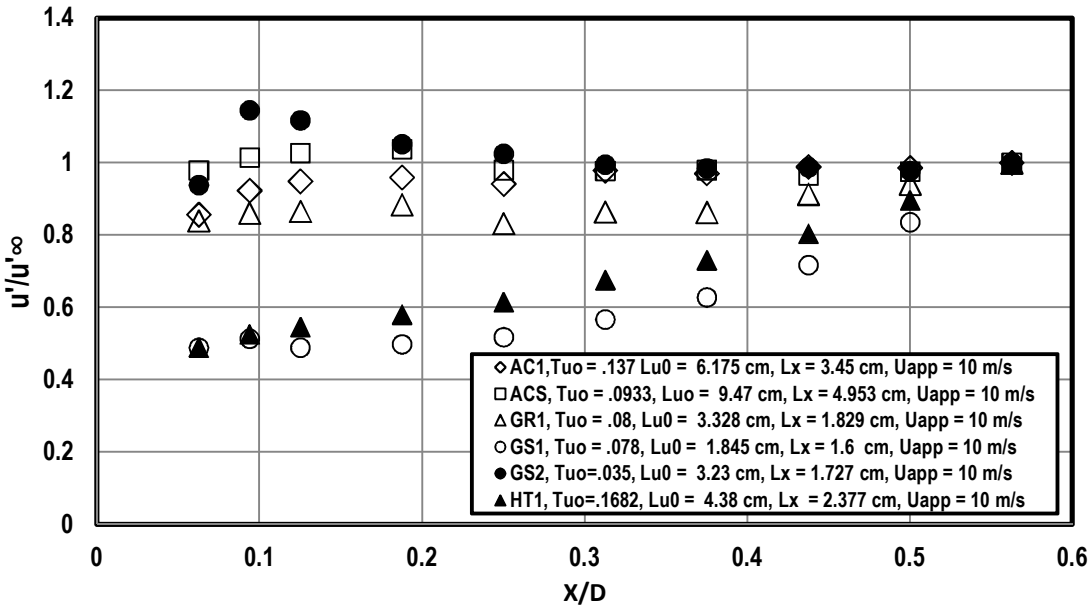

Figure 50: RMS fluctuating velocity distributions along upstream stagnation line for the big cylinder.

5.6.2 Turbulence Energy Scale (Lu)

Turbulent energy scale distributions along stagnation streamline are shown in the Figure 51 for small cylinder. The energy scales decrease significantly as flow gets closer to the stagnation region due to the attenuation of large eddies. Similar results for integral length scale are documented in the Nix at el experiment as well. A slight increase in energy scale is observed for the small scales before fall off while large scales do not show a noticeable rise before the drop. Comparatively, bigger scales start falling off very rapidly and earlier. Energy scale is calculated based on rms fluctuating velocity and dissipation rate. Since TKE decreases and dissipation rate increases near the stagnation region, so the energy scale should show something similar results. Plots for all conditions

are also shown for big cylinder in Figure 52 where the trend is analogous to small cylinder.

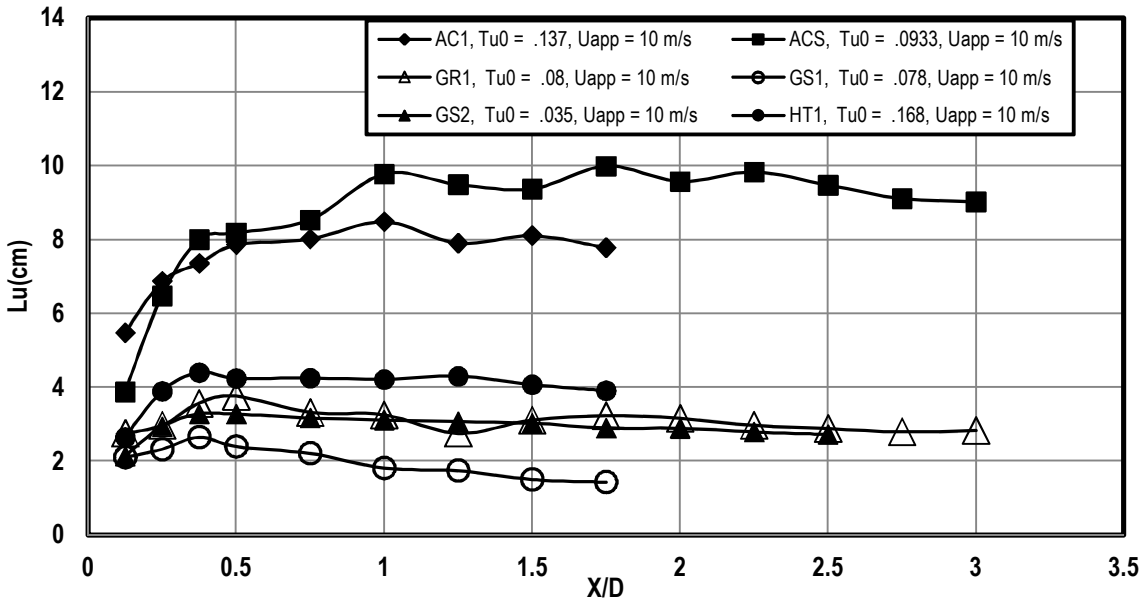

Figure 51: Energy scale distributions along the upstream stagnation line for the small cylinder.

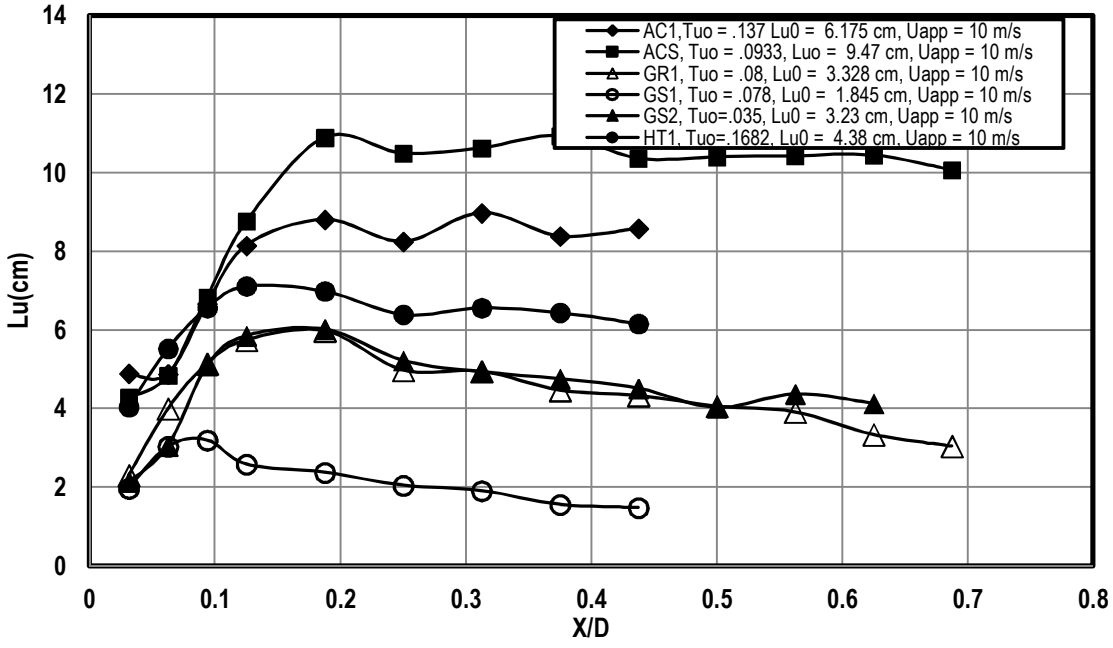

Figure 52: Energy scale distributions along the upstream stagnation line for the big cylinder.

5.6.3 Integral Length Scale (L_x)

Both cylinders have shown interesting features for the integral length scale at the six different turbulent length scales.

The integral length scale distributions along the stagnation streamline for small and big cylinder are presented in the Figure 53 and Figure 54. The plots suggest that integral length scale decreases as it goes closer to the stagnation region of the cylinders. Initially, they fluctuate in a consistent manner and start to fall off after passing certain distance.

Integral length scale decreases as the flow approaches to stagnation region for the aero-combustor case. It does not show any significant change till X/D = 0.5 from the leading edge. It falls gradually after crossing that distance (X/D = 0.5). The plot also implies that the fall off of the integral length scales dominated by the energy length scale. As the value of energy length scale increases, it also starts falling off earlier compared to those small scales.

Big cylinder shows the similar trend as small cylinder for the integral length scale distribution upstream of the stagnation region. The integral scales are decreased whenever they are closer to the stagnation region except for the case of big grid generated turbulence condition in Figure 53. Initially, it shows slow increase in the integral length scale and eventually starts falling off after crossing the distance at X/D = 0.12.

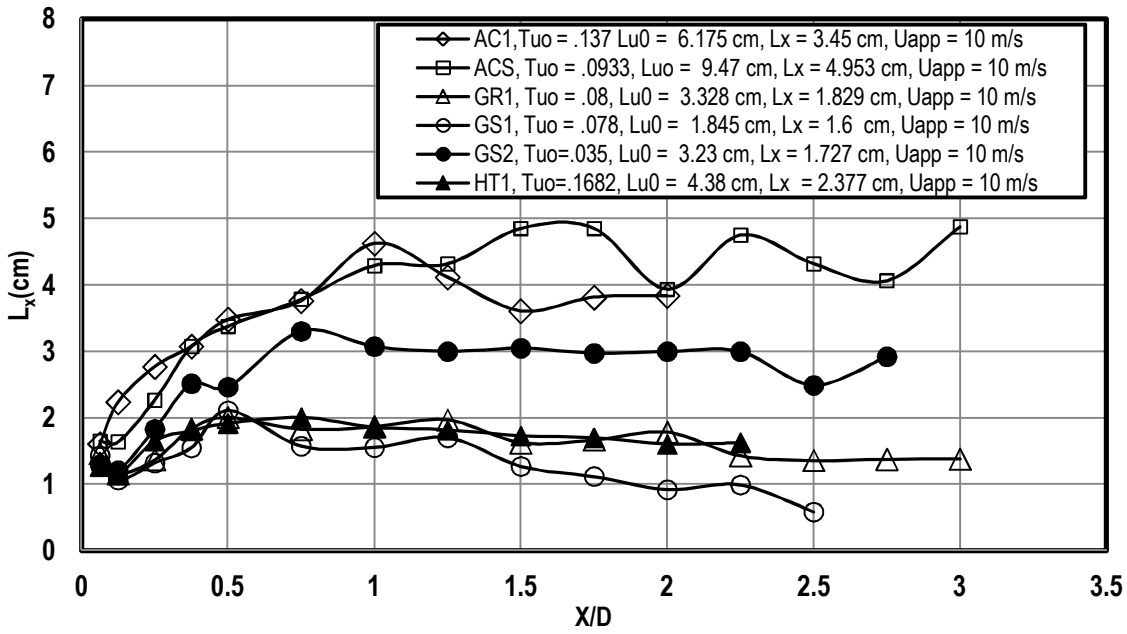

Figure 53: Integral Length Scale distributions along stagnation streamline for small cylinder.

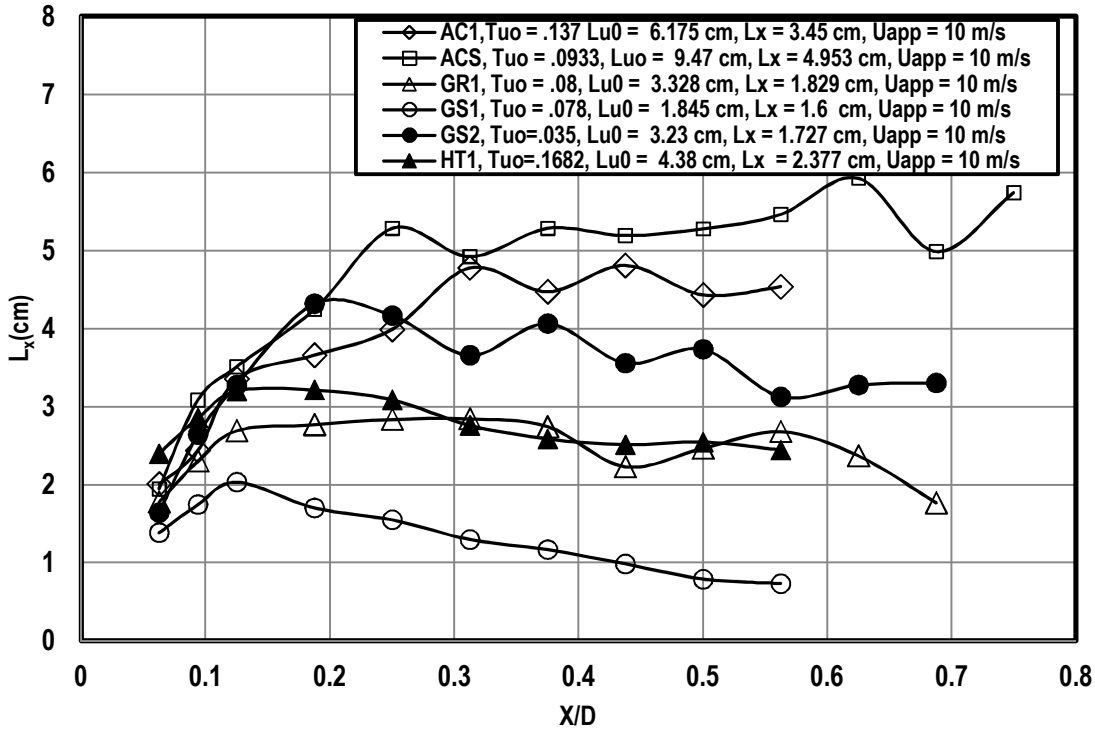

Figure 54: Integral Length Scale distributions along stagnation streamline for big cylinder.

5.6.4 Spectrum Analysis

Spectra measurements were taken at upstream of the stagnation region at four different Reynolds numbers. Spectra are plotted at X = 1″, 2″ and 4″ upstream from the stagnation region as a function of wave number to get a comparative view. The wave number and spectral energy relationship were used to fit the inertial subrange to determine the dissipation rate where the constants are chosen from Ames and Moffat (Ames, F.E., and Moffat, R.J. 1990) experiment.

$$E_1(k_1) = 1.62\left(\frac{18}{55}\right)\varepsilon^{2/3}\,{k_1}^{-5/3}$$

$$k_1 = \frac{2\pi f}{U_\infty}$$

There are three regions that can be identified from the spectral plot. The relatively flat portion at the lower wave numbers is called the energy-containing range. The spectrum then falls off at approximately -5/3 slope in which is phrased as the inertial subrange. A small tail region where the spectra fall off from the -5/3 slope is defined as the dissipation range. In general, turbulent energy is generated by velocity gradients in the flow. Initially, turbulence is neither homogeneous nor isotropic and it requires some time for the turbulence to reach these conditions. As turbulence develops, large eddies result from the velocity gradients in the flow. These larger eddies break down into smaller and smaller eddies through inertial interactions; thus, energy is transferred from larger eddies to these smaller eddies and forms an energy cascade. This process is represented by the inertial subrange. In inertial subrange, there is no addition or

dissipation of energy which means conservation of energy is maintained. As the eddy sizes turn into smaller and smaller eddies, the viscous effect becomes more and more dominant and turbulent energy is dissipated.

All the turbulence conditions show the clear attenuation at lower wave numbers as the flow approaches near the stagnation region. Figures are only shown for the aero-combustor with spool condition. From the spectrum analysis, it is quite obvious that the spectra showed attenuation for a range of low wave numbers which represents the large energy containing eddies due to the blocking effect caused by the presence of cylinder body in the flow. However, amplification is observed in the inertial subrange region for the big cylinder in Figure 56. The end portion of the spectrum called dissipation region where decay of energy is dominated by viscous effect which causes the spectra to fall off at a rate of greater than -5/3. The spectra show a longer tail due to the resolution of data acquisition board.

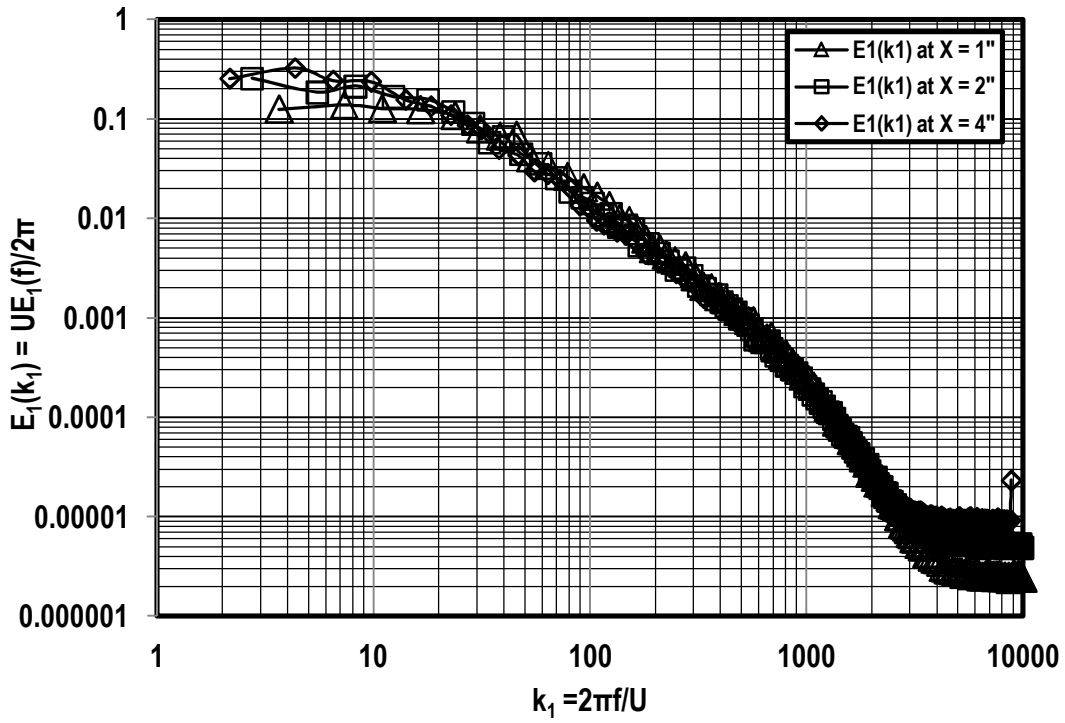

Figure 55: Spectra for aero-combustor with spool for the small cylinder at 10 m/s.

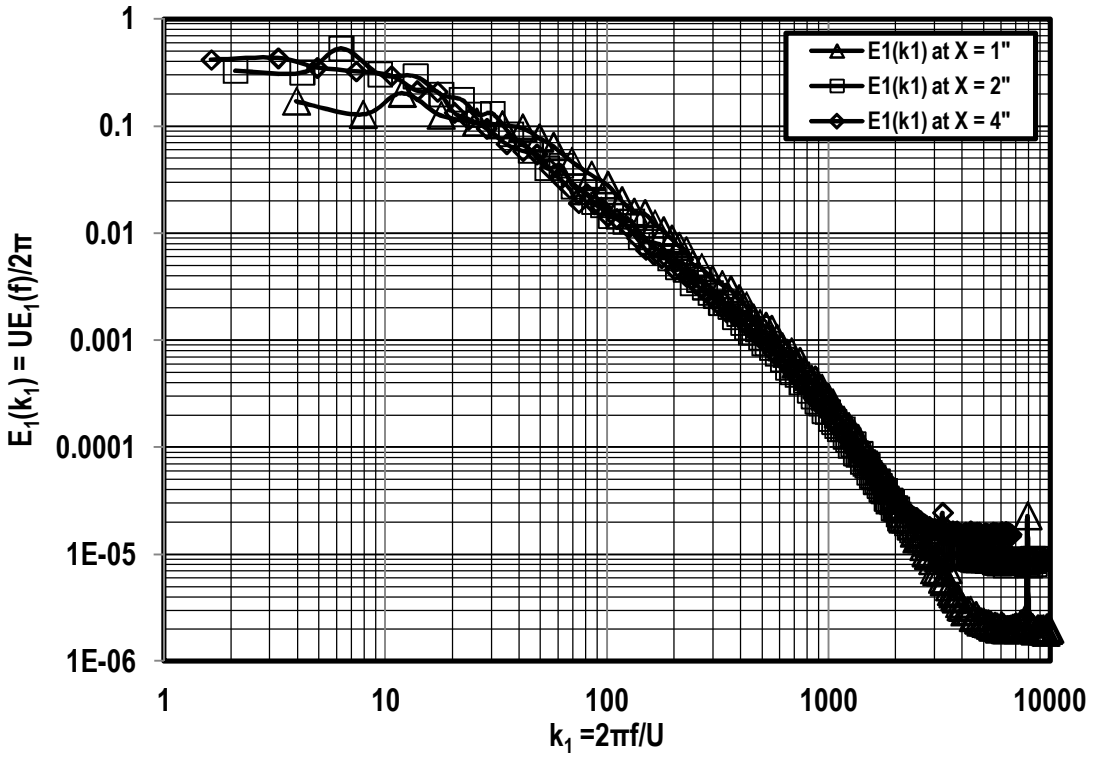

Figure 56: Spectra for aero-combustor with spool for the big cylinder at 10 m/s.

5.6.5 Dissipation Rate (ε)

Dissipation rate is approximated by matching -5/3 slope to the inertial subrange of the spectra and plotted against the upstream stagnation streamline of the cylinder in the Figure 57 and Figure 58. Dissipation rate is the measure of the rate of change in the turbulent kinetic energy with respect to time. It is normalized by using the value of dissipation rate at x = y = z = 0 without the cylinder in position. Both the cylinders showed interesting features in response to the dissipation rate. Dissipation rate decays faster for the small grid at near location and the high turbulence generator. All the conditions showed slight increase near the stagnation region except high turbulence generator condition which is in good agreement with Britter et al(R. E. Britter, J. C. R. Hunt AND J. C. Mumforf 1979). According to Britter et al, the dissipation of energy is expected to be higher in the straining flow near the cylinder than in the approach flow. But in this experiment, it is observed that the dissipation rate falls at the closest point to the stagnation region which is 0.25" away from the wall. The rms fluctuation velocity measurement, as discussed earlier, could be influenced by the unsteadiness due to high FST and the vibration in the probe holder. That may influence the dissipate rate calculation by contributing uncertainties, since dissipation rate is related to the cubic function of streamwise rms fluctuating velocity.

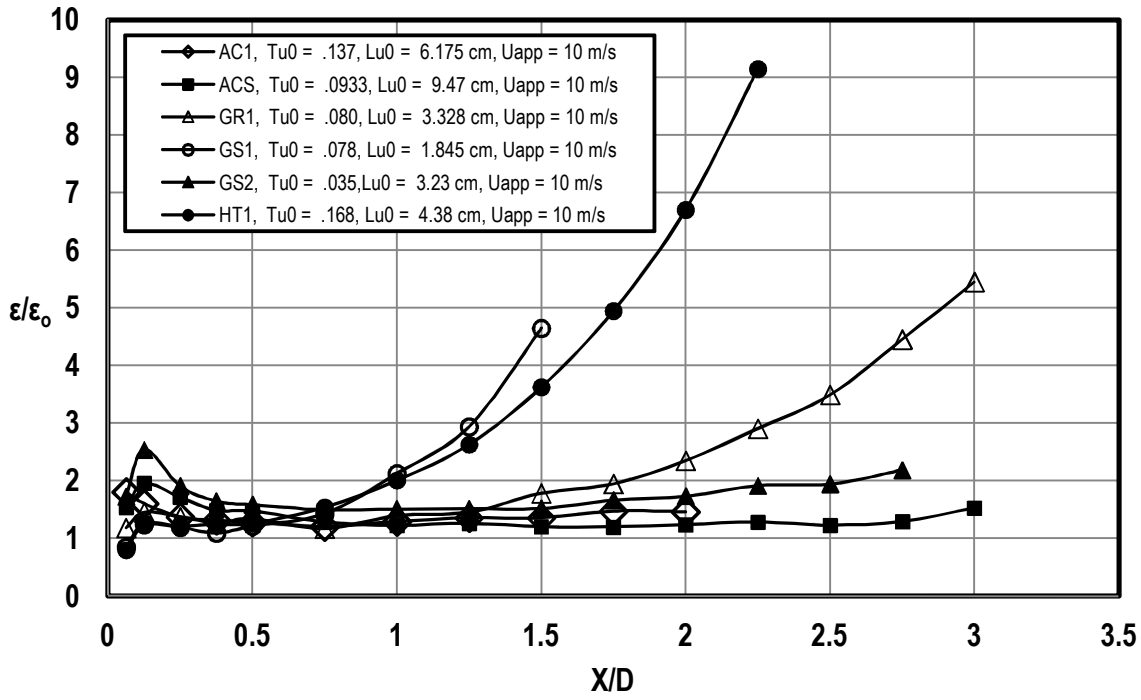

Figure 57: Dissipation rate plots in the upstream of the small cylinder.

Dissipation rate also shows the similar trend for the big cylinder as the small cylinder. But in the case of aero combustor with spool, it shows remarkable increase in the dissipation rate as the flow approaches near the stagnation region. It also showed the influence of body size and energy length scale effect on the turbulence distortion.

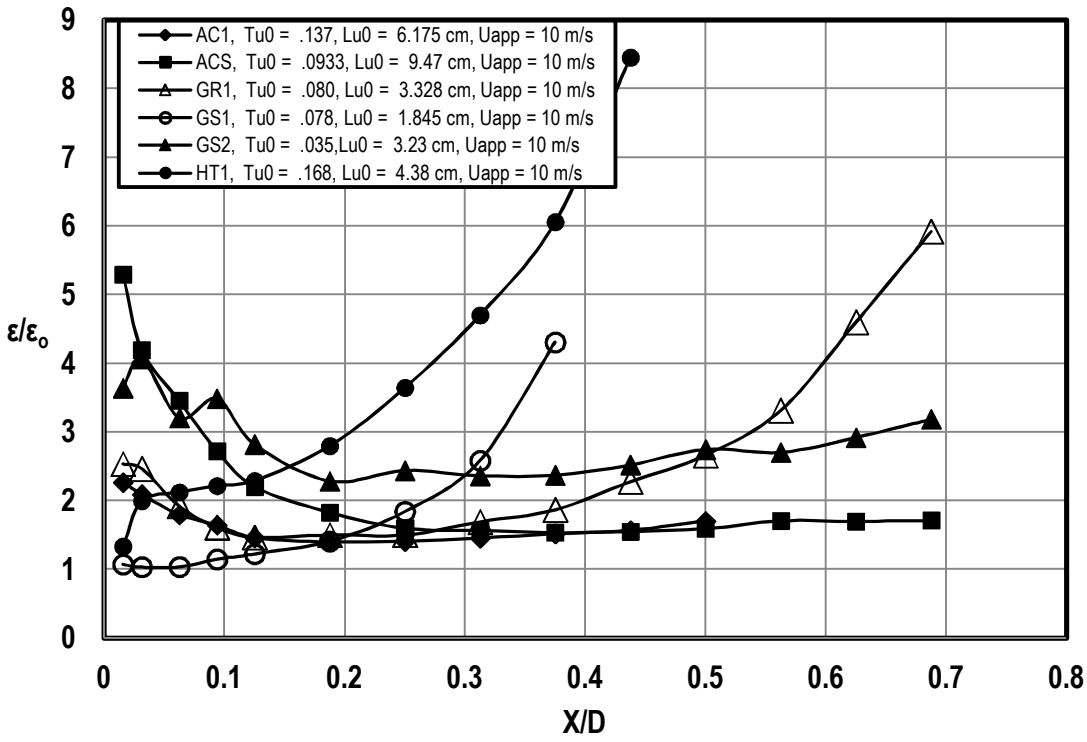

Figure 58: Dissipation rate plots in the upstream of the big cylinder.

5.6.6 Effective Length (L_e)

Dissipation rate is plotted against the effective length to compare the dissipation characteristics with and without the presence of the cylinder in position. The parameter effective length is calculated based on the flight time that required for approach flow to reach near the stagnation region. Flight time is calculated from the CFD code.

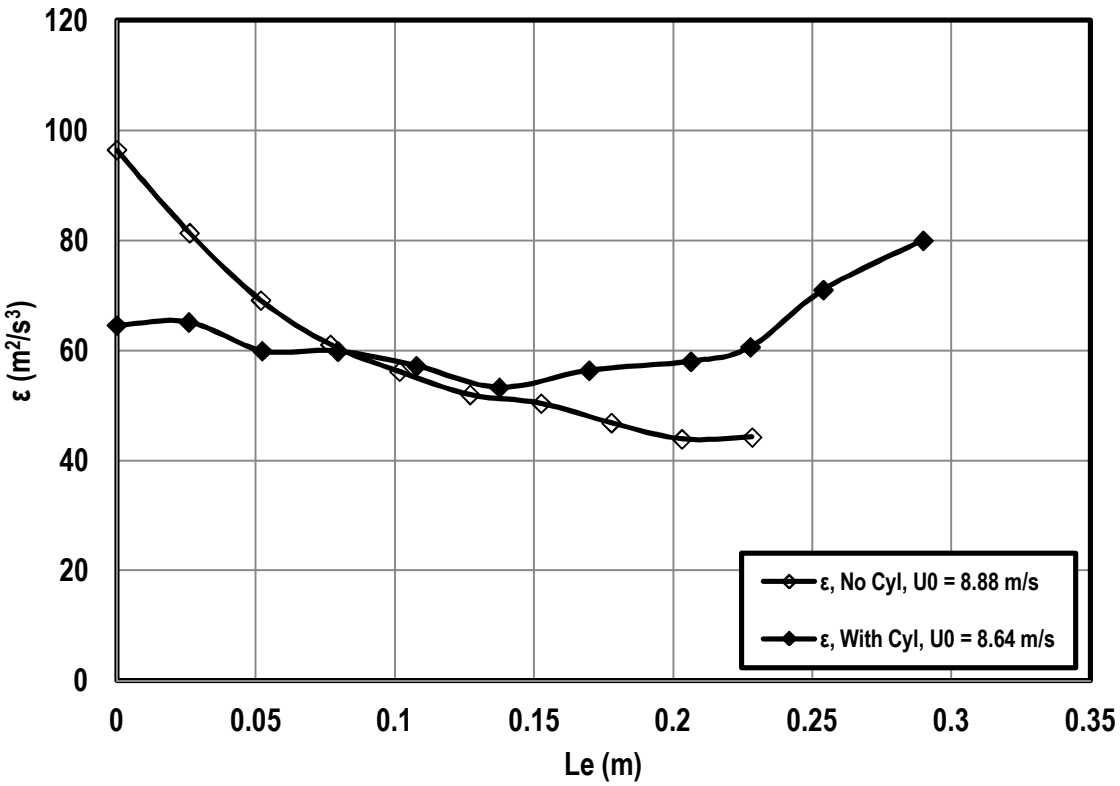

Figure 59: Plot of Dissipation rate against Effective length with and without the small cylinder (4") in position for the aero combustor (AC1) at Re_D = 62,500.

Dissipation rate against effective length with and without the small cylinder for aero-combustor is plotted in Figure 59. It is very clear that the dissipation rate decreases initially and then increases as it approaches near the stagnation region which is in good agreement with Britter et al. (R. E. Britter, J. C. R. Hunt AND J. C. Mumford 1979). And it is also expected that the flow with the presence of cylinder takes more time to dissipate its energy compare to no cylinder in position.

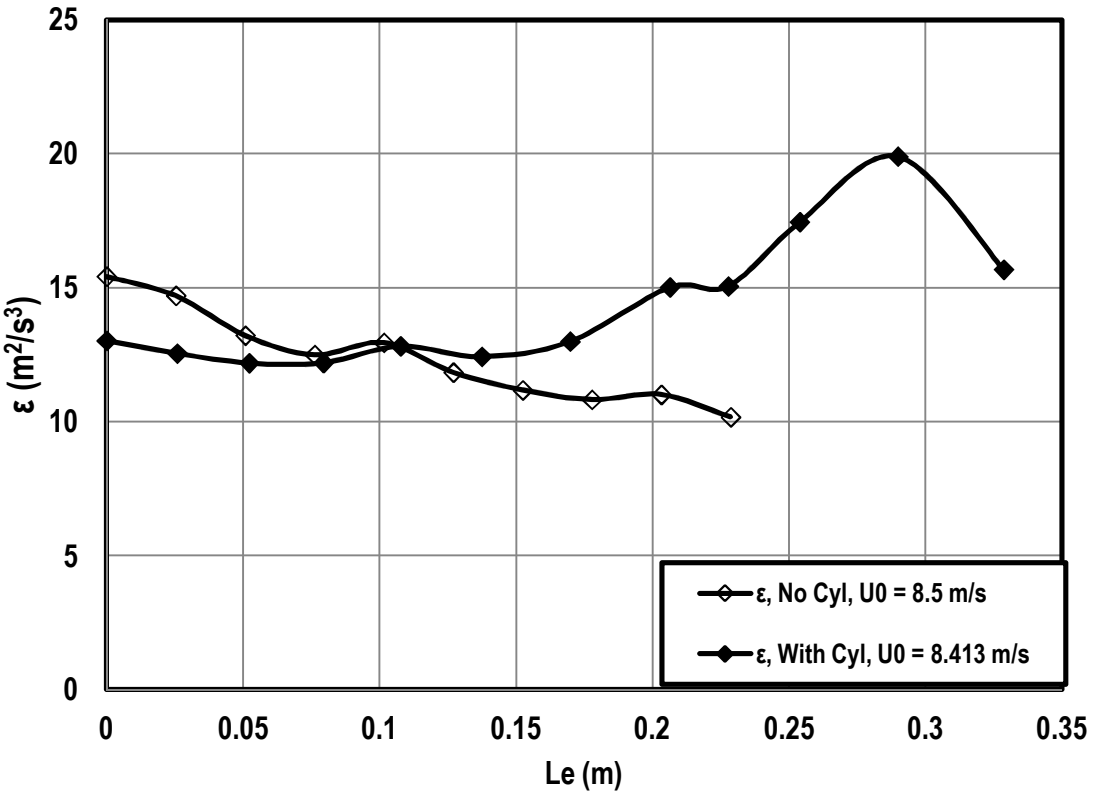

Figure 60: Plot of Dissipation rate against Effective length with and without the small cylinder (4") in position for the aero combustor with spool (ACS) at Re_D = 62,500.

Figure 60 also shows dissipation rate against effective length with and without the 4″ cylinder for ACS conditions. It is quite flat initially and then increases as it approaches near the stagnation region. Next, it starts fall off in the flow near the wall. The near wall fall off in dissipation is not fully understood.

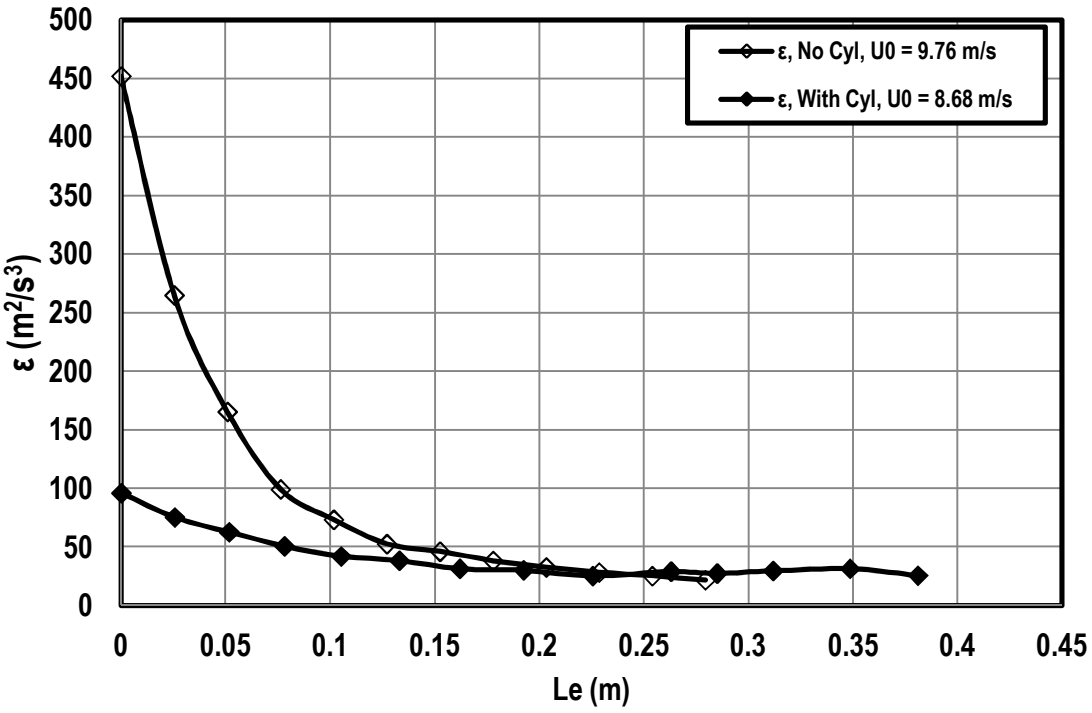

Figure 61: Plot of Dissipation rate against Effective length with and without the small cylinder (4") in position for the big grid (GR1) at Re_D = 62,500.

Figure 61 also shows dissipation rate plot for GR1 against effective length with and without the 4″ cylinder. It decreases very slowly for the most of its flight as it approaches near the stagnation region and starts to increase slightly as the flow moves closer to the stagnation region. The cylinder in position changes the decay characteristics of the turbulence from its no cylinder condition.

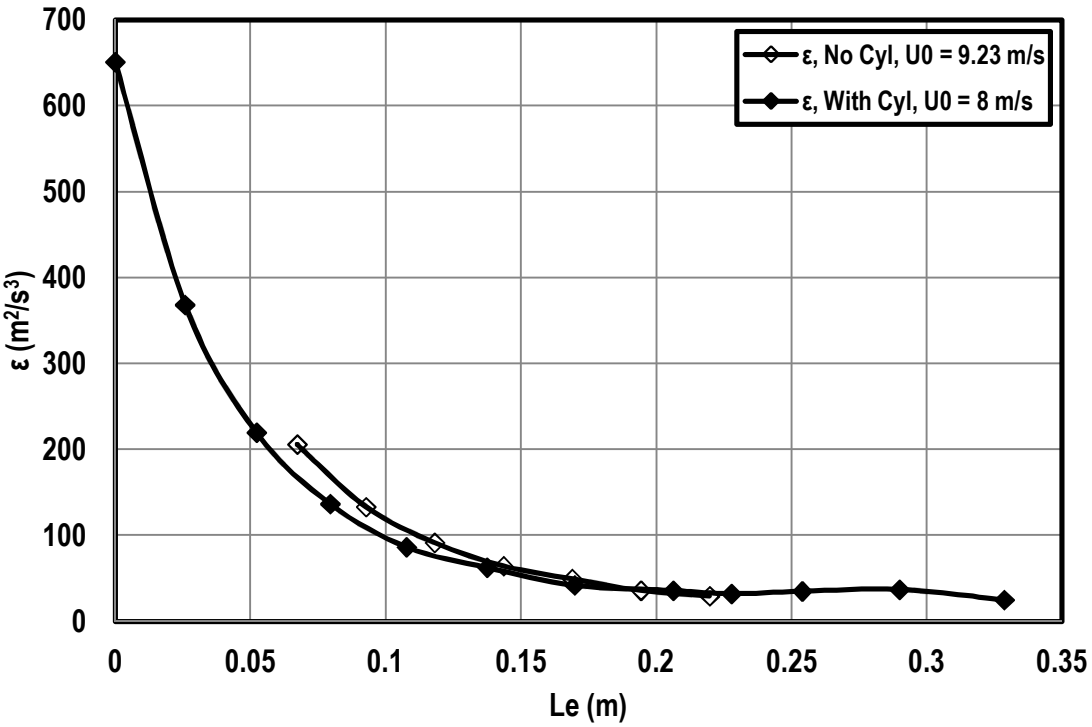

Figure 62: Plot of Dissipation rate against Effective length with and without the small cylinder (4") in position for the small grid at near location (GS1) at Re_D = 62,500.

Figure 62 also shows dissipation rate plot for GS1 against effective length with and without the 4″ cylinder. It decreases monotonically with showing a flat tail at the end with a minor drop as the closer to the stagnation region.

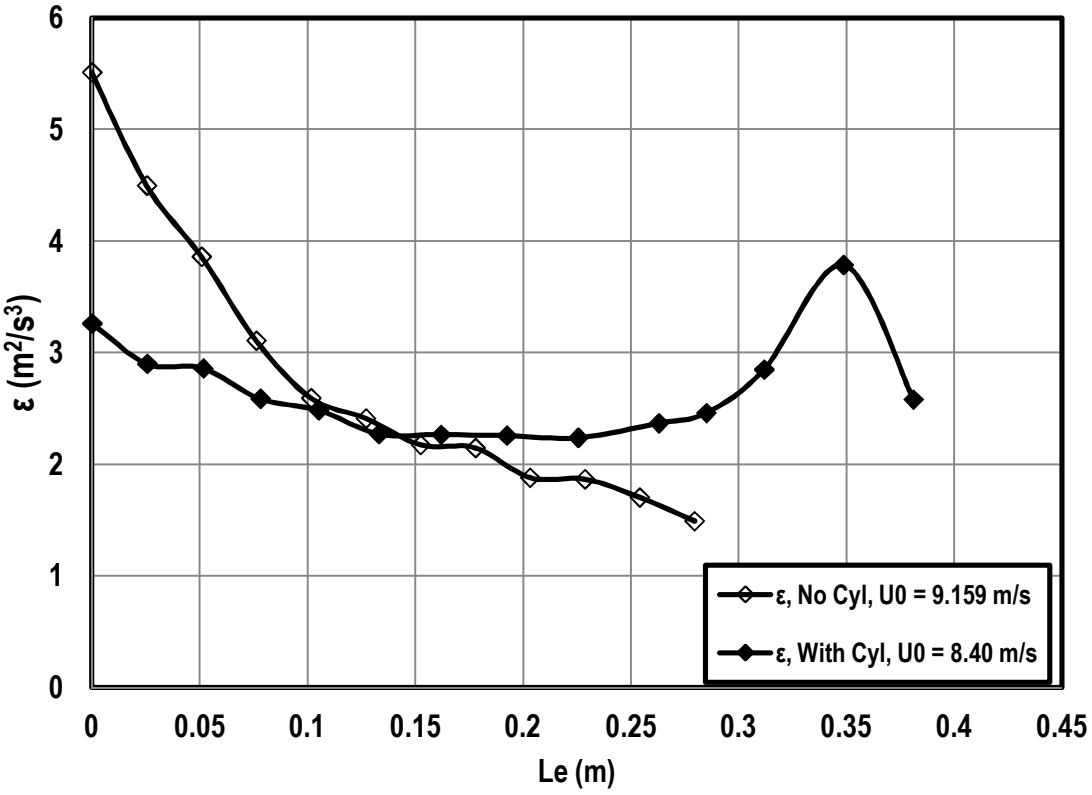

Figure 63: Plot of Dissipation rate against Effective length with and without the small cylinder (4") in position for the small grid at far location (GS2) at Re_D = 62,500.

Figure 63 shows dissipation rate plot for GS2 against effective length with and without the 4″ cylinder. Initially, it decays consistently then again starts increasing as the flow moves toward the stagnation region.

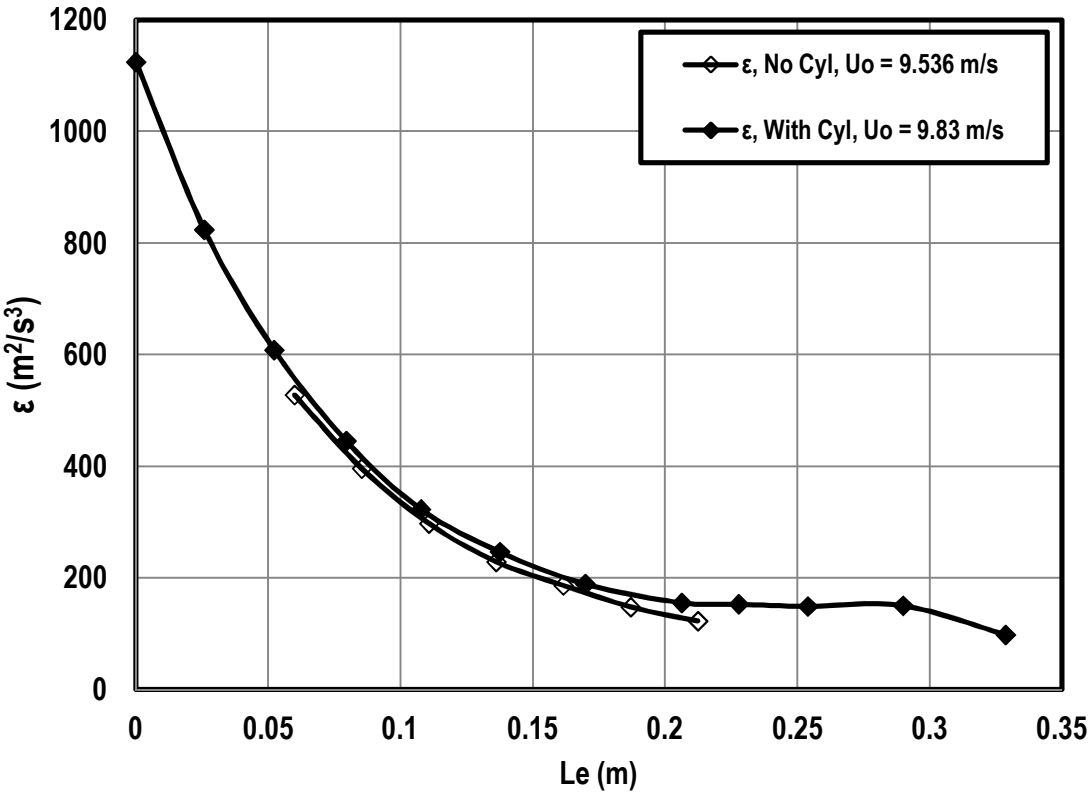

Figure 64: Plot of Dissipation rate against Effective length with and without the small cylinder (4") in position for the high turbulence generator (HT1) at Re_D = 62,500.

Figure 64 shows dissipation rate plot for HT1 against effective length with and without the 4″ cylinder. It shows that the flow dissipates rapidly as the flow moves toward the stagnation region. Both the curves fall on each other nicely showing the same trend and dissipation takes longer time compare to no cylinder in position.

The dissipation trend is also shown for big cylinder in the Figure 65 through Figure 70. The aero-combustor condition in Figure 65 shows a decrease initially and then increases as it approaches to the stagnation region. But the aero-combustor with decay

spool does not show any remarkable change at the beginning and starts increasing as it moves toward the stagnation region.

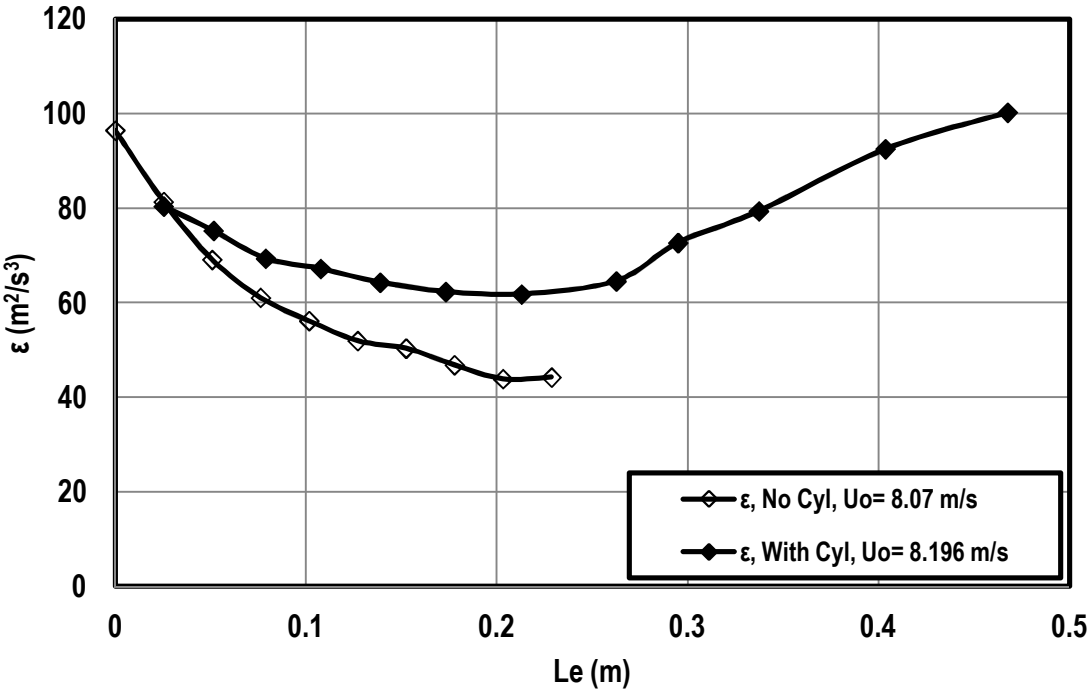

Figure 65: Plot of Dissipation rate against Effective length with and without the big cylinder (16") in position for the aero combustor (AC1) at Re_D = 250,000.

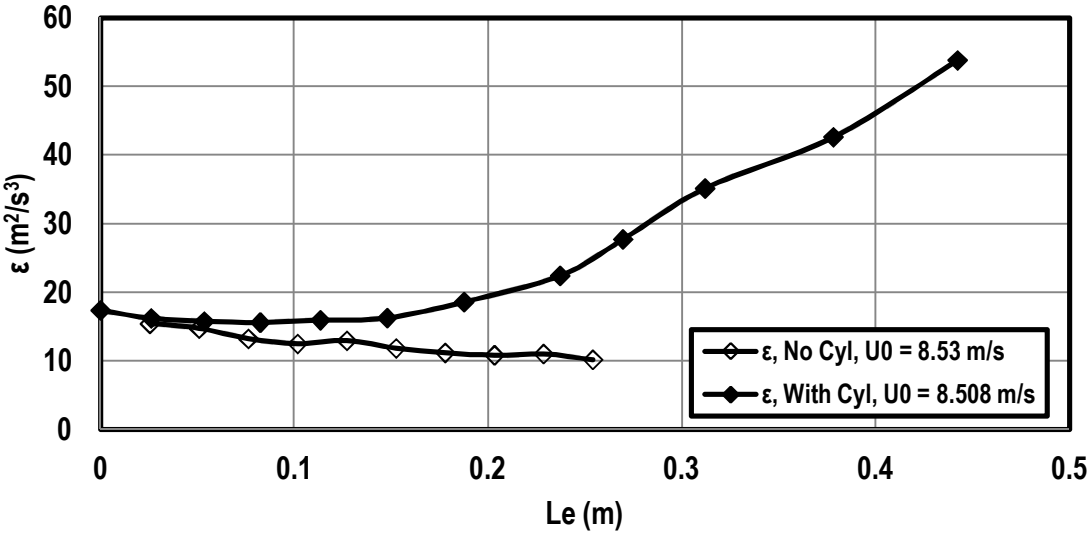

Figure 66: Plot of Dissipation rate against Effective length with and without the big cylinder (16") in position for the aero combustor with spool (ACS) at Re_D = 250,000.

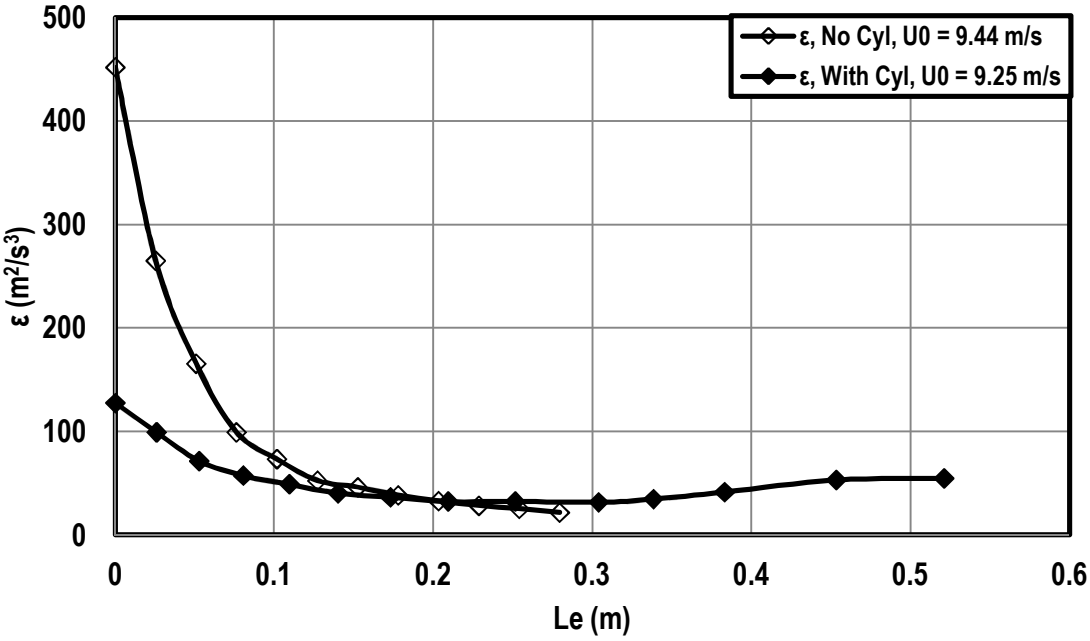

Figure 67: Plot of Dissipation rate against Effective length with and without the big cylinder (16") in position for the big grid (GR1) at Re_D = 250,000.

Dissipation rate starts decreasing very sharply for the case of big grid generated turbulence and it keeps consistently decreasing for the rest of the distance in the Figure 67. Both curves fall on each other very well showing the same trend.

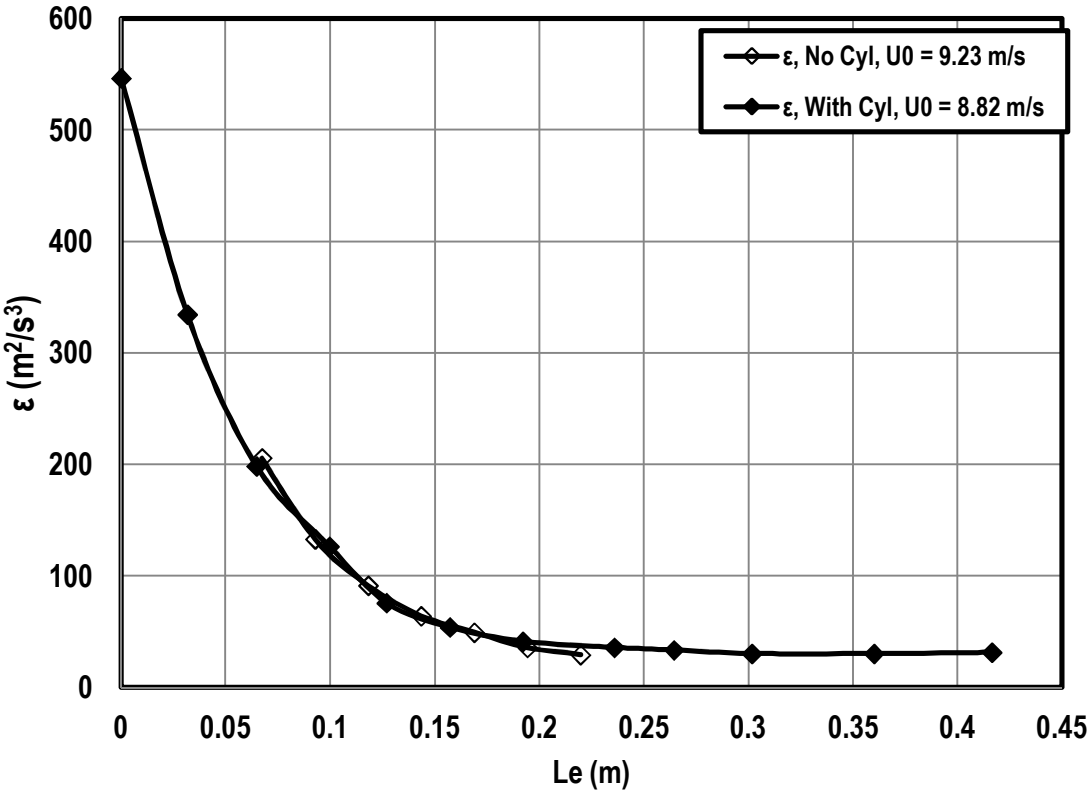

Figure 68: Plot of Dissipation rate against Effective length with and without the big cylinder (16") in position for the small grid at near location (GS1) at Re_D = 250,000.

Figure 68 also shows dissipation rate plot for GS1 against effective length with and without the 16″ cylinder. The dissipation rate decreases very slowly with a very minor drop as the flow moves closer to the stagnation region and crosses a longer

effective distance to dissipate the energy from the same stand point as no cylinder condition.

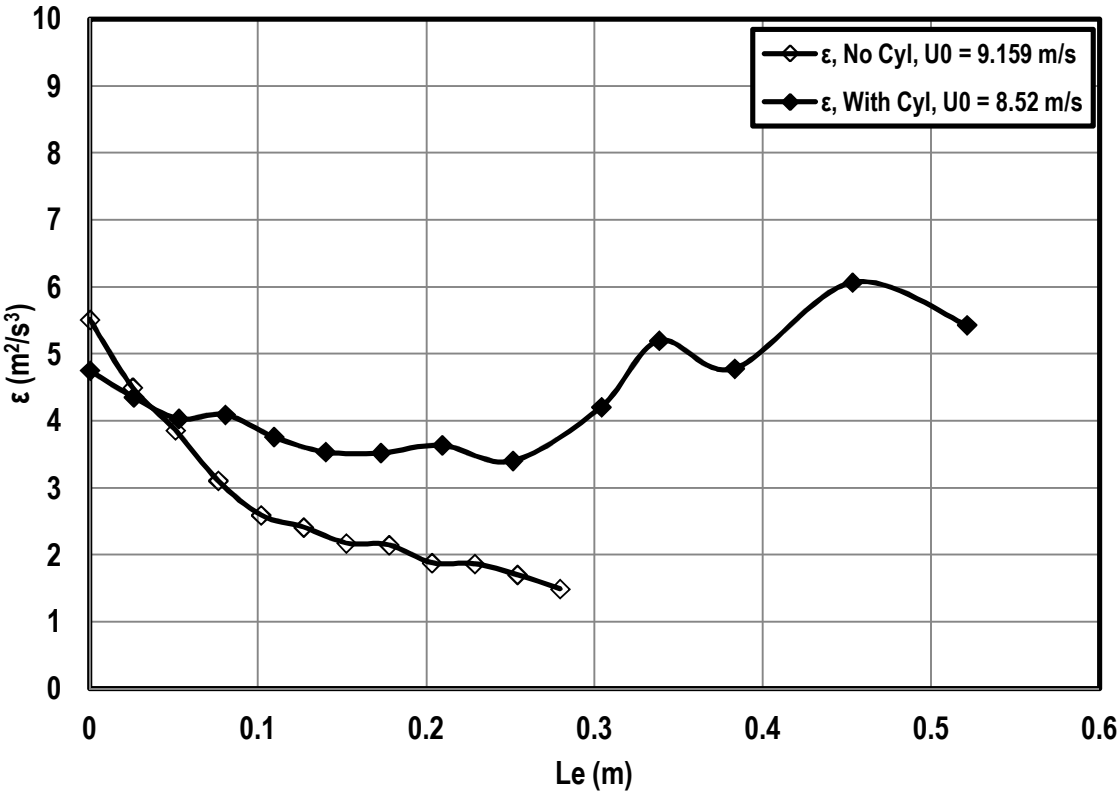

Figure 69: Plot of Dissipation rate against Effective length with and without the big cylinder (16") in position for the small grid at far location (GS2) at Re_D = 250,000.

Dissipation rate plot for GS2 against effective length with and without the 16″ cylinder is shown in Figure 69. It decreases with a sharp fall, initially, and then starts increasing as the flow moves toward the stagnation region showing a peak.

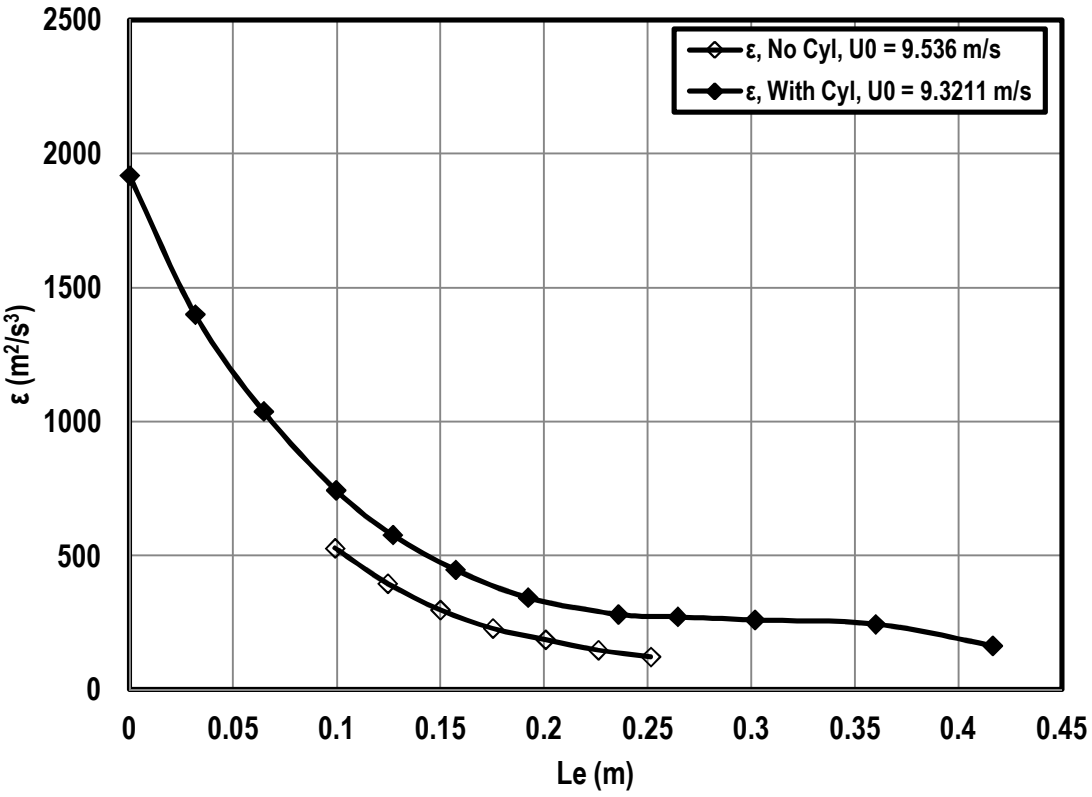

Figure 70: Plot of Dissipation rate against Effective length with and without the big cylinder (16") in position for the high turbulence generator (HT1) at Re_D = 250,000.

Figure 70 shows dissipation rate plot for HT1 against effective length with and without the 16″ cylinder in position. It shows that the flow dissipates rapidly as the flow moves toward the stagnation region. Both the curves fall and show the similar trend and dissipation for the cylinder in position takes a longer time compared to no cylinder in position.

CHAPTER V

CONCLUSIONS

The purpose of this study was to systematically document the detailed history of upstream flow field in the presence of a cylindrical leading edge, which is very important in understanding and predicting the heat transfer at the stagnation region of a turbine vane. This research was intended to acquire hotwire measurements along the stagnation streamline with and without the presence of the large and smaller cylinders. These measurements included the mean velocity (U), the rms fluctuating velocity (u′), the energy length scale (Lu), the integral scale (L_x), the dissipation rate (ε), and the one dimensional turbulent spectrum for different turbulence conditions. Turbulence was generated using two bi-planer grids and two aero combustors for two different test bodies. The two cylindrical leading edges of different diameter (0.1016 m and 0.4064 m) produced Reynolds numbers ranging from 15,625 to 500,000 based on diameter and approach velocity.

Test bodies were fabricated with foam boards that were stacked in between plywood. Both the cylinders were covered with a fiberglass epoxy board circumferentially to make a smooth surface downstream of the stagnation region. A traversing mechanism was developed that allowed the probe to move along stagnation streamline capable of reaching 24″ upstream. The approach velocity was estimated using

an upstream total pressure probe and a downstream static pressure tap based on CFD calculation.

The small cylinder was used in the experiment for six different scales of turbulence conditions at four different Reynolds numbers based on approach velocity and leading edge diameter. The mean velocity distributions and the streamwise rms fluctuating component distribution along the upstream stagnation streamline were obtained using hot wire anemometry. They were also compared with CFD code where they showed remarkable variation close to the stagnation region. The variations in the velocity distributions can be due to spanwise variations in the streamwise velocity, effective velocity error resulting from the high levels of the streamwise and lateral components of free stream turbulence and vibration in the probe support. These uncertainties are analyzed using statistical analysis and by generating random data points that helped in estimating the unusual errors. For the case of streamwise rms fluctuating component, they showed mostly attenuation whereas grid at far location showed slight amplification. For the case of high turbulence generator and small grid at near location, it showed large decay with continuous attenuation. Different quantities like integral length scale (Lx), energy length scale (Lu), and dissipation rate (ε) related to turbulent spectra were extracted from spectrum analysis. Results suggested that as the flow is approaching the cylinder stagnation region, the integral length scale decreases appreciably with the same trend for the energy length scale as well. This means that average size of eddies decreases as the flow goes closer to the body. Again, dissipation rate showed strong initial decay for high turbulence generator (Tu = 16%), small grid at near location (Tu = 7.8%) case and big grid (Tu = 8%) conditions. But in every case, they showed a slight

increase near the stagnation region. The strong streamwise decay was influenced with the larger transport time of the turbulence along the streamline with the decrease in velocity. Since the small grid at near location and big grid were comparatively closer to the test body, they showed that noticeable decay initially. The effective decay time that is required for a flow in the presence of a cylinder was modeled using the dissipation rate in terms of effective length based on CFD code. It suggested that the presence of a body in the flow slowed down the flow. It results in a longer time for decay of turbulent energy and was also responsible for intensifying the energy dissipation rate for two higher energy scales (AC1 and ACS) in comparison with the no cylinder in position. The spectra were captured at different upstream locations from the cylinder to estimate the dissipation rate that was calculated approximately by matching the -5/3 slope with the inertial subrange of the energy cascade. The spectrum plot at different positions also suggested that turbulent energy is blocked as the flow goes closer to the stagnation region in the low wave number range.

The big cylinder was also tested for similar conditions to the small cylinder and showed analogous characteristics of turbulent parameters. The same inlet turbulence conditions were applied at four Reynolds numbers to observe the behavior of turbulence distortion. The big cylinder showed higher increase in the turbulence intensities in each case, which resulted from the large body presence in the flow. The big cylinder also showed higher uncertainty near the stagnation region due to higher blockage to the flow and the high frequency vibrations of the hot-wire probe support.

Though the hot-wire measurements were limited to upstream locations, the results agree well with other previous experiments. There are a good number of correlation models already developed that have been using to predict the heat transfer by turbine designers, within limitations. Those models require detailed knowledge of the local turbulence intensity and integral length scale distribution in the flow field. These values may not be known exactly for actual engine conditions, although computational fluid dynamics predictions may be able to establish a reasonable estimate of these values based on the inlet turbulence conditions, making the model moderately applicable to engine development. The results of from this experiment will offer insight in understanding the scales of turbulence that are considered as most critical in affecting surface heat transfer of a vane.

APPENDICES

APPENDIX A

Table 2: Table showing all the turbulence generators used with their corresponding turbulence intensities, length scale, and others at the stagnation point at no cylinder conditions.

Turbulence Conditions	**U_{ave} (m/s)**	**Tu**	**L_x (cm)**	**Lu(cm)**	**ε (m^2/s^3)**
Aero-combustor (AC1)	4.433	0.153	4.267	7.158	6.494
	8.907	0.137	3.454	6.175	44.251
	17.830	0.138	3.810	7.075	313.691
Aero-combustor with decay spool (ACS)	4.572	0.100	4.788	8.832	1.637
	9.247	0.093	4.953	9.477	10.171
	18.469	0.092	4.826	9.810	75.968
High Turbulence Generator (HT1)	4.553	0.169	2.134	3.938	17.279
	9.110	0.168	2.377	4.390	122.970
	16.558	0.169	2.443	4.707	696.252
Big Grid (GR1)	5.095	0.083	1.808	3.217	3.512
	9.689	0.081	1.829	3.328	21.540
	18.638	0.081	1.942	3.194	160.752
Small Grid at Near Location (GS1)	4.484	0.081	1.514	1.785	3.998
	9.124	0.078	1.605	1.846	29.409
	17.868	0.079	1.118	1.969	215.962
Small Grid at Far Location (GS2)	4.695	0.038	2.383	3.808	0.232
	9.081	0.035	1.727	3.231	1.493
	17.612	0.035	2.134	2.854	12.127

APPENDIX B

Table 3: Table showing all stations that used for capturing data at different turbulence generator conditions

X Locations (in)	AC1	ACS	GS1	GR1	GR2	HT1
0.25	√	√	√	√	√	√
0.5	√	√	√	√	√	√
1	√	√	√	√	√	√
1.5	√	√	√	√	√	√
2	√	√	√	√	√	√
3	√	√	√	√	√	√
4	√	√	√	√	√	√
5	√	√	√	√	√	√
6	√	√	√	√	√	√
7		√	√	√	√	
8		√	√	√	√	
9		√	√		√	
10		√	√		√	
11		√	√		√	
12		√	√		√	
13		√	√		√	

APPENDIX C

HOT WIRE CALIBRATION TECHNIQUE

Calibration was required for miniature single wire and x-wires before using in the experiment. A calibration wind tunnel with a heat exchanger was utilized to produce the operating range of velocities from 0.50 m/s to 35 m/s. The target was set to calibrate hot wire within ± 2 percent that gave an uncertainty of ± 4 percent in the pressure differential according to the Bernoulli's law. The pressure transmitters have an accuracy of ± 0.1 percent of the full scale. Combining these uncertainties gives a differential pressure of 3.1 Pa. The minimum velocity can be estimated to be 2.4 m/s based on Bernoulli's equation within the 2 percent uncertainty. This velocity was easily generated using a simple nozzle setup where the differential pressure was measured in between atmosphere and upstream of the contraction. Bernoulli's equation was used to calculate the inlet jet velocity from the calibration tunnel.

To get velocities lower than 2.4 m/s within the preset uncertainty, a specially designed low velocity jet nozzle with a larger area ratio was used in addition to the regular nozzle that used to measure the higher velocity range. The mathematical correlation was developed earlier based on mass flow rate in the jet experimentally from

the pressure difference in the flow entering and exiting this low-speed nozzle. The velocity at the regular nozzle exit plane can be measured based on this mass flow rate and the boundary layer growth inside the nozzle.

Voltage responses produced by the hot wire at different velocities were recorded as a function of Reynolds number based on wire diameter. Changes in density were accounted for due to atmospheric pressure variations. Hot wire voltages were also corrected for wire-to-gas temperature changes and air thermal conductivity changes based on a fundamental heat transfer analysis. A fourth order regression analysis was performed on the data prior to using the calibration. The regression analysis performed based on the difference between the measured voltage and the average voltage. The regression fit the data within ± 4 percent for the high velocity range (1.5 m/s to 35 m/s) and within ± 2 percent for the low velocity range (0.5 m/s to 4 m/s). An intended overlap was made in between high and low velocity calibration jets to construct of an entire range of data, from 0.5 m/s to 35 m/s. calibration curve is shown in the Figure 71.

Mathematical Background

Velocities were captured as a function of Reynolds number based on wire diameter to account for changes in density due to atmospheric pressure variations. Hot wire voltages were corrected for wire-to-gas temperature changes and air thermal conductivity changes based on a basic heat transfer analysis at the same time. The rest of the article gives a general mathematical background, showing that the effective velocity

sensed by the hot wire, V_{eff}, is a function of Reynolds number based on wire diameter, Re_w. In this analysis, the Prandtl number is assumed to be nearly constant for air: 0.71.

$$Q = \frac{V^2}{R_w} = h\, A_w\, (T_w - T_f)$$

$$Nu = \frac{hD_w}{k} = Cf(Re_D)$$

$$h = \frac{k}{D_w}\, Nu_D = \frac{k}{D_w}\, f(Re_D)$$

$$\frac{V^2}{R_w} = \frac{k}{D_w}\, f(Re_D)\;\; A_w\, (T_w - T_f)$$

The wire resistance, R_w, area, Aw, and diameter, D_w, all remain constant and are therefore combined into a constant value, C_1.

$$V^2 = C_1\, k\, f(Re_D)\, (T_w - T_f)$$

$$V = C_2 \sqrt{\left(k\, f(Re_D)\, \left(T_w - T_f\right)\right)}$$

$$V_{eff} = C_2 \sqrt{\left(k_o\, f(Re_D)\, (T_w - T_o)\right)}$$

Solving the equations for V and V_{eff} in terms of the square root of a function based on Reynolds number based on diameter allows the two to be equated, and an equation for the effective voltage is then found.

$$\frac{V}{\sqrt{(k\, (T_w - T_g))}} = \frac{V_{eff}}{\sqrt{(k_o\, (T_w - T_o))}}$$

$$V_{eff} = V\sqrt{\frac{k_o}{k}}\sqrt{\frac{(T_w - T_o)}{(T_w - T_g)}}$$

In practice, $V^2 = A_o + B_o U^n$ since $Re_D = \frac{\rho UD}{\mu}$

Where n= 0.45 according to King's Law

This analysis provides a compensation for the thermal conductivity of air (k), the wire-to-gas temperature difference, and density changes. Calibration of the hot wires was performed first for the high velocity range in order to set the appropriate buck/offset and gain. These values were then used for the low velocity calibration. The following procedures were followed that written by previous graduate student Lindsay Dvorak for calibration of single wire.

Procedure for Calibrating a Single Wire

1. Prepare ice bath for reference temperature.

2. Record barometer reading and temperature in log book.

3. Turn on the TSI IFA 300 constant temperature anemometry system and check the voltage fluctuation and wait for the steady state using a multimeter. (Usually it should be 4.77 volts)

4. Open valve for make-up water and start the pump to begin make-up water recirculation.

5. Place the appropriate grounding probe in the probe holder.

6. Start air flow through the calibration jet at a moderate velocity: 10 m/s for the high velocity range and 1 m/s for the low velocity range. Start up *IFA ThermalPro* software

7. Under “Diagnostics” option

a. Set a mock offset - 1.2

b. Set a mock gain - 9

c. Choose wire

d. Choose none for low-bypass filter

8. Check and record the cable resistance for few runs and get the average value

9. Stop air flow through the calibration jet.

10. Remove and put away the appropriate grounding probe.

11. Align the desired hot wire with the end of the calibration jet closely to the jet exit plane of the nozzle and multimeter is used to ensure the connection and circuit response during the experiment.

12. Start air flow through the calibration jet.

13. Measure the probe resistance for few runs and get the average

14. Calculate the operating resistance using the following equation

$$R_{op} = R_{TOT/prob} + \alpha R_{20} (T_{sensor/overheat} - T_o)$$

15. Set the operating resistance as calculated and cable resistance as measured.

16. Switch the TSI IFA 300 from standby to run.

17. Measure the bridge voltage at 0 m/s and at 35 m/s.

18. Switch the TSI IFA 300 back to standby.

19. Average the bridge voltages at 0 and 40 m/s that will give the buck or offset.

20. Subtract the average voltage from the 40 m/s bridge voltage.

21. Divide 5 by the result to get gain.

22. Reset the gain and buck/offset on the IFA300 to these new values.

23. Switch the TSI IFA300 back to run.

24. Initiate appropriate hot wire calibration routine in QuickBASIC.

25. Calibrate the hot wire over the range of velocities.

26. Use the QuickBasic program (ianalyze.bas) to perform a fourth order regression analysis on the voltages (Vactual – Vaverage) and wire Reynolds numbers.

27. Switch the TSI IFA300 back to standby and remove the hotwire.

28. Replace the high velocity calibration jet with the low velocity calibration jet.

29. Place the hot wire in the probe holder and align the wire as stated in the step (12).

30. Switch the TSI IFA 300 to run.

31. Initiate appropriate hot wire calibration routine in QuickBASIC.

32. Acquire the hot wire data over the range of velocities.

33. Switch the TSI IFA 300 to standby.

34. Remove the hot wire and put it away.

35. Shut down the calibration jet and re-circulation unit.

36. Create a single graph of using two velocity ranges.

a. Plot the high range velocity calibration (raw data and fourth order regression of the calibration velocity less the average velocity and the Reynolds number recorded by the QuickBASIC program) and check the uncertainty range.

b. Plot the low range velocity calibration (raw data and fourth order regression of the calibration velocity less the average velocity and the Reynolds number recorded by the QuickBASIC program) and check the uncertainty range.

37. If they both are within the range then use the overlap region (from approximately 1.5 m/s to 4.5 m/s) to create a new set of raw data for the entire range of velocities.

38. Use the QuickBasic program (ianalyze.bas) to perform another fourth order regression analysis on the voltages ($V_{calibration} - V_{average}$) and Reynolds numbers. Calibration files should be compiled from the raw data of the calibration over the low range of velocities and from the raw data compiled from both the high and low range velocity calibrations.

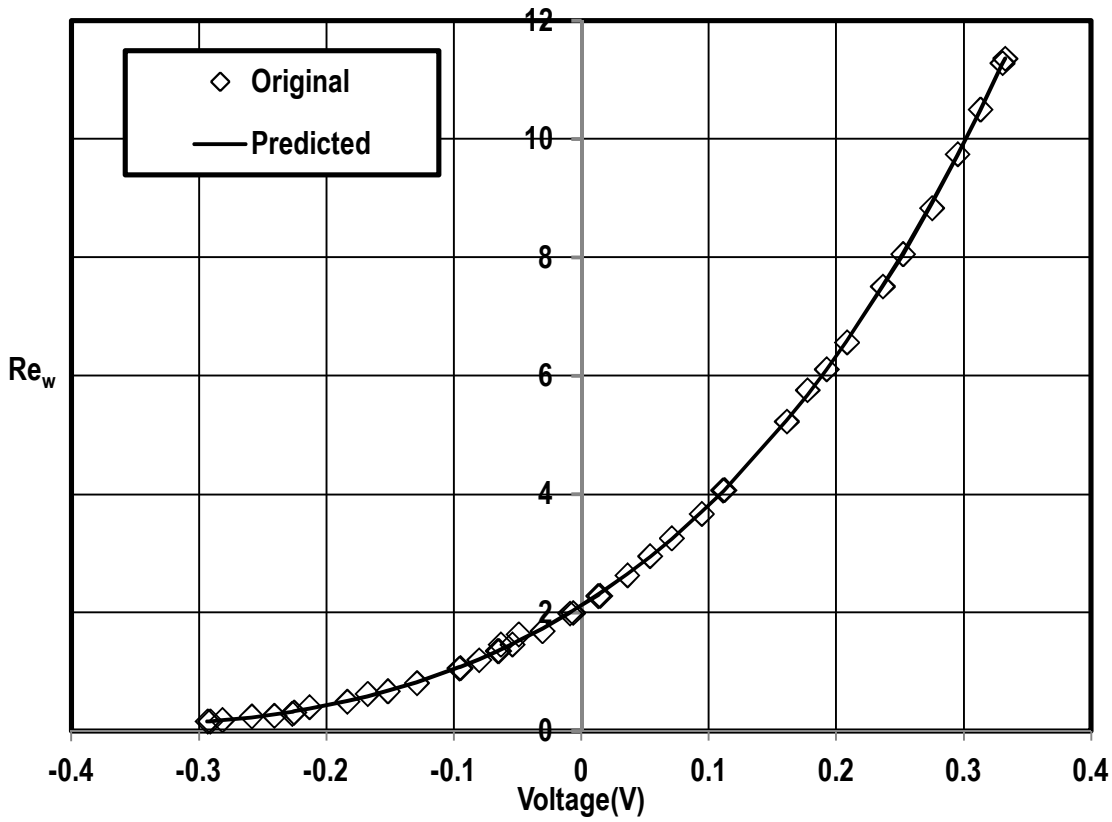

Figure 71: Calibration curve with 4th order polynomial fit.

APPENDIX D

UNCERTAINTY ANALYSIS

The experimental uncertainty related to turbulence measurement was performed using statistical approach and general technique for the single wire measurements. All uncertainties are based on a 95 percent confidence interval.

Single-Wire Data

In general, turbulence parameters uncertainty is the combination of three different sources including statistical uncertainty, uncertainty in the calibration, and uncertainty in measurement technique using a hot wire.

An uncertainty for the measurement of a mean streamwise velocity, U_{ave}, using the hot wire was estimated to be ±2.8 percent. The sources of this uncertainty due to drift in the calibration caused by the changes in operating temperatures and an uncertainty due to high turbulence effects and a finite sample size, and errors due to simultaneous wire cooling caused by normal and spanwise fluctuating components. The uncertainty in calibration was estimated within ±4 percent. The possible errors due to randomness were minimized by gathering large samples sizes such as 8192 points.

The effect of very high turbulence fluctuations on the hot wire response can be estimated by expanding the series for the n-th power of velocity to its higher order terms..

An equation for the average effective velocity, U_{eff}, is found using the average velocity, U_{ave} and the turbulence-velocity components. Errors in mean velocity from wire cooling due to cross stream components of turbulence can be estimated for the single wire using equation (2-46a) from Hinze (J. Hinze 1959). At the same time, it is recommended by Hinze to consider additional fluctuation component in other direction, since they cause a nonlinearity effect in the response of the hot wire.

$$\overline{U}_{eff} = U_{ave}\left(1 + \frac{v'^2}{2U_{ave}^2} - \frac{u'v'^2}{2U_{ave}^3} - \cdots\ldots\right)$$

The overall uncertainty in the of mean velocity for the single wire was typically around +/- 2 percent considering the isotropic turbulence but reached as high as +/- 5 percent for certain unsteady situations near the stagnation region due to large turbulence fluctuation. Hinze showed from his calculation that a turbulence intensity of 20 percent can contribute approximately 5 per cent for one-dimensional and 0.2 per cent for an isotropic turbulence. The present data sets were not corrected for this effect.

The statistical uncertainty in the turbulence intensity was estimated using the Chi-squared distribution. Chi-squared statistic is defined as a function of the degrees of freedom, ν, which is one less than sample population size, n. The uncertainty band of the variance, σ^2, can be calculated given the unbiased estimator for σ and n, S_{N-1}, with a confidence level of 1 - α. For a confidence level of 95 percent, α is 0.05.

For the present data, 8192 points were taken at sampling rate of 15000 Hz, for the convective velocity magnitude of 10 m/s and the integral length scale was about 5 cm. Considering 2.5 times of integral time scale, estimated from the autocorrelation, the number of independent samples was found to be 3495. To calculate the statistical component of the uncertainty in Tu, a sample size of 3495 was used. For the Chi-squared distribution with large sample sizes, a value of χ^2 is estimated based on α/2 of 0.025, ν of 3495, and a value of $Z_{(1-\alpha)/2}$ which is equal to 1.96.

$$\frac{\upsilon S_{N-1}^2}{\chi^2(\frac{\alpha}{2},\upsilon)} < \sigma^2 < \frac{\upsilon S_{N-1}^2}{\chi^2((1-\frac{\alpha}{2}),\upsilon)}$$

$$\frac{\upsilon S_{N-1}^2}{\chi^2(\frac{\alpha}{2},\upsilon)} < \sigma^2 < \frac{\upsilon S_{N-1}^2}{\chi^2((1-\frac{\alpha}{2}),\upsilon)}$$

$$\chi^2\left(\frac{\alpha}{2},\upsilon\right) = \frac{[Z_{\frac{(1-\alpha)}{2}} + (2\upsilon-1)^{\frac{1}{2}}]^2}{2} = 3660.53$$

$$\chi^2\left(1-\frac{\alpha}{2},\upsilon\right) = \frac{[-Z_{\frac{(1-\alpha)}{2}} + (2\upsilon-1)^{\frac{1}{2}}]^2}{2} = 3332.8$$

$$0.976 < \text{Tu} < 1.044 \qquad \left(Tu = \sqrt{\frac{\sigma^2}{S_{n-1}{}^2}}\right)$$

The uncertainty in Tu due to randomness is about +/- 2.33 percent and the overall uncertainty in u' is typically +/- 3.07 percent based on root-rum-square method explained by Moffat.

Experimental uncertainty for the dissipation rate, energy scale, Lu, and the integral length scale, Lx, were also estimated. Most often it is difficult to estimate the exact error in calculating these parameters, since most of them derived from the dissipation rate which is estimated by fitting the -5/3 slope in spectra plot. To accurately fit a slop is difficult and it is mostly qualitative rather than being quantitative, as they are most often fitted based on visual judgment. The worst case of uncertainty in the dissipation was encountered at Re_D = 62,500. Roughly this can be estimated within the +/- 1% band. The uncertainty in the energy scale with respect to u′ and dissipation rate resulted in an uncertainty of ±1 percent. The estimated uncertainty in the integral length scale was estimated from the data (no cylinder in position) to be about ± 8 percent for the lowest Reynolds number. However, the uncertainties in time scale will increase this uncertainty.

Due to high FST and possible vibration in the probe, there is a strong possibility of error generation. To understand the situation, a set of 8192 random data points were generated with an aim to distribute them in a circular region which a hot wire probe can sense. Then considering 16% turbulence level and a constant rms fluctuation, an uncertainty model is developed based on potential flow theory to determine the possible uncertainties. The model suggests that hot wire data does not hold good as the flow

approaches near the stagnation region and shows the same trend as found in the experiment in few worst cases.

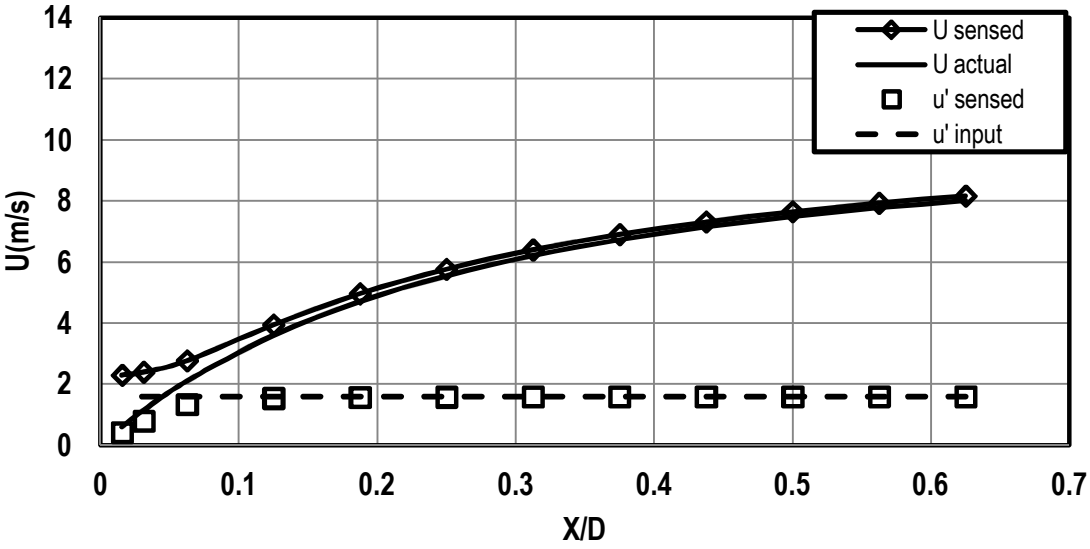

Figure 72: Velocity distribution along the stagnation streamline

APPENDIX E

Streamwise RMS fluctuating velocity distributions at four Reynolds numbers

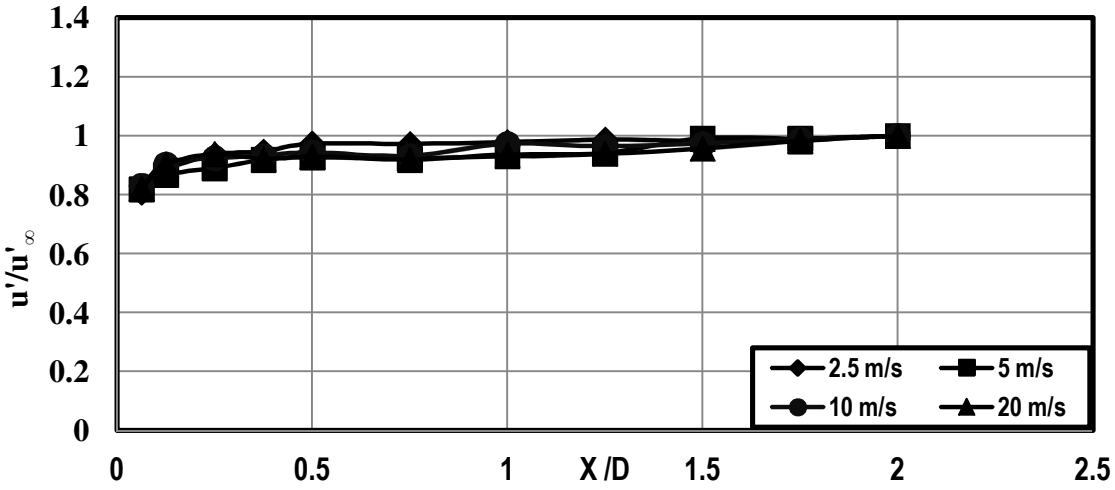

Figure 73: Dimensionless fluctuating velocity distribution for 4″ cylinder along normalized upstream distance from the cylinder stagnation point at four different Reynolds numbers with aero-combustor (AC1).

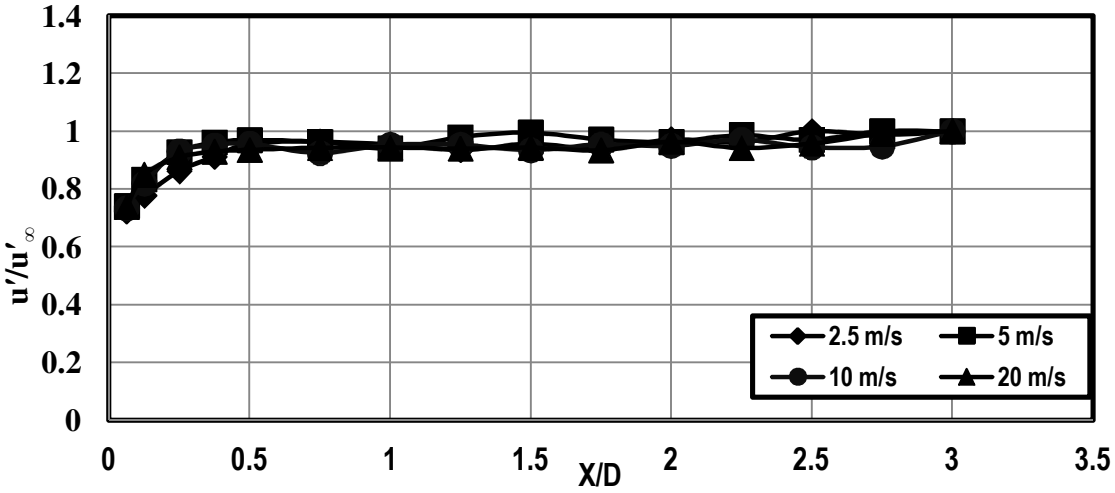

Figure 74: Dimensionless fluctuating velocity distribution for 4″ cylinder along normalized upstream distance from the cylinder stagnation point at four different Reynolds numbers for aero-combustor with spool (ACS).

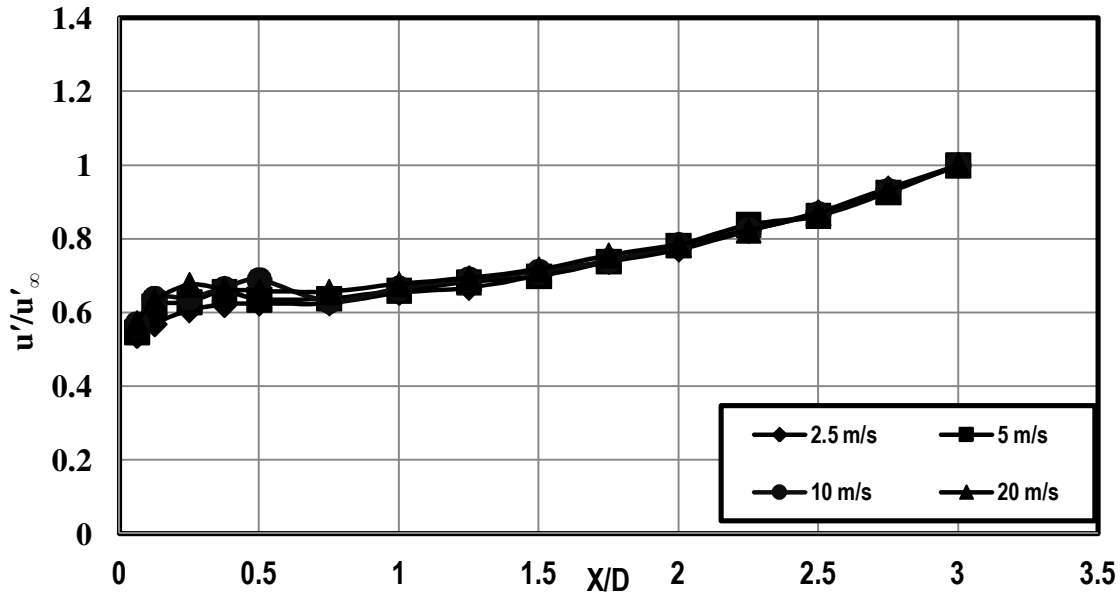

Figure 75: Dimensionless fluctuating velocity distribution for 4″ cylinder along normalized upstream distance from the cylinder stagnation point at four different Reynolds numbers with big grid (GR1).

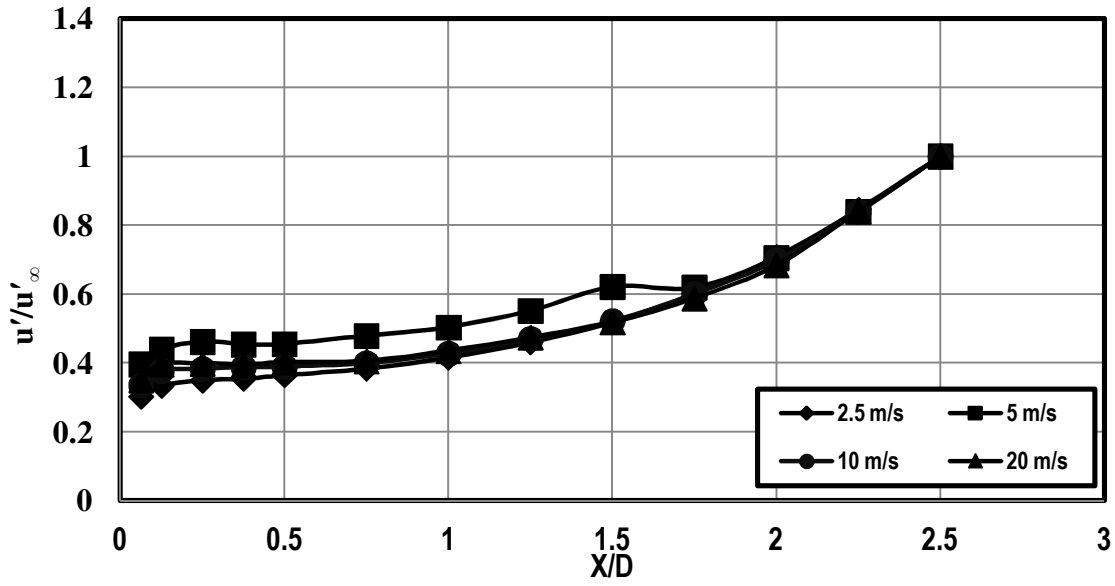

Figure 76: Dimensionless fluctuating velocity distribution for 4″ cylinder along normalized upstream distance from the cylinder stagnation point at four different Reynolds numbers with small grid at near location (GS1).

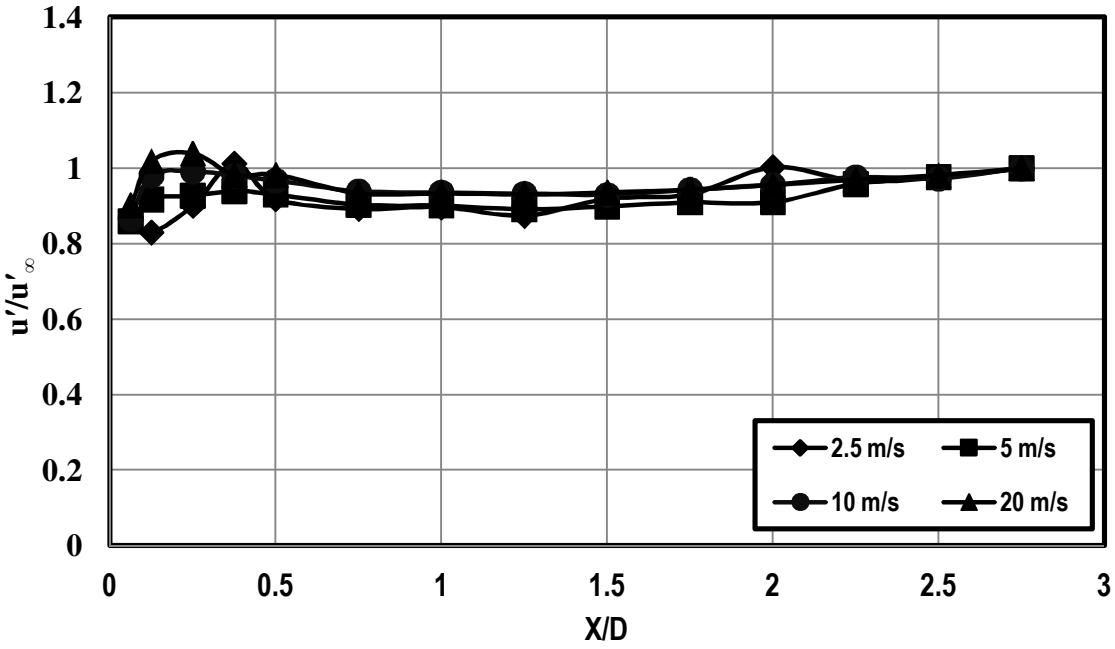

Figure 77: Dimensionless fluctuating velocity distribution for 4″ cylinder along normalized upstream distance from the cylinder stagnation point at four different Reynolds numbers with small grid at far location (GS2).

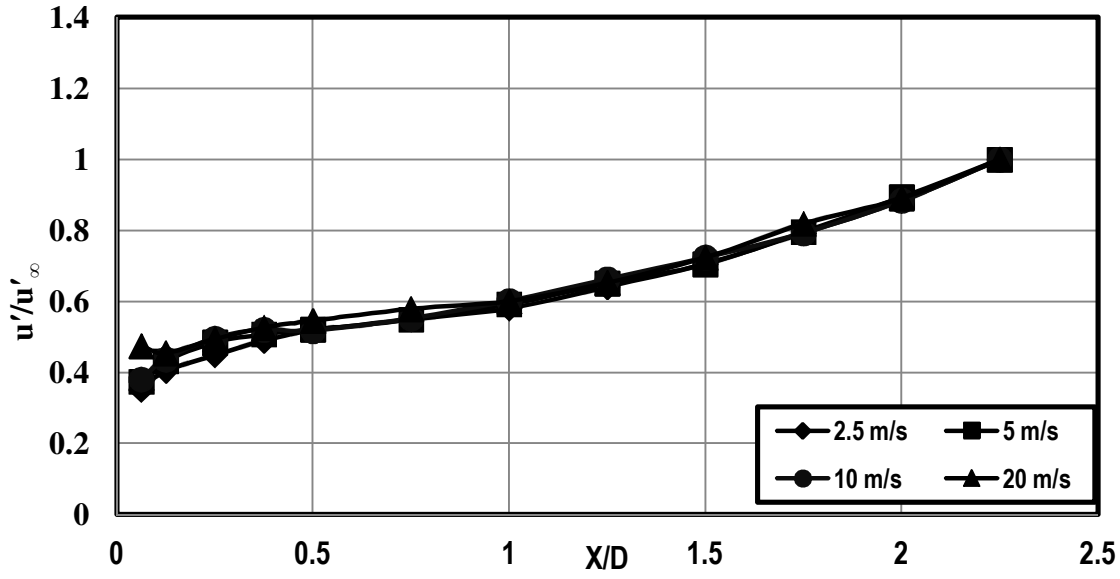

Figure 78: Dimensionless fluctuating velocity distribution for 4″ cylinder along normalized upstream distance from the cylinder stagnation point at four different Reynolds numbers for high turbulence generator (HT1).

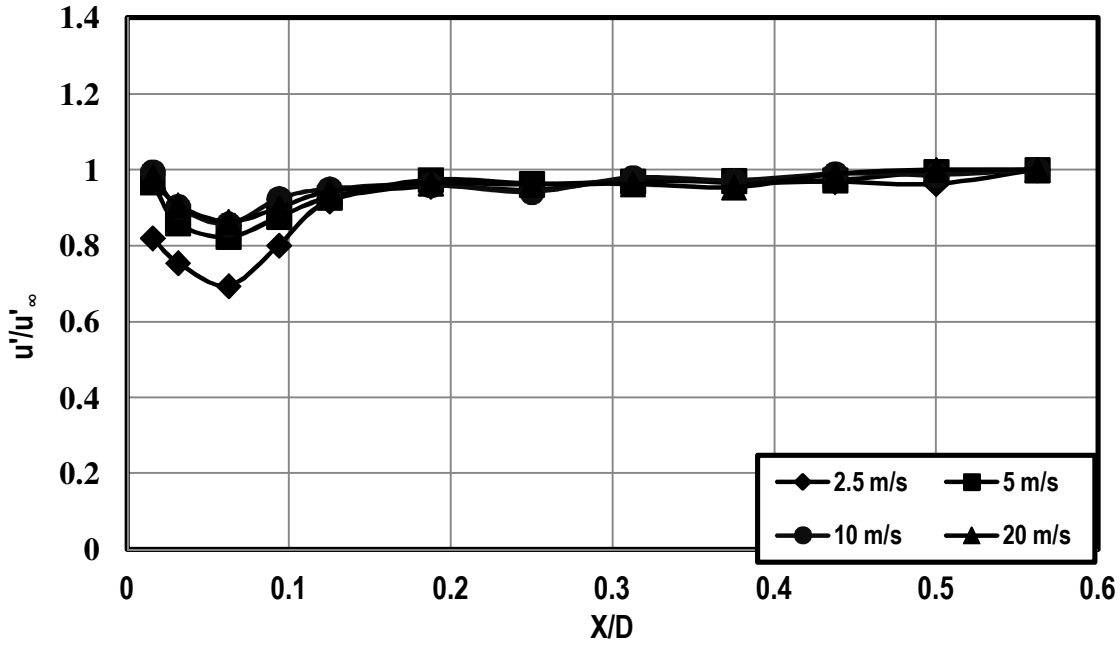

Figure 79: Dimensionless fluctuating velocity distribution for 16″ cylinder along normalized upstream distance from the cylinder stagnation point at four different Reynolds numbers with aero combustor (AC1).

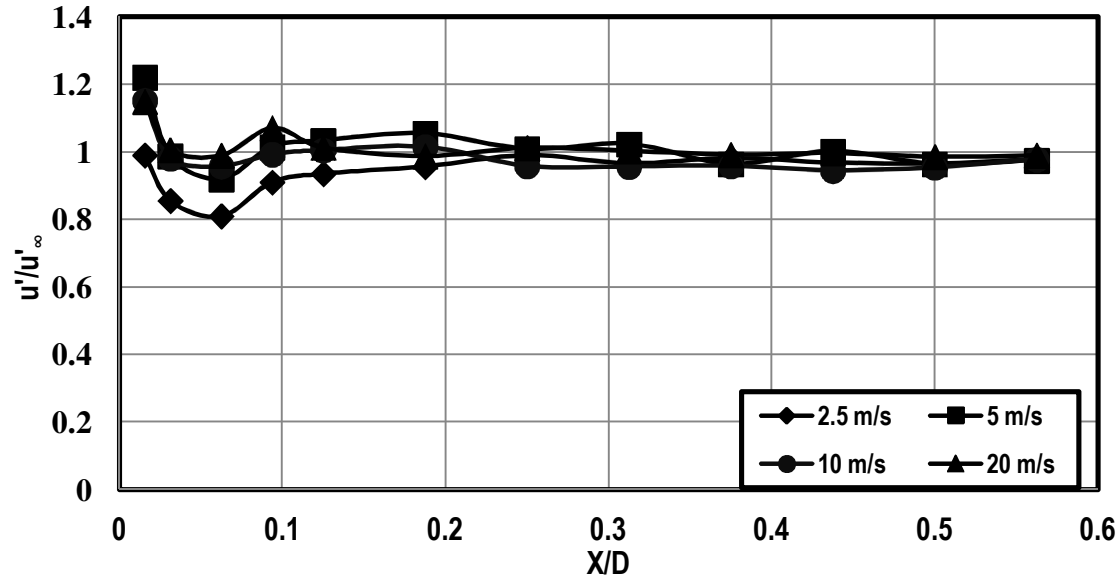

Figure 80: Dimensionless fluctuating velocity distribution for 16″ cylinder along normalized upstream distance from the cylinder stagnation point at four different Reynolds numbers for aero combustor with spool (ACS).

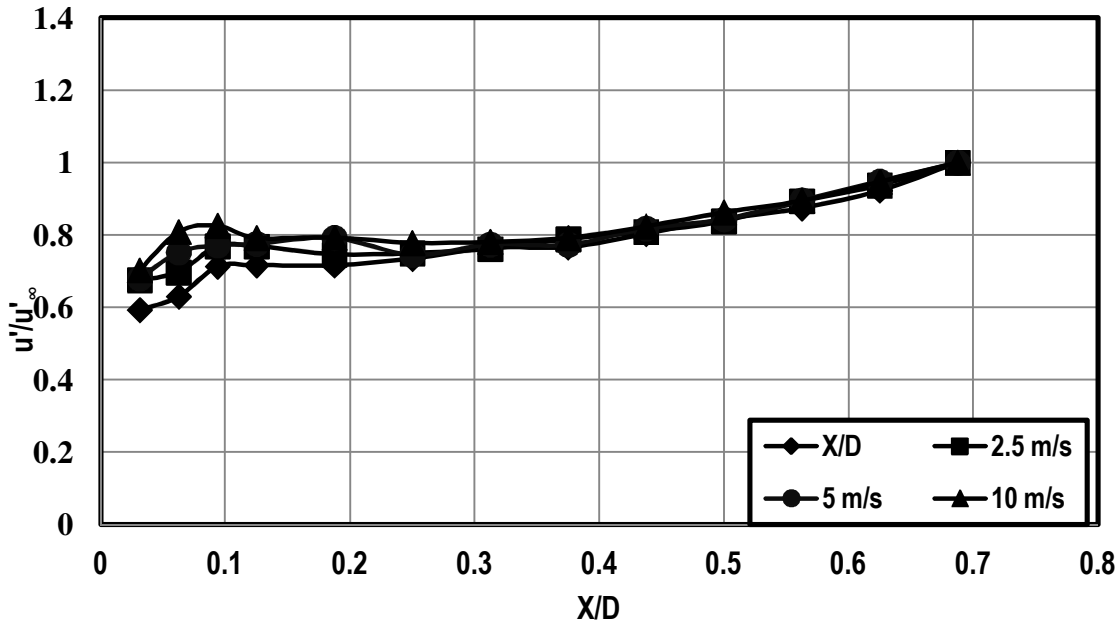

Figure 81: Dimensionless fluctuating velocity distribution for 16″ cylinder along normalized upstream distance from the cylinder stagnation point at four different Reynolds numbers for big grid (GR1).

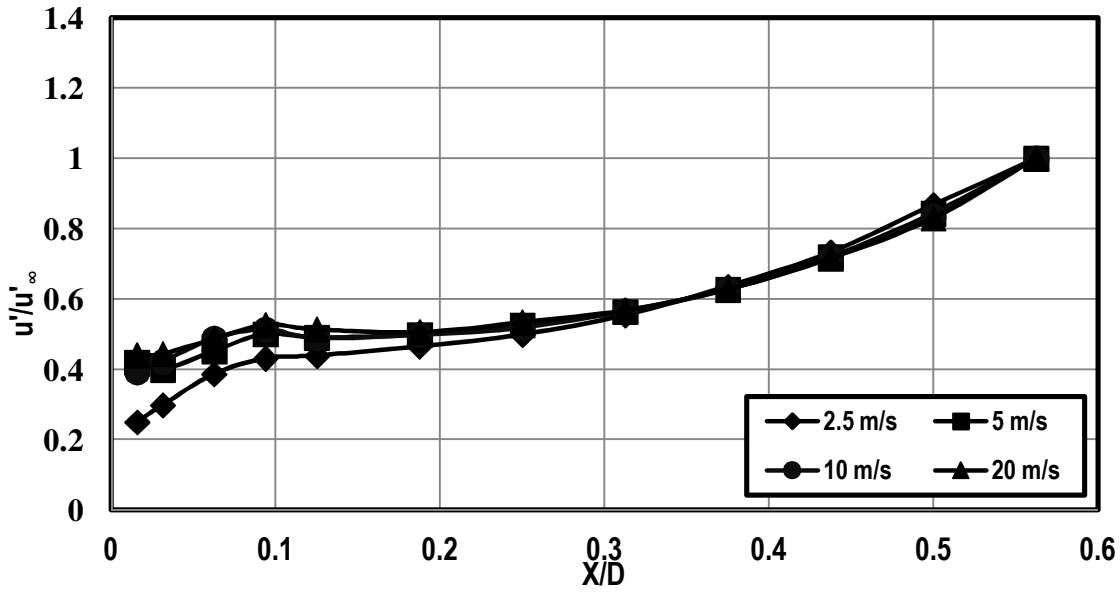

Figure 82 : Dimensionless fluctuating velocity distribution for 16″ cylinder along normalized upstream distance from the cylinder stagnation point at four different Reynolds numbers for small grid at near location (GS1).

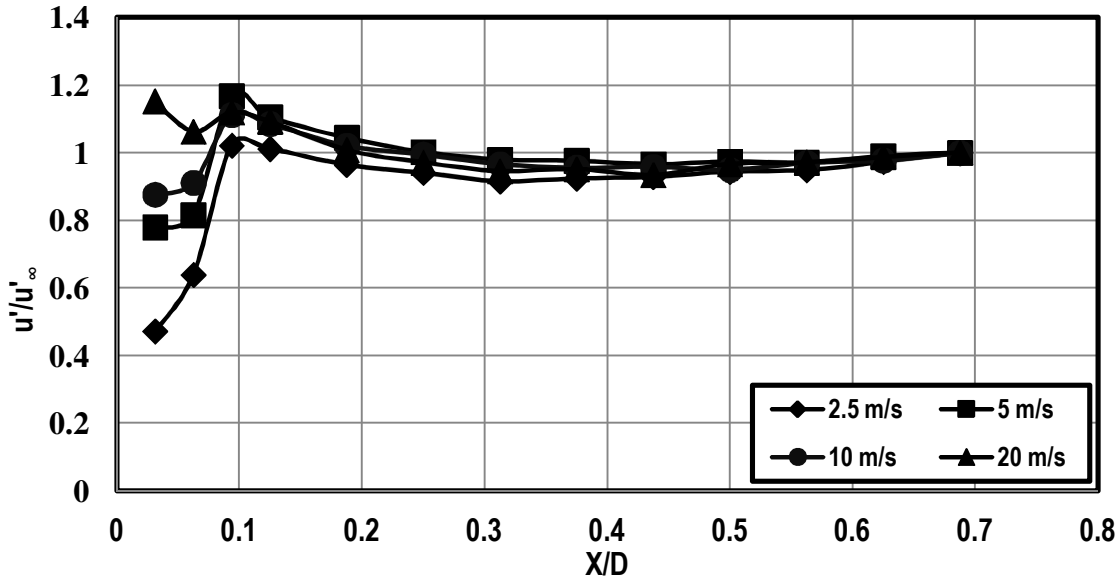

Figure 83: Dimensionless fluctuating velocity distribution for 16″ cylinder along normalized upstream distance from the cylinder stagnation point at four different Reynolds numbers for small grid at far location (GS2).

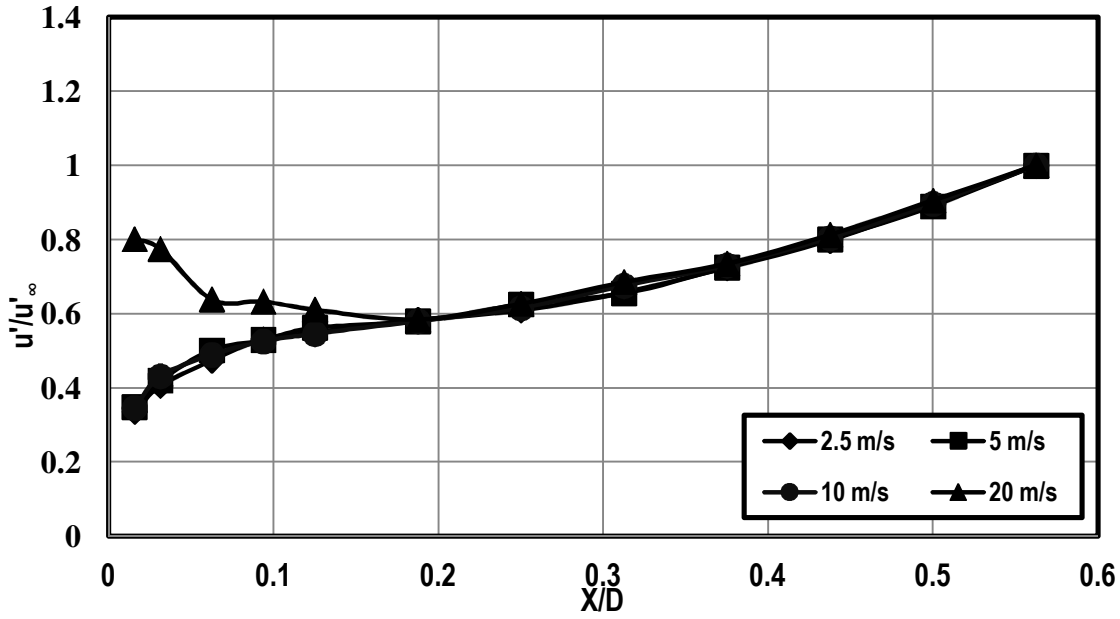

Figure 84: Dimensionless fluctuating velocity distribution for 16″ cylinder along normalized upstream distance from the cylinder stagnation point at four different Reynolds numbers for high turbulence generator (HT1).

APPENDIX E

Streamwise integral length scale distributions at four Reynolds numbers

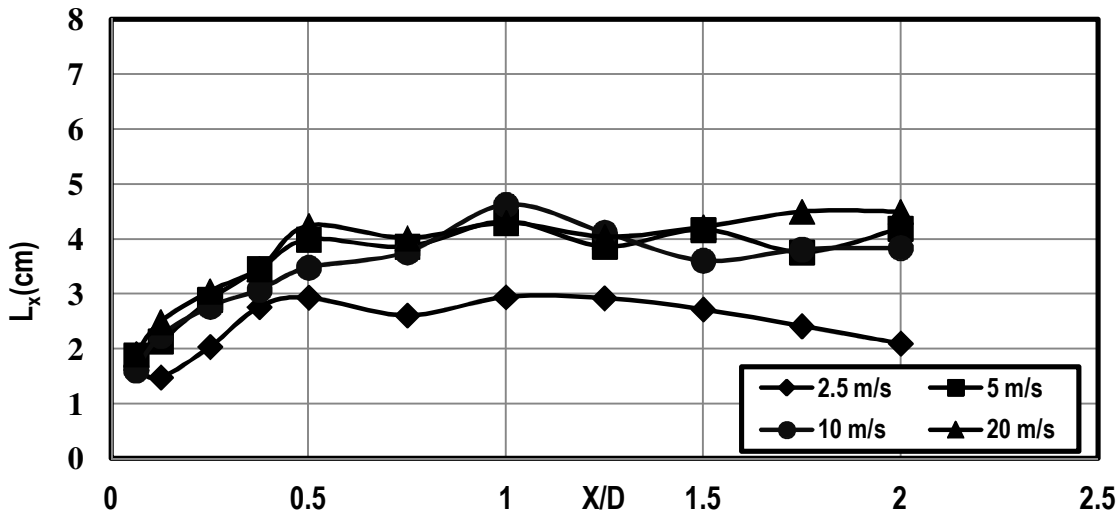

Figure 85: Integral length scale distribution for 4″ cylinder along normalized upstream distance from the cylinder stagnation point at four different velocities for aero combustor (AC1).

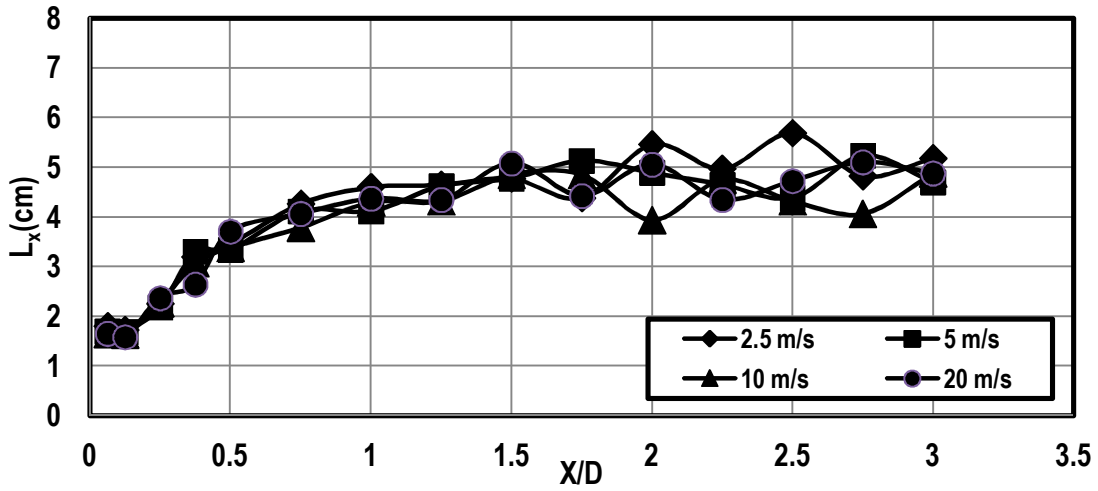

Figure 86: Integral length scale distribution for 4″ cylinder along normalized upstream distance from the cylinder stagnation point at four different velocities for aero combustor with spool (ACS).

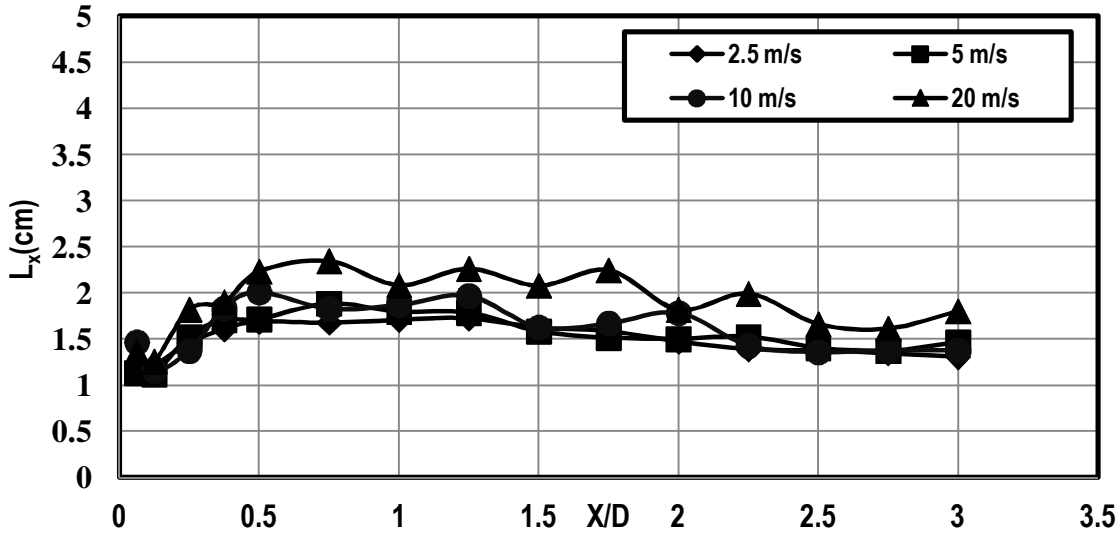

Figure 87: Integral length scale distribution for 4″ cylinder along normalized upstream distance from the cylinder stagnation point at four different Reynolds numbers for big grid (GR1).

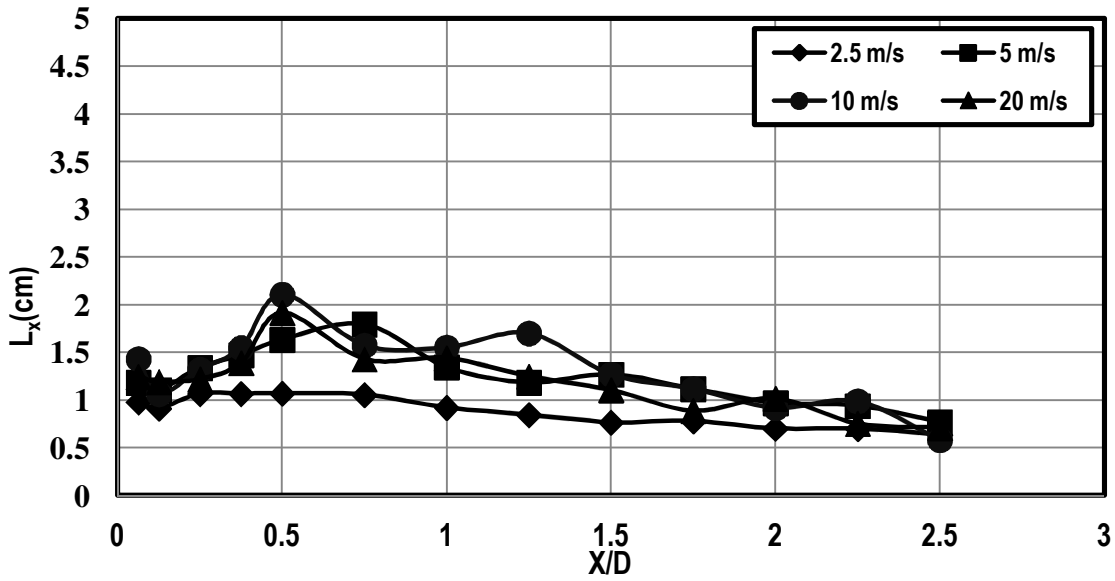

Figure 88: Integral length scale distribution for 4″ cylinder along normalized upstream distance from the cylinder stagnation point at four different Reynolds numbers for small grid near position (GS1).

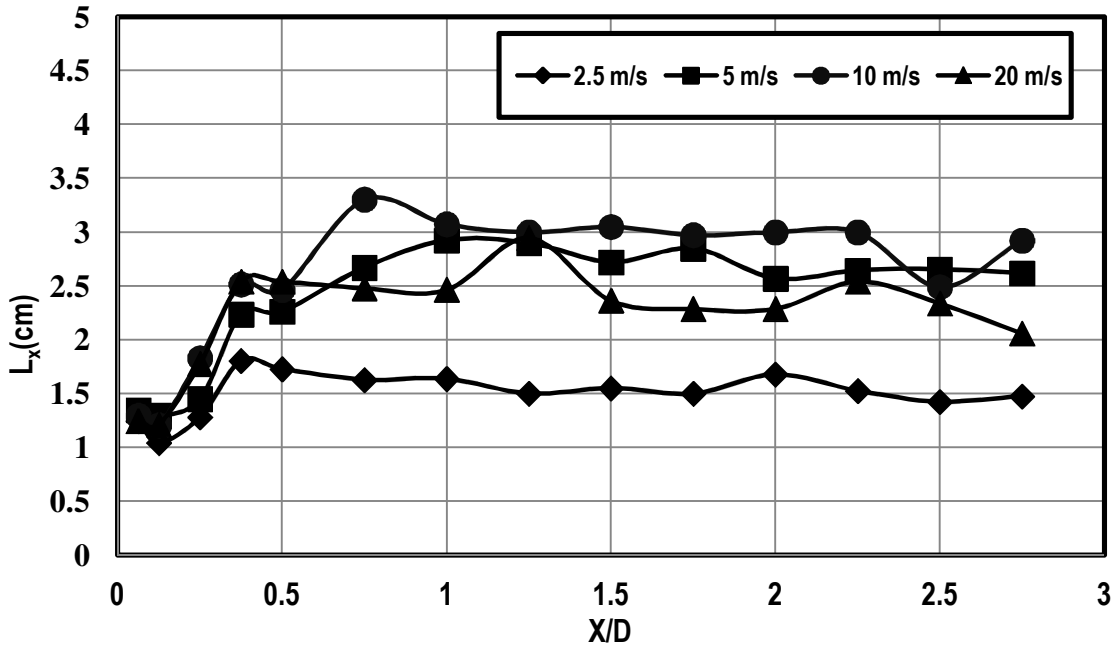

Figure 89: Integral length scale distribution for 4″ cylinder along normalized upstream distance from the cylinder stagnation point at four different Reynolds numbers for small grid at far position (GS2).

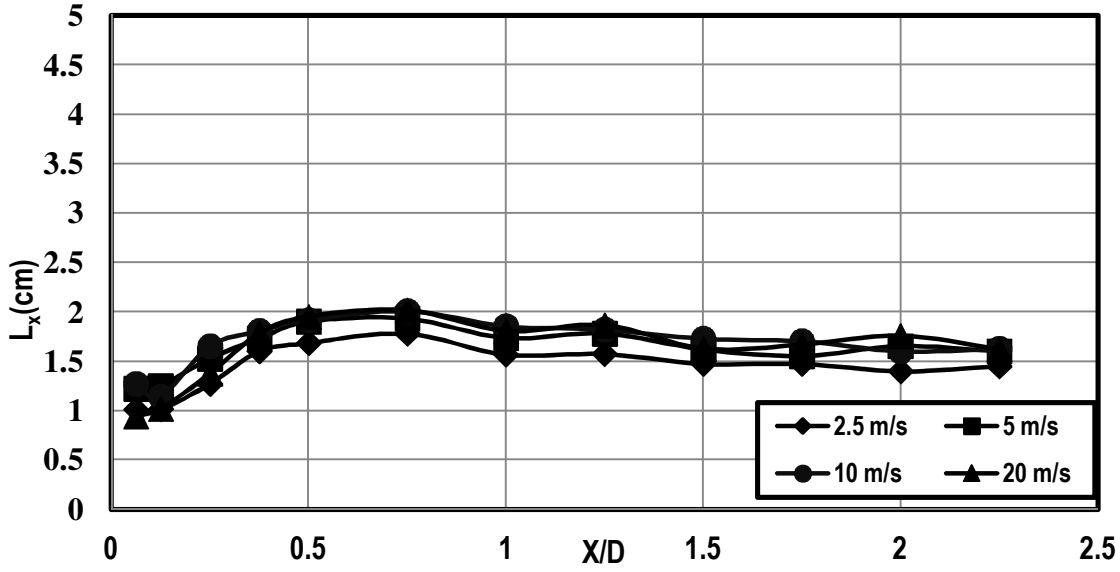

Figure 90: Integral length scale distribution for 4″ cylinder along normalized upstream distance from the cylinder stagnation point at four different velocities for high turbulence generator (HT1).

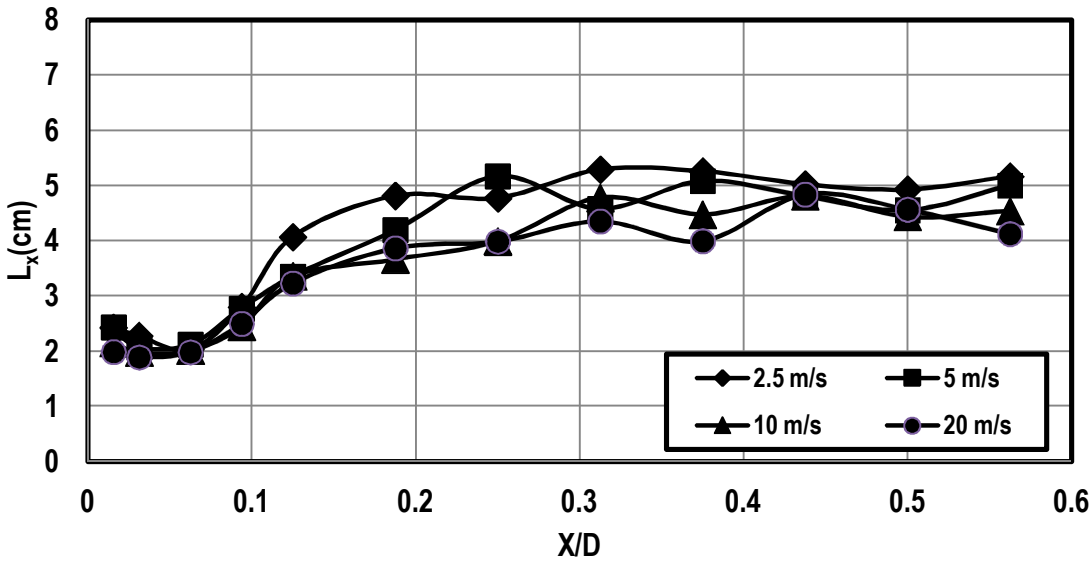

Figure 91: Integral length scale distribution for 16″ cylinder along normalized upstream distance from the cylinder stagnation point at four different velocities for aero combustor (AC1).

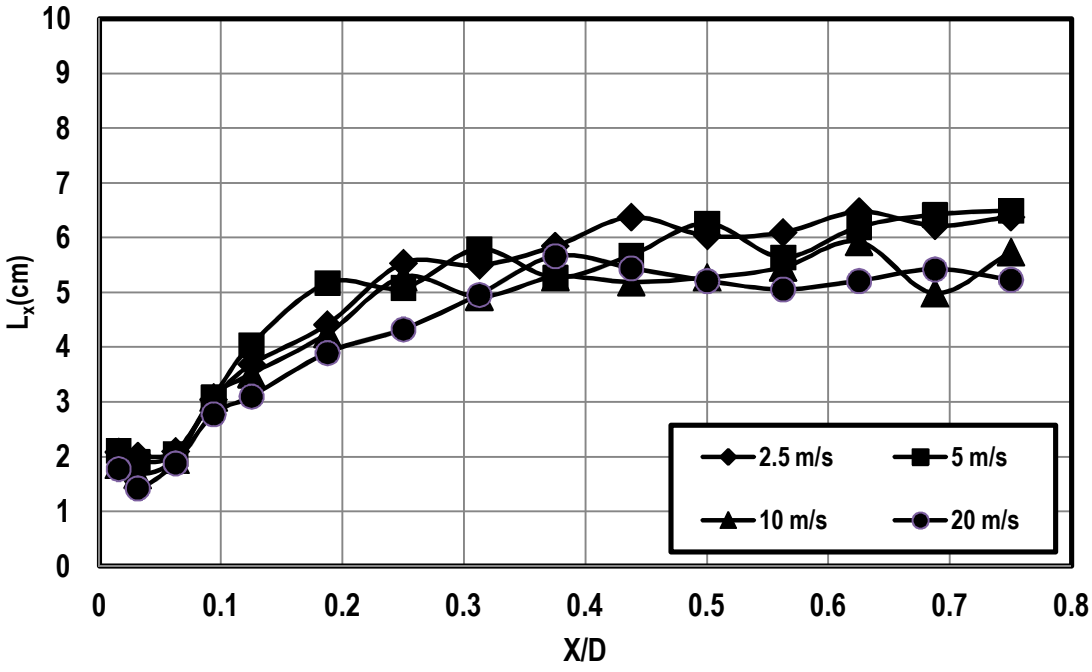

Figure 92: Integral length scale distribution for 16″ cylinder along normalized upstream distance from the cylinder stagnation point at four different velocities for aero combustor with spool (ACS).

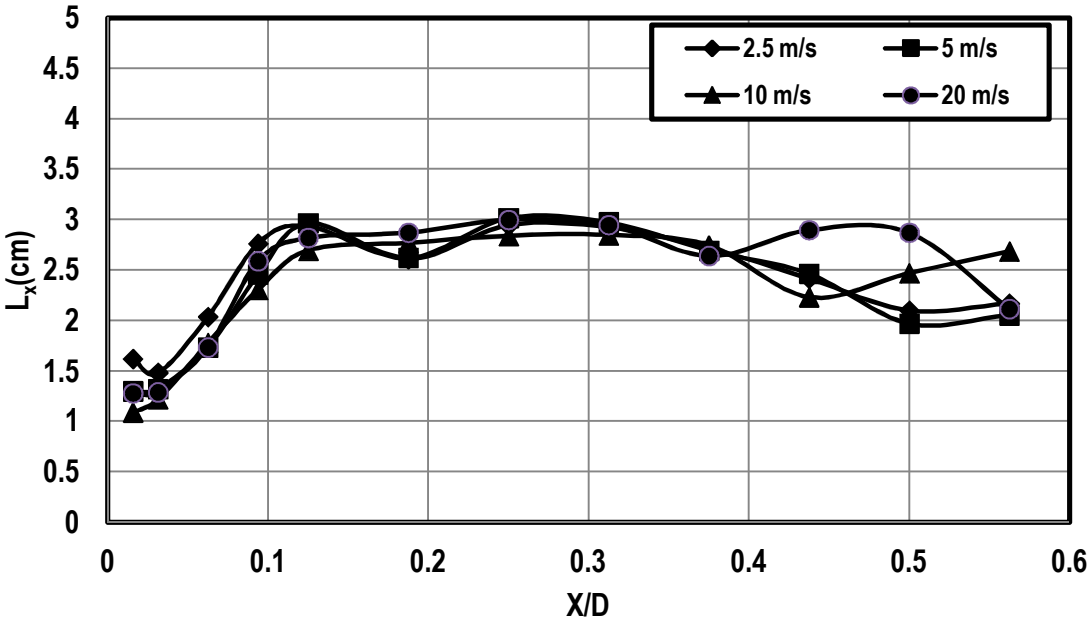

Figure 93: Integral length scale distribution for 16″ cylinder along normalized upstream distance from the cylinder stagnation point at four different Reynolds numbers for big grid (GR1).

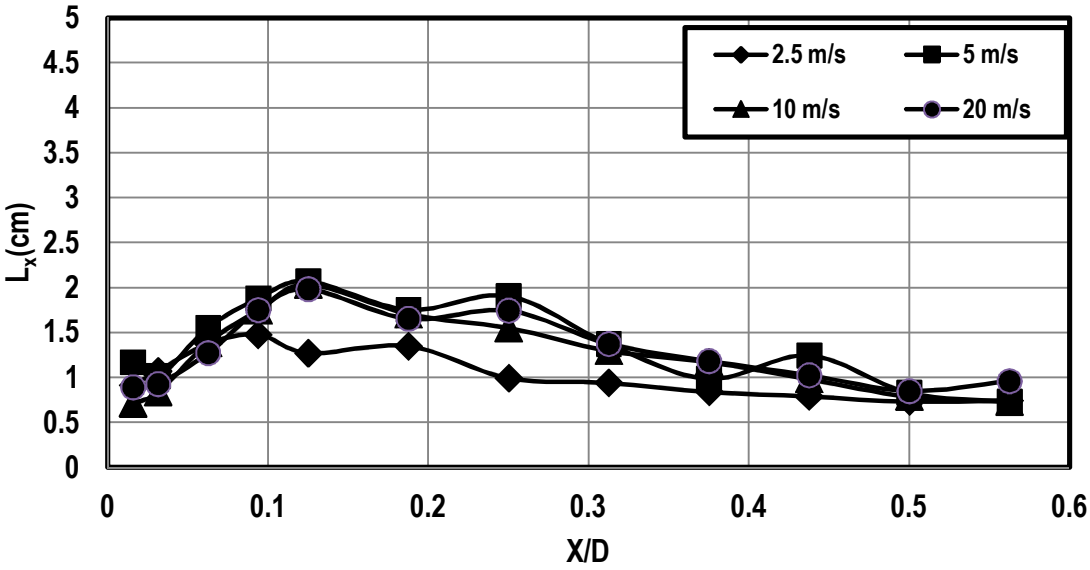

Figure 94: Integral length scale distribution for 16″ cylinder along normalized upstream distance from the cylinder stagnation point at four different Reynolds numbers for small grid at near position (GS1).

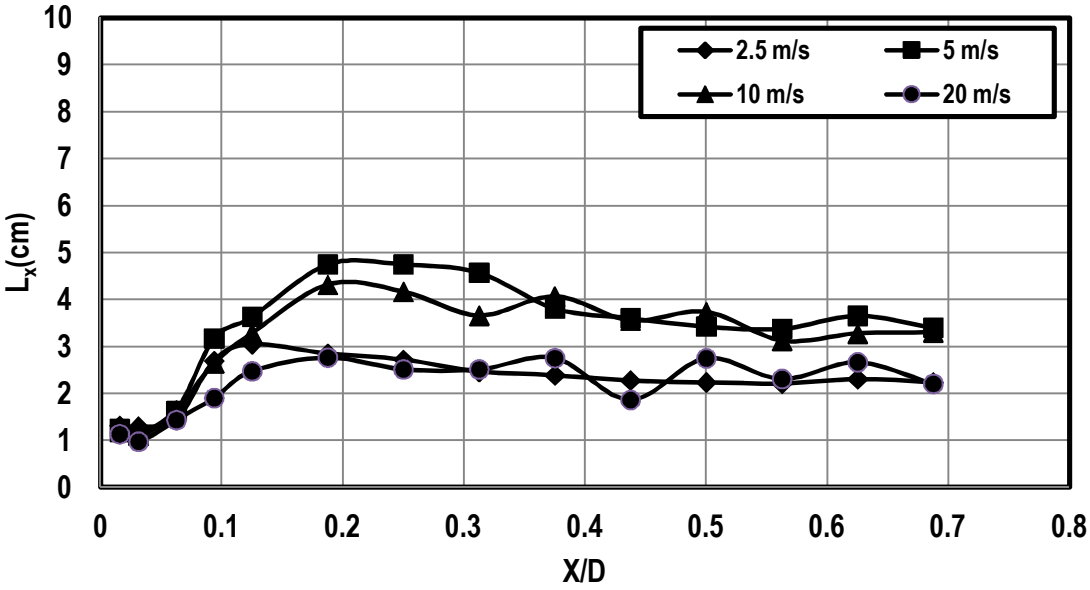

Figure 95: Integral length scale distribution for 16″ cylinder along normalized upstream distance from the cylinder stagnation point at four different Reynolds numbers for small grid at far position (GS2).

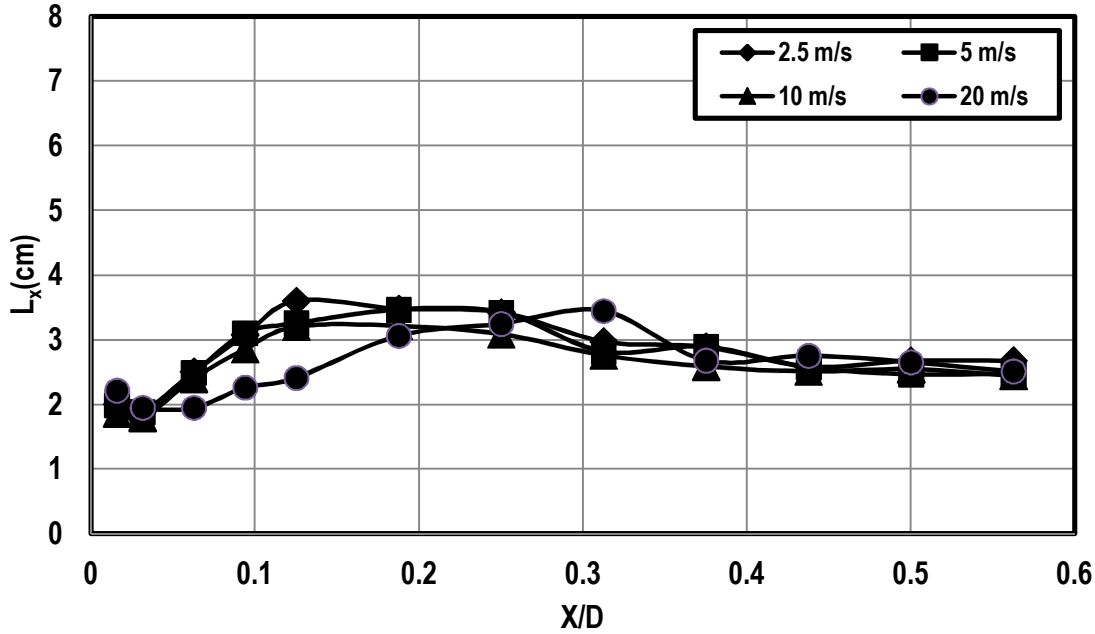

Figure 96: Integral length scale distribution for 16″ cylinder along normalized upstream distance from the cylinder stagnation point at four different Reynolds numbers for high turbulence generator (HT1).

REFERENCES

Ames, F.E. 1997, "The influence of large scale, high intensity turbulence on vane heat transfer", *ASME Journal of Turbomachinery,* vol. 119, pp. 23-30.

Ames, F.E., and Moffat, R.J. 1990, *Heat Transfer with High Intensity, Large Scale Turbulence: The Flat Plate Turbulent Boundary Layer and the Cylindrical Stagnation Point*, Stanford University.

Ames, F.E., Argenziano, M., Wang 2004, "Measurement and Prediction of Heat Transfer Distributions on an Aft-Loaded Vane Subjected to the Influence of Catalytic and Dry Low NO_x Combustor Turbulence", *Journal of Turbomachinery,* vol. 126, no. 1, pp. 139.

Ames, F.E., Barbot, P.A., Wang, C 2003, "Effects of Aeroderivative Combustor Turbulence on Endwall Heat Transfer Distributions Acquired in a Linear Vane Cascade", *ASME Journal of Turbomachinery,* vol. 125, pp. 221-231.

Ames, F.E., Wang, C., and Barbot, P.A. 2003, "Measurement and prediction of the influence of catalytic and dry low NOx Combustor Turbulence on Vane Surface Heat Transfer", *ASME Journal of Turbomachinery,* vol. 125, pp. 210-23 1220.

Barbot, P.A. 2003, *The Effects Of Combustor Generated Turbulence And Reynolds Number On Endwall Heat Transfer Distributions In A Linear Vane Cascade*, University of North Dakota.

F. E. Ames, L. A. Dvorak, and M. J. Morrow 2005, "Turbulent Augmentation of Internal Convection Over Pins in Staggered-Pin Fin Arrays", *Journal of turbomachinery,* vol. 127, no. 1, pp. 183.

Finn E. Jørgensen 2002, *How to measure turbulence with hot-wire anemometers- a practical guide*, Dantec Dynamics A/S, Skovlunde, Denmark.

Forrest E. Ames 1990, *Heat Transfer with High Intensity, Large Scale Turbulence: The Flat Plate Turbulent Boundary Layer and The Cylindrical Stagnation Point*, Stanford University.

G. James Van Fossen and Chan Y. Ching 1997, "Measurements of the Influence of Integral Length Scale on Stagnation Region Heat Transfer", *International Journal of Rotating Machinery,* vol. 3, No. 2, pp. 117-132.

Gifford, A.R., Diller, T.E., and Vlachos, P.P. 2011, "The Physical Mechanism of Heat Transfer Augmentation in Stagnation Flow Subject to Freestream Turbulence", *ASME Journal of Heat Transfer,* vol. 133, no. 021901-1-11.

Hunt, J.C.R. 1973, "A theory of turbulent flow round two dimensional bluff bodies", *J. Fluid Mech.,* vol. 61, part 4, pp. 625.

Indrajit Jaswal 2008, *Aerodynamic Losses and Heat Transfer for A Covered Trailing Edge Turbine Vane with A High Solidity Low Pressure Drop Pedestal Pin Fin Array and Variable Coolant Ejection*, University of North Dakota.

J. Hinze 1959, *Turbulence, An introduction to its Mechanism and Theory,* McGraw-Hill, New York.

K.A. Thole, R.W. Radomsky, M.B. Kang, A. Kohli 2002, "Elevated freestream turbulence effects on heat transfer for a gas turbine vane", *International Journal of Heat and Fluid Flow,* vol. 23, pp. 137-147.

Kestin, J. 1966, "The Effect of Free-Stream Turbulence on Heat Transfer Rates", *Advances in Heat Transfer,* vol. 3, pp. 1-32.

Kestin, J., and Wood, R.T. 1971, "The influence of turbulence on mass transfer from cylinders", *Journal of Heat Transfer,* vol. 93, no. 4, pp. 321.

Lindsay A. Dvorak 2004, *Turbulent Augmentation of Heat Transfer off Pin and Endwall surfaces In A Staggered Pin Fin Array*, University of North Dakota.

Lowery,G.W.,Vachon,R.I. 1975, "The effect of turbulence on heat transfer from heated cylinders", *International Journal of Heat and Mass Transfer,* vol. 18, no. 11, pp. 1229-1242.

Mehendale, A.B., Han, J.C., and Ou, S. 1991, "Influence of high mainstream turbulence on leading edge heat transfer", *Journal of Heat Transfer,* vol. 113, no. 4, pp. 843-850.

Nix, A.C., Diller, T.E. 2009, "Experiments on the Physical Mechanism of Heat Transfer Augmentation by Freestream Turbulence at a Cylinder Stagnation Point", *ASME Journal of Turbomachinery,* vol. 131, no. 2, pp. 021015.

Nix, A.C., Diller, T.E., and Ng, W. F. "Experimental Measurements and Modeling of the Effects of Large-Scale Freestream Turbulence on Heat Transfer", *ASME J. Turbomach.,* vol. 129, pp. 550-550.

Oo, A.N., and Ching, C.Y. 2002, "Stagnation line heat transfer augmentation due to freestream vortical structures and vorticity", *ASME J. Heat Transfer,* vol. 124, pp. 583-587.

P.W.Bearman 1972, "Some measurements of the distortion of turbulence approaching a two-dimensional bluff body", *Journal of Fluid Mechanics,* vol. 53 part 3, pp. 451-467.

Preethi Gandavarapu 2011, *The Influence of High Turbulence Intensity and Large Leading Edge Reynolds Numbers on Stagnation Region Heat Transfer*, University of North Dakota.

R. E. Britter, J. C. R. Hunt and J. C. Mumford 1979, "The distortion of turbulence by a circular cylinder,", *Journal of Fluid Mechanics,* vol. 92, part 2, pp. 269-301.

Rigby, D.L., and Van Fossen, G.J. 1991, "Increased heat transfer to a cylindrical leading edge due to spanwise variations in the freestream velocity", *AIAA 22nd Fluid Dynamics,Plasma Dynamics and Lasers Conference*.

S. Bae, S.K.Lele and H.J.Sung 2000, "Influence of Inflow Disturbances on Stagnation-Region Heat Transfer", *Journal of Heat Transfer,* vol. 122, pp. 258-265.

S. Sanitjai, R.J.G. 2001, "Effect of free stream turbulence on local mass transfer from a circular cylinder", *International Journal of Heat and Mass Transfer,* vol. 44, no. 15, pp. 2863-2875.

Smith, M.C., and Kuethe, A.M. 1966, "Effects of turbulence on laminar skin friction and heat transfer", vol. 9, no. 12, pp. 2337.

Sutera S.P 1965, "Vorticity amplification in stagnation-point flow and its effects on heat transfer", *Journal of Fluid Mechanics,* , pp. 513-534.

Sutera S.P., Maeder P.F. and Kestin J. 1963, "On the sensitivity of heat transfer in the stagnation point boundary layer to free-stream velocity", *Journal of Fluid Mechanics,* vol. 16, pp. 497.

Van Fossen, G. James and Bunker, Ronald S 2001, "Augmentation of stagnation region heat transfer due to turbulence from a DLN can combustor", *ASME J. of Turbomachinery,* vol. 123, pp. 140-146.

Van Fossen, G.J., Simoneau, R.J., and Ching, C.Y. 1995, "Influence of turbulence parameters, Reynolds number, and bodyshape on stagnation region heat transfer", *ASME J. Heat Transfer,* vol. 117, pp. 597-603.

VanFossen, G. J.& Simoneau, R. J. 1987, "A Study of the Relationship Between Free-Stream Turbulence and Stagnation Region Heat Transfer", *J. of Heat transfer,* vol. 109, pp. 10-24.

Zapp, G.M. 1950, *The effect of turbulence on local heat transfer coefficients around a cylinder normal to an air stream*, Master's Thesis edn, Oregon State College.

Zhongmin Xiong and Sanjiva K. Lele 2007, "Numerical study of leading edge heat transfer under free-stream turbulence", *Journal of Fluid Mechanics,* vol. 590, pp. 1-33.